論文 / 著書情報
Article / Book Information

題目(和文)	高速炉用炭化ホウ素中性子吸収材の中性子照射効果
Title(English)	Effect of Fast Neutron Irradiation on B4C Absorber for Fast Reactors
著者(和文)	You Yan
Author(English)	Yan You
出典(和文)	学位:博士(学術), 学位授与機関:東京工業大学, 報告番号:甲第10898号, 授与年月日:2018年3月26日, 学位の種別:課程博士, 審査員:矢野 豊彦,小原 徹,小林 能直,高橋 実,吉田 克己
Citation(English)	Degree:Doctor (Academic), Conferring organization: Tokyo Institute of Technology, Report number:甲第10898号, Conferred date:2018/3/26, Degree Type:Course doctor, Examiner:,,,,
学位種別(和文)	博士論文
Category(English)	Doctoral Thesis
種別(和文)	要約
Type(English)	Outline

Doctoral Dissertation

EFFECT OF FAST NEUTRON IRRADIATION ON B_4C ABSORBER FOR FAST REACTORS

by

You, Yan

Department of Nuclear Engineering,
Tokyo Institute of Technology

February, 2018

Contents

CHAPTER 1
Introduction

1.1 Background

The most of the operating commercial nuclear power plants are light water reactors (LWR), which use ^{235}U as nuclear fuels. However, the ^{235}U comprises only 0.72% of natural uranium, almost all the rest are ^{238}U which could hardly be directly utilized in LWR. By capturing a neutron and two β decay, the ^{238}U could transmute to another fissile nuclide, ^{239}Pu. The ratio of the consumed ^{235}U and the newly produced ^{239}Pu are called conversion ratio. The common LWR have a conversion ratio of around 0.6, approximately only 1.8% of the total uranium resource could be utilized by the LWR-only fuel cycle. This means that after approximately 200 years, all the economically accessible uranium resources on earth would drain if the same level of the present existing installed capacity of nuclear power was kept[1]. However, the current primary energy supply share of nuclear energy is only 4.9%[2], far from enough to make a significant contribution on reducing the emission of greenhouse gas and filling the newly added global energy needs. The IEA 450 scenario, which aimed to limit the increase in the global temperature to less than 2°C, indicated that the nuclear power output needs to be increased to almost 2.5 times compared to present day by 2040[3]. Clearly, the LWR alone cannot sustain the long-term use of the nuclear power of such amount. Luckily, there is a kind of reactors utilizing the fast spectrum neutrons that have a conversion ratio of above 1, theoretically make all the uranium fully utilized in generating energy, named as the fast “breeder” reactors (FBR)[4]. With the FBR put into the nuclear fuel cycle, the ^{238}U could be constantly be converted into ^{239}Pu and be made into fuel return to the fuel cycle. Further, the fast spectrum neutron could also

significantly reduce the long half-life nuclear waste by the transmutations of the nuclides. Hence, the FBR is definitely the key technology to the sustainability of nuclear power and have great significance to the future sustainable development of human society.

1.2 Neutron absorber materials for FBR

Due to the constant production of the so-called “neutron poison” during reactor operation, a nuclear reactor must capable to reach supercritical that with an effective neutron multiplication factor $k_{eff} > 1$ in design. While the control rods full filled with neutron absorber materials are used to eliminate the excess k_{eff} to adjust the reactor power and keep the criticality of the fission chain reactions. Naturally, just as the name implies, the most important indicator of whether a material can be used as a neutron absorber is its neutron absorbing capability.

Because of almost all kinds of nuclides have much smaller neutron absorb cross sections for the fast spectrum of neutrons than for the thermal spectrum of neutrons, the standard of selecting neutron absorbers for FBR is much harsher than for LWR. There are only boron, tantalum, a few rare earth elements, and their various compounds are considered suitable for use as neutron absorbers for fast reactors.

The ^{10}B, which have a natural isotopic abundance of 19.8 at%, have a great neutron absorption cross-section of 3840 barns for 25.3 meV thermal neutrons, and on several barns order for 1 keV fast neutrons, makes boron-containing compounds outstanding neutron control materials for nuclear reactors[5]. The elemental boron is less used directly as a neutron absorber in reactors due to its active chemical properties; boron can react with water to form boric acid and hydrogen, and react with almost all metals to form nonstoichiometric compounds at high temperature. As a result of having high boron content, excellent chemical stability, high melting point, light weight, and easy to produce, the boron carbide (B_4C) is the most widely used compound of boron as neutron absorbers in FBR, as shown in **Table 1.1**. However, due to the $^{10}B(n, \alpha)^{7}Li$

reaction, the accumulation of helium causing pellet swelling have been the main problem to be solved, which is the main purpose of this research, and the details will be described in the following chapters.

Comparing with boron, the neutron absorbing capability of tantalum and europium are inferior. However, they still had been considered as potential alternatives to B_4C by the advantage of that there is no helium generation form their neutron capture reactions have made them alternative FBR absorber materials. Moreover, unlike ^{10}B, the products of the neutron capture reaction of ^{181}Ta, ^{182}Ta, and ^{182}W also have large neutron capture cross sections. As a result, the performance degradation in capturing neutrons of tantalum absorber is slower than the boron carbide absorber. However, the (n, γ) reaction of ^{181}Ta and the decay of ^{182}Ta release a large amount of heat, and the decay heat would continue for a long time after shutdown the reactor[6, 7]. Hence, extra cooling margin needs to be considered when using the tantalum absorber. in FBR In addition, due to the high density of tantalum, it is considered a good absorber material for the safety rods of the fast reactors using the heavy liquid lead or lead-bismuth eutectic alloy as a coolant, which is required to insect by gravity[8]. In the case of europium, due to the high chemical reactivity of its metallic state, the more stable Eu_2O_3 is a more favorable form for use as neutron absorbers. A previous study on Eu_2O_3 has indicated that it has larger reactivity worth than tantalum, while release less decay heat[7]. Beside the Eu_2O_3, to achieve a higher reactivity worth, the europium hexaboride (EuB_6) also have been studied in 1960-1970s. Due to both high neutron absorption of boron and europium atoms of EuB_6, the reactivity worth of EuB_6 is even higher than B_4C with the same enrichment in ^{10}B. Neutron irradiation experiments showed the EuB_6 can release almost all the helium that was generated[7, 9, 10]. However, depending on Hoyt et al.[10], the advantage of EuB_6 in excluding helium gas to B_4C absorber is not reflected in the inhibition of volume expansion. Moreover, the higher residual activity is also a major drawback of europium-based neutron absorber, which causes difficulties in handling the spent rod and post-use management[11]. As a result, as far as the author is aware, no (large) fast reactors have used or would use EuB_6

as a neutron absorber in practice.

In summary, although many materials have been proposed in the last several decades, B_4C is still the leading candidate material as the neutron absorber for FBR, because of its excellent neutron capture capability, low residual activity, rich data of usage, and mature fabrication technique.

1.3 Development of the B_4C control rod for the Japanese experimental fast reactor "JOYO"

The Japanese experimental fast reactor "JOYO" is located at the Japan Atomic Energy Agency's O-arai Research and Development Center. JOYO is a reactor to advance the technology through operation and experiment, conduct irradiation tests on fuel and materials; all aimed to accumulate technology for commercialization of FBR. Therefore, naturally, developing reliable, long-life control rods for the future commercial FBR is within the scope of its research.

The neutron absorbers of JOYO are 90% ^{10}B enriched B_4C pellets. The pellets are hot-press sintered and densified to approximately 90% of theoretical density. In the early stages of JOYO, helium-bonding type control rods with B_4C pellets sealed in stainless pipes were used. However, when knew the risk of cladding failure caused by the rise of internal gas pressure, the control rods were changed into a ventable design which solved the gas pressure issue by leaking the helium gas. The ventable helium-bonding control rod is shown in **Figure 1.1.** Otherwise, the ACMI is the main cause of the cladding failure. After newly inserting a B_4C control rod to the reactor core, the B_4C pellets would change in the following steps.

- First, the B_4C pellets are fragmented by the surface-center temperature gradient which caused by the heat when absorbing neutrons.
- The thermal conductivity of the B_4C pellets would be severely reduced by the formation of helium bubbles inside the pellets under neutron irradiation, which deepening the degree of the fragmentation.

- Next, the small fragments relocate in the small reserve gap between the cladding and the pellets. Several patterns of fragment relocations are shown in **Figure 1.2**.
- Then, the neutron irradiation induced swelling of the pellets cause direct stresses to the cladding tube and finally result in the ACMI cladding failure[12–14].

A post-irradiation examination[13] has been done on the MKII core control rods which peak burnups were between 43–56×10^{20} capture/cm^3, cracks of cladding were found on 15 control elements of 8 control rods (each control rod contains 7 control elements), an example of crack is shown in **Figure 1.3**. Moreover, approximately 2% increase in the outside diameter induced by ACMI was confirmed at the bottom part of the controls rods. Although there are no radioactive isotopes production except a trace of tritium in the B_4C pellets when absorbing neutrons and the tritium can easily penetrate the cladding by diffusion, the erosion of the B_4C pellets by the liquid sodium flow is confirmed minor by a 50 days out-side-reactor sodium flow experiment[15], the cracks of claddings should have no significant impact on the reactor. However, due to lack of detailed experimental data on the after-cladding-crack behaviors, and there is no way to detect and slow down the growth of cracks, the burnup limitation of the B_4C control rod tend to be conservative, based on the estimation of the plastic deformation limit of the of the cladding[15]. Hence, the lifetime of the helium-bonding type control rods of JOYO was limited to approximately 50×10^{20} capture/cm^3[13]. While, the theoretical lifetime of the B_4C control rods is expected to be 260×10^{20} capture/cm^3 from the point of view of the ^{10}B consumption[12–16].

Later, in order to prolong the lifetime of the control rods, a sodium-bonding type control rod with a shroud tube covering the B_4C pellets to reduce the relocation of pellet fragments and a function of helium gas venting was developed, which is shown in **Figure 1.4**[13]. Owing to the better thermal conductivity of liquid sodium than helium, the sodium-bonding control rod was allowed to have a broader gap between the pellets and the cladding. Based on the above improvements, the lifetime of the sodium-bonded

control rod was extended to 100×10^{20} capture/cm^3[12]. However, the lifetime is still less than half of the ideal development target, 260×10^{20} capture/cm^3. Therefore, there is a large space for further development of the B_4C control rod for JOYO and the other FBR.

1.4 Previous studies on the neutron irradiation effects on B_4C

1.4.1 Interactions of Neutrons with Crystalline Materials

In general, the iteration of neutron irradiation and substances could be thought briefly into an elastic collision model. Hence, the max energy of the knock-on atom could gain from the neutron, T_m could be expressed by the following equation.

$$T_m = \frac{4A}{(1+A)^2}E \qquad (1.1)$$

Where A is the mass ratio of the colliding neutron and the knock-on atom. E is the kinetic energy of the colliding neutron. When the kinetic energy of the lattice atom gained from the neutron collision T is larger than the displacement energy E_d, then the lattice atom could be knocked out from its original site and leave a vacancy defect. The pair of a vacancy and an interstitial atom is called the Frenkel Pair. Generally, the E_d was qualitatively considered as approximately 25 eV[17, 18]. While the formation energy of the Frenkel Pairs caused by the thermodynamic in many crystals is approximately 5 eV[18]. It is because of to form stable Frenkel Pairs, the knocked-out atoms need to leave their original positions a certain distance which need extra energies[18]. Moreover, if the primary-knock-on atom (PKA) gained enough energy from the neutron collision, other lattice atoms could be displaced by the secondary knock-ons with the PKA, lead to a displacement cascade.

When these point defects continue to accumulate, they tend to form two-dimensional or three-dimensional defect clusters, which are dislocations, void, and interstitial atoms clusters etc., to release the excessive lattice distortion energy. This process mainly relies on the diffusion of the point defects. The diffusion coefficient of

the point defects could be described by the famous Arrhenius's equation. In the case of metals, the equation shows as follows.

$$D = D_0 exp\left(-H_f/kT\right)(-H_m/kT) \qquad (1.2)$$

Where H_f is the formation energy of the point defect, and H_m is the migration energy of the point defect. D_0 is a constant related to the physical properties of the metal. k and T are the Boltzmann constant and temperature, respectively. It is easy to find that the diffusion coefficient increases with increasing temperature. Therefore, at high temperature, the neutron-induced point defects are easier to self-recover or form clusters.

In addition, if the rate of the generation of radiation defects exceeds the threshold, crystalline materials will be converted into amorphous materials. This usually occurs at heavy ion irradiation, which can cause large knock-on cascade zones. Otherwise, a low irradiation temperature also can slow down the diffusion of the point defects, then result in amorphization of materials.

1.4.2 Neutron irradiation effects on B_4C

In the case of B_4C, in addition to the irradiation effects described in 1.4.1, the neutron capture reactions of the ^{10}B isotope also need to be considered. The reactions show as follow.

$$^{10}B + {}^{1}n \rightarrow {}^{7}Li + {}^{4}He + 2.79\ \text{MeV} \qquad (1.3)$$

$$^{10}B + {}^{1}n \rightarrow {}^{7}Li + {}^{4}He + 2.31\text{MeV} + \gamma(0.48\ MeV) \qquad (1.4)$$

The two reactions have possibilities of 6% and 94%, respectively. As the reaction equation shows, a large amount of energy is produced by the neutron capture reaction of ^{10}B, which is mainly in the form of kinetic energy. Obviously, the B_4C suffers more damage than other materials when irradiated by neutrons due to the production high energy Li and He atoms. Except that some of them can be excluded by diffusion, the rest would exist as impurity defects in the B_4C crystal. A brief schematic diagram of the

neutron induced defects in B_4C is shown in **Figure 1.5**.

On the effects of neutron irradiation on the crystal structure of boron carbide, Tucker et al.[19] measure the lattice parameter change of a single crystal boron carbide and boron carbide powder after thermal neutron irradiation by X-ray diffraction in 1950s. They reported a shrinkage in *c*-axis and a slightly expansion in *a*-axis, and this change in lattice parameters returned after annealing at 700–900°C. Later, Hoyt et al.[10] preliminary measured the volume change and helium release of the neutron irradiated B_4C, a significant swelling of approximately 36% was found on a natural B_4C specimen irradiated at a maximum temperature of 250°C with a ^{10}B burnup of 37%. There was only a small amount of helium gas released from the B_4C bulk at that temperature.

In 1970s, due to the development of sodium-cooled fast reactor, further research works on the irradiation defects of B_4C were published. Suzuki et al.[20] carried out a more in-depth study on the lattice parameter change and helium release of neutron irradiated B_4C. Sharp recovery curves of the lattice parameters were observed among the annealing temperature range of 600–900°C, as shown in **Figure 1.6.** Moreover, a large peak of helium release around 800°C and a smaller peak at 1100°C on different neutron irradiated B_4C specimens. The results indicated that the irradiation-induced defects were activated between this range of temperature.

From the same time, transmission electron microscopy (TEM) was also introduced into the study[21–29]. The TEM studies reported the formation of tiny voids and dislocation loops in the neutron-irradiated B_4C crystal. The tiny voids in flat shapes were confirmed in B_4C specimens irradiated under various conditions, and formation of these flat shape voids/bubbles (an example is shown in **Figure 1.7**) was attributed to the high gas pressure caused deforming by Ashbee et al.[25]. However, there is different opinions on the specific direction of the parallel-arranged bubbles in a B_4C crystal. Ashbee[21] observed small defects that were mostly parallel to the traces of the (111) plane in B_4C irradiated in a thermal reactor (Oak Ridge Research Reactor, ORR) at 400°C for 8% burnup (natural B_4C). The shape of bubbles was unclear but appeared to

be elongated ellipses. Ashbee et al.[22], however, latterly reported that the plate-shaped bubbles aligned parallel to the rhombohedral {110} planes of the B_4C specimen after irradiation in the experimental breeder reactor (EBR-II) with up to 3.7% burnup and post-irradiation-annealing at 1900°C for 1 h. Jostsons et al.[26] reported black-spot defects in the as-irradiated natural B_4C specimen up to 1.7% burnup and at an estimated temperature of 500°C in EBR-II. The defects that possessed spherical strain field were deduced as small cavities with ribbon-like shape, with the largest face of the faceted cavity most frequently parallel to the trace of the rhombohedral (111) plane and less frequently parallel to the trace of {100} or {110}. The size of the cavities increased to 3–20 nm by annealing at 1150°C. Furthermore, after further annealing at a higher temperature (1450°C), the lattice strain around the cavities was eliminated, and size of the faceted cavity was further increased and the edges of bubbles were parallel to the traces of (111), {100} and {011}. Jostson et al.[26] observed natural and depleted B_4C specimens irradiated both in thermal (ETR) and fast (EBR-II) reactors at 500–840°C, and with burnups of 1.7-81%. All the bubbles had disc-like morphology surrounded by strain fields, and the plane of the disc was aligned parallel to the (111) planes in the as-irradiated specimen at 800–840°C in EBR-II. The larger bubbles were positioned along the dislocations, stacking faults, and grain boundaries. The grain boundary bubbles appeared more equiaxed. The disk-like morphology of the bubbles appeared less developed in the specimens irradiated at slightly lower temperature (710–735°C). In this case some bubbles were also observed with the {110} plane as the most prominent facet. The specimen irradiated in ETR was similar to the specimens irradiated in EBR-II. However, the specimen irradiated at 550°C with up to 81% burnup (natural B_4C) in the ETR contained only small bubbles without clear shape, and were aligned parallel to the trace of (111). Jostson et al.[27] also mentioned that after annealing at 1400°C, there was a significant increase in the bubbles growth and were more equiaxed; however, the (111) facet was still predominant. The grain boundaries were the preferred sites of bubble agglomeration. The strain fields around the bubbles disappeared. Hollenberg et al.[29] reported the change in the morphology of the helium bubbles irradiated up to

around 62×10^{20} capture/cm^2 across a wide range of irradiation temperature. Further, they concluded that small (diameter less than 10 nm) and high-density lenticular bubbles were homogeneously created at temperatures lower than ~900°C. At temperatures higher than 1500°C, low density, large equiaxed and faceted bubbles were formed heterogeneously. Copeland et al.[24] also observed that the largest face of the plate-like bubbles is most frequently parallel to the trace of the (111) plane, and less frequently parallel to the trace of {100} or {110} rhombohedral planes in the specimen irradiated in EBR-II at 650°C or 730°C up to 10 and 7.7×10^{20} capture/cm^3 burnup, respectively. On the other hand, for the specimens irradiated up to 16×10^{20} capture/cm^3 burnup in the Oak Ridge Research Reactor (ORR) at 350–400°C showed only black-spot defects. Cummings et al.[25] found that almost all the bubbles were parallel to the trace of {110} plane. Basmajian et al.[23] also mentioned that plate-like cavities were observed within a grain associated with both {110} and (111) crystallographic planes for the B_4C specimen irradiated at EBR-II from 427°C to 871°C up to $2–20\times10^{20}$ capture/cm^3. Later, Stoto et al.[30] observed B_4C irradiated in the Phénix fast reactor between 620°C and 1500°C, and they confirmed that the bubbles were parallel only to the (111) plane in his specimens irradiated at 620–1000°C. At 1500°C, the shape of bubbles was changed to a more tridimensional form.

Comparing with the helium, there is few studies on the behavior of neutron produced lithium in the B_4C pellets, because of the lithium is keeping invisible under TEM and being considered less important. Deschanels et al.[31] measured the lithium diffusion coefficient in a dense B_4C pellet, and the lithium was generated inside the B_4C grain by neutron irradiation. The calculated activation energies of lithium diffusion were 0.19 eV for temperature below 948 K, and 0.88 eV for temperature above 948 K, respectively. They are thought respectively mainly attributed to the lithium diffusion in the grain boundaries and inside the grain. However, the results cannot accurately describe the bulk diffusion of lithium in the B_4C grains due to the diffusion in the grain boundaries were always exists in the measurement.

1.5 Objective

With reviewing literature of the previous studies on the neutron irradiation effects on B_4C absorbers, there are still many unknowns remains, such as the favorable plane of the disk-like bubbles parallel with, and the description of the formation mechanism of disk-like morphology of bubbles was ambiguous, and most of the data was collected from the specimen irradiated at the environment with constant neutron flux and temperature. To further the understanding on the neutron irradiation effects on the B_4C absorber and develop a new reliable long-life B_4C absorber for FBR, the following questions are needed to be addressed.

1. How would the changing irradiation environment of an actual control rod of a FBR affect the B_4C pellet?
2. Why do the helium form bubbles in a flat disk-like shape?
3. Could the anisotropic reactions of B_4C under the neutron irradiation be utilized to improve the performance of the pellet?

This research is conducted in order to answer the above questions. X-ray diffraction, transmission electron microscopy, first-principle calculations based on density functional theory are used to investigate the neutron irradiation effects on the B_4C pellets from a retired control rod of JOYO.

References

1. Fetter S. How long will the world's uranium supplies last? 2009 [cited 2017 Nov. 27]. Available from: https://www.scientificamerican.com/article/how-long-will-global-uranium-deposits-last/.

2. Key world energy statistics 2017. IEA; 2017.

3. World Energy Outlook 2016 EXECUTIVE SUMMARY. IEA; 2016.

4. Cohen BL. Breeder reactors: A renewable energy source. Am J Phys. 1983;51:75-6.

5. Shibata K, Iwamoto O, Nakagawa T, Iwamoto N, Ichihara A, Kunieda S, Chiba S, Furutaka K, Otuka N, Ohsawa T, Murata T, Matsunobu H, Zukeran A, Kamada S, Katakura J. JENDL-4.0: A New Library for Nuclear Science and Engineering. Journal of Nuclear Science and Technology. 2011;48:1-30.

6. Nuclear Reactor Materials Handbook: Nikkan Kogyo Shimbun; 1977.

7. Paul CSW. Europia as a Nuclear Control Material. Nuclear Technology. 1978;39:84-94.

8. Wang M, Xiao H, Liu C, Wu Y, inventors; Hefei Institutes of Physical Science, Chinese Academy of Sciences, assignee. Control rod for liquid heavy metal cooling reactor. China patent CN103236276 (B). 2013 Apr. 21.

9. Mahagin DE. Fast-Reactor Neutron Absorber Materials. Am Ceram Soc Bull. 1979;58:393-.

10. Hoyt EW, Zimmerman DL. Radiation Effects in Borides: Part I—Helium release and swelling in irradiated borides. San Jose, California: Vallecitos Atomic Laboratory, General Electric Company, 1962 Feb. 13.

11. Gosset D. Absorber materials for Generation IV reactors. Structural Materials for Generation IV Nuclear Reactors2017. p. 533-67.

12. Donomae T, Katsuyama K, Tachi Y, Maeda K, Yamamoto M, Soga T. Reduction in Degree of Absorber-Cladding Mechanical Interaction by Shroud Tube in Control Rods for the Fast Reactor. Journal of Nuclear Science and Technology. 2011;48:580-4.

13. Soga T, Tobita K, Mitsugi T, Miyakawa S. The Development of a Sodium Bonded Type Control Rod in Joyo. Japan Nuclear Cycle Development Institution, 2000. (no. 1344-4239).

14. Sasaki S, Maeda K, Furuya H. Irradiation performance of sodium-bonded control rod for the fast breeder reactor. Journal of Nuclear Science and Technology. 2017:1-7.

15. Miyakawa S, Soga T, Takatsudo Y. Development of JOYO MKII control rod and the evaluation of actual use. Ibaraki, Japan: Power reactor and nuclear fuel development corporation, 1997. (no. PNC TN9410 97-068).

16. Soga T, Miyakawa S, Mitsugi T. Advancement of control rod of JOYO: Design of sodium-bonding type control rod. Japan Nuclear Cycle Development Institute, Technical Cooperation Section TMD; 1999. (no. JNC TN 9400 99-052).

17. Shiraishi K, Yamaoka H, Kinoshita C, Koyama A. Radiation effect and materials. Japan: Shokabo Co., Ltd; 1994.

18. Kobayashi A, Miyazawa H, Hatoyama M, Kainuma Y, Uemura Y, Iwata S, Suita T, Kojima T, Hashiguchi R, Mizuki E. Interfacial Phenomena and lattice defects. Japan: Kyoritsu Shuppan Co., Ltd.; 1959.

19. Tucker CW, Senio P. X-ray scattering by neutron-irradiated single crystals of boron carbide. I. Acta Crystallographica. 1955;8:371-8.

20. Suzuki H, Maruyama T, Wakasa T. Postirradiation Annealing of Boron Carbide Pellet Irradiated in Fast Breeder Reactor. Journal of Nuclear Science and Technology. 1979;16:588-95.

21. Ashbee KHG. Defects in Boron Carbide before and after Neutron Irradiation. Acta Metall. 1971;19:1079-&.

22. Ashbee KHG, Frank FC, Dubose CKH. Voids in Boron Carbide. J Nucl Mater. 1973;48:193-8.

23. Basmajian JA, Pitner AL, Mahagin DE, Ripfel HCF, Baker DE. Irradiation Effects in Boron Carbide Pellets Irradiated in Fast Neutron Spectra. Nuclear Technology. 1972;16:238-48.

24. Copeland GL, Donnelly RG, Martin WR. Irradiation Behavior of Boron Carbide.

Nuclear Technology. 1972;16:226-37.

25. Cummings WV, Laidler JJ, Mahagin DE, Mastel B. Microstructure of Fast-Reactor-Irradiated Boron Carbide. T Am Nucl Soc. 1972;15:742-+.

26. Jostsons A, Dubose CKH. Microstructure of Boron Carbide after Fast-Neutron Irradiation. J Nucl Mater. 1972;44:91-&.

27. Jostsons A, Dubose CKH, Copeland GL, Stiegler JO. Defect Structure of Neutron-Irradiated Boron-Carbide. J Nucl Mater. 1973;49:136-50.

28. Hollenberg GW, Cummings WV. Effect of Fast Neutron Irradiation on the Structure of Boron Carbide. J Am Ceram Soc. 1977;60:520-5.

29. Hollenberg GW, Mastel B, Basmajian JA. Effect of Irradiation Temperature on the Growth of Helium Bubbles in Boron-Carbide. J Am Ceram Soc. 1980;63:376-80.

30. Stoto T, Housseau N, Zuppiroli L, Kryger B. Swelling and Microcracking of Boron-Carbide Subjected to Fast-Neutron Irradiations. J Appl Phys. 1990;68:3198-206.

31. Deschanels X, Simeone D, Bonal JP. Determination of the lithium diffusion coefficient in irradiated boron carbide pellets. J Nucl Mater. 1999;265:321-4.

32. Fast Reactor Database 2006 Update. Vienna, Austria: IAEA; 2006.

Table 1.1 Absorber materials of commercial size fast reactors (design)[32]

Plant	Absorber pins		
	Material of neutron absorber (safety)	Group 1	Group 2
Super-Phénix 1 (France)	BC90	BC90	–
Super-Phénix 2 (France)	BC90	BC90	BC90
SNR 2 (Germnay)	–	B90	B90
DFBR (Japan)	BC92	–	–
CDFR (UK)	BC30	–	BC20
BN-1600 (Russian Federation)	BC80	BC80	BC80
BN-800 (Russian Federation)	BC92	BC20	BC60
EFR	BC30, 45, 90	BC30,45,90	BC30, 90*
ALMR (USA)	–	BC20	–
SVBR-75/100 (Russian Federation)	BC50	BC50	BC50
BN-1800 (Russian Federation)	BC92	–	–
BREST-1200 (Russian Federation)	to be determined		
JSFR-1500 (Japan) Breeding core	BC80	BC80	BC80
JSFR-1500 (Japan) Break even core	BC80	BC80	BC80

(If B_4C is used it is abbreviated below as BCx, where x is the enrichment (%^{10}B) and if boron powder or sintered powder is used it is abbreviated as Bx)
*control and shutdown rods/diverse shutdown rods

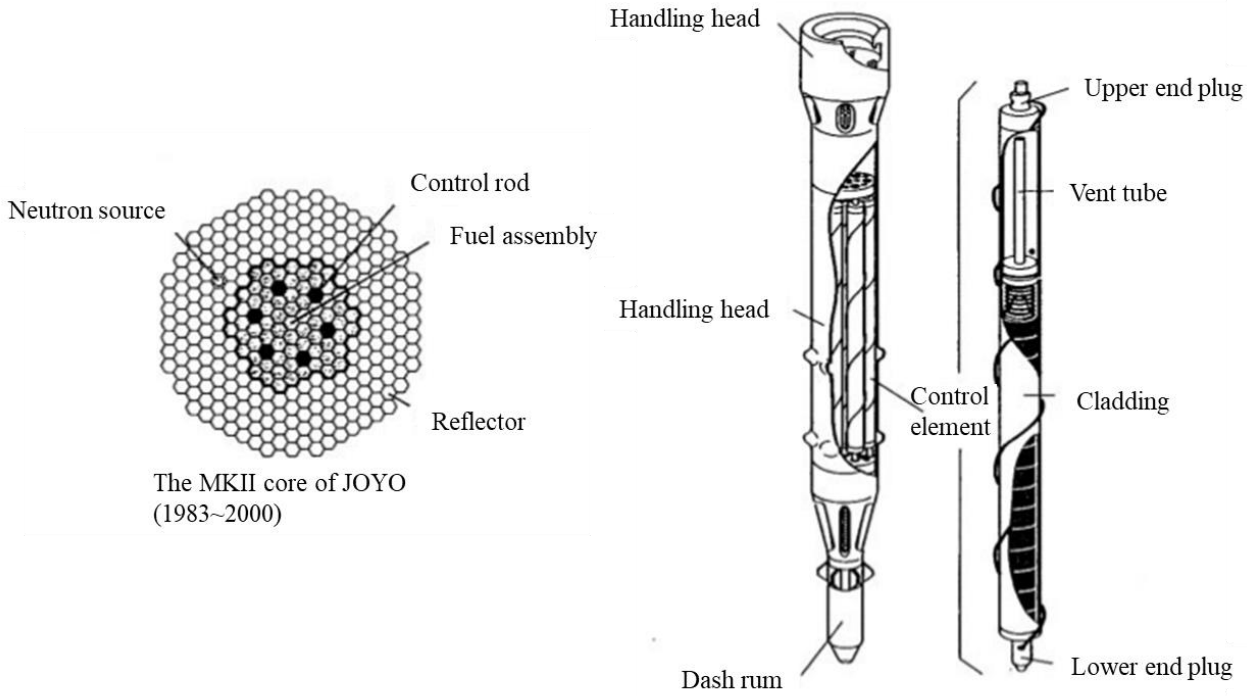

Figure 1.1 The MKII core configuration of JOYO and the structure of the helium-bonding control rod used in the MKII core[15].

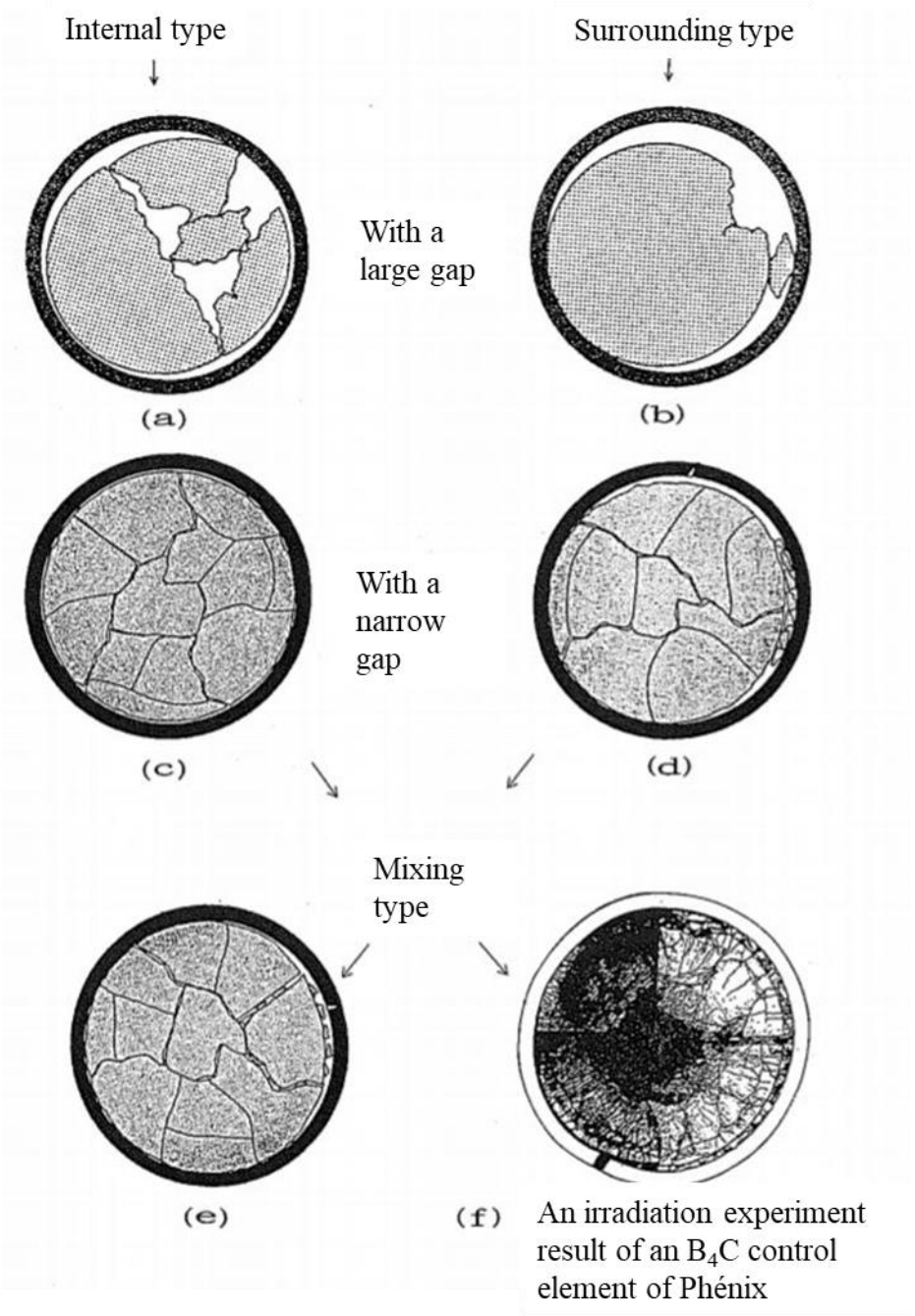

Figure 1.2 Different patterns of the relocations of the pellet fragments[15].

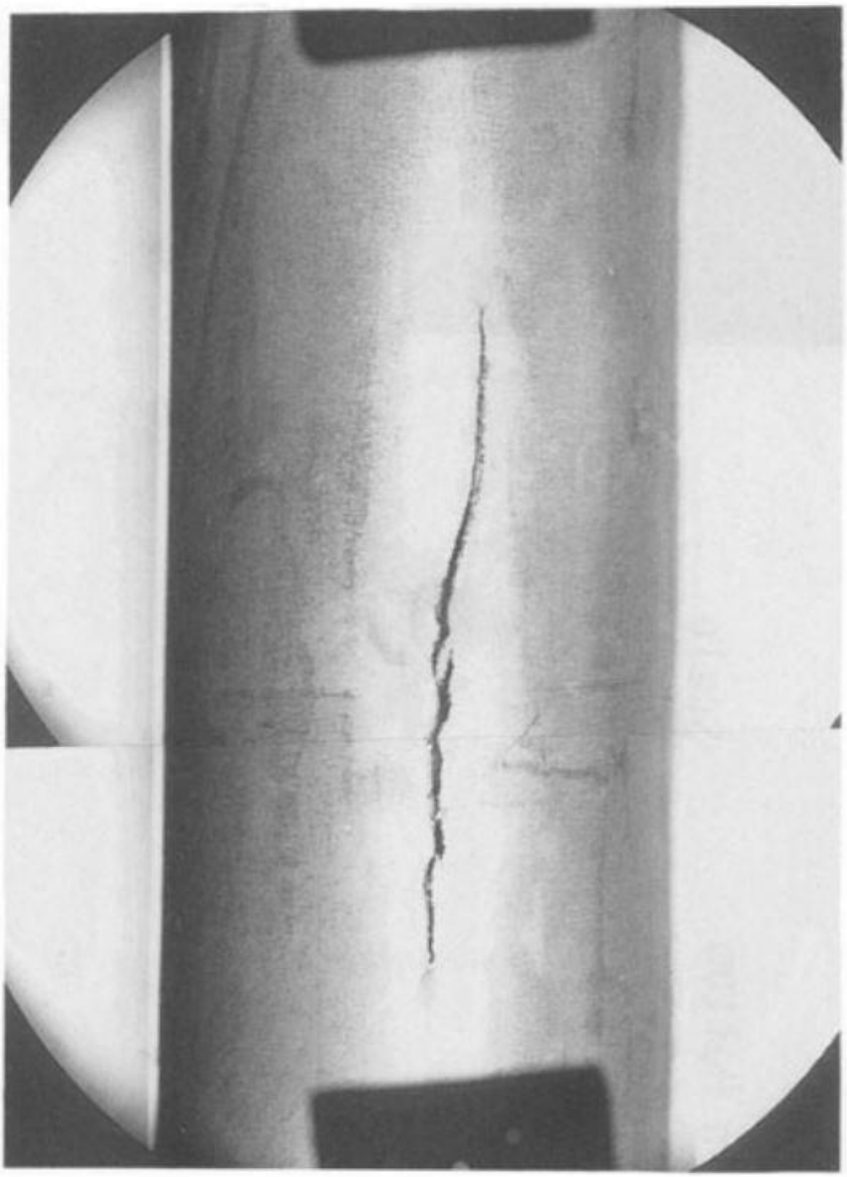

Figure 1.3 An example of a crack on cladding[14].

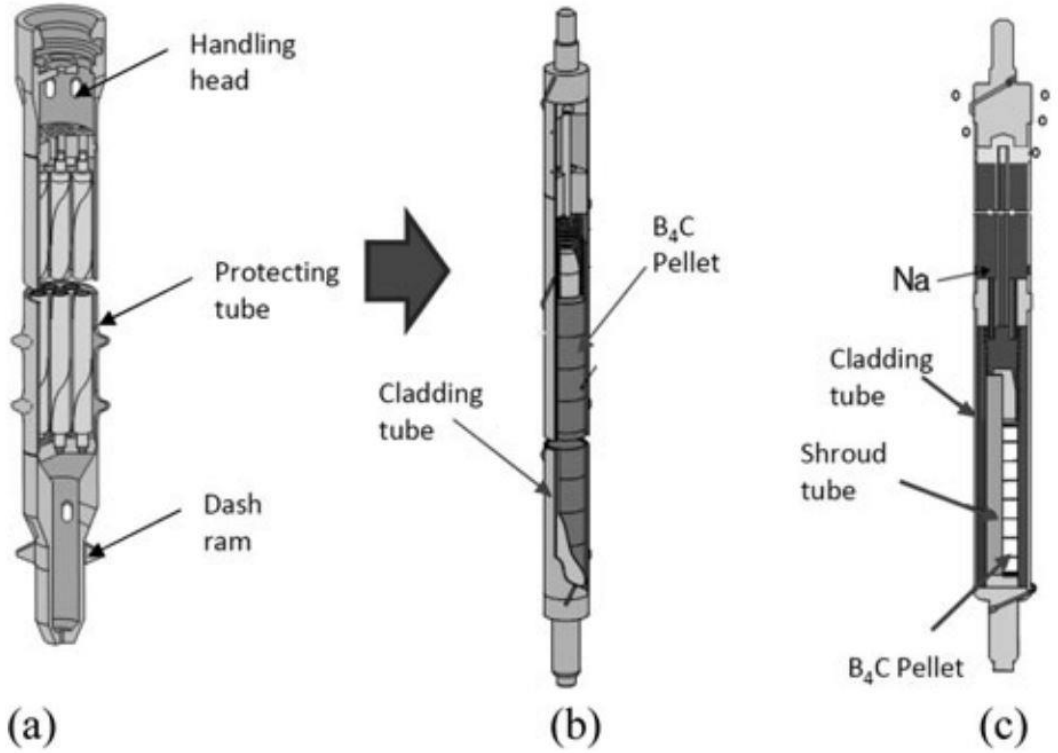

Figure 1.4 A schematic diagram of the sodium-bonding control rod[14].

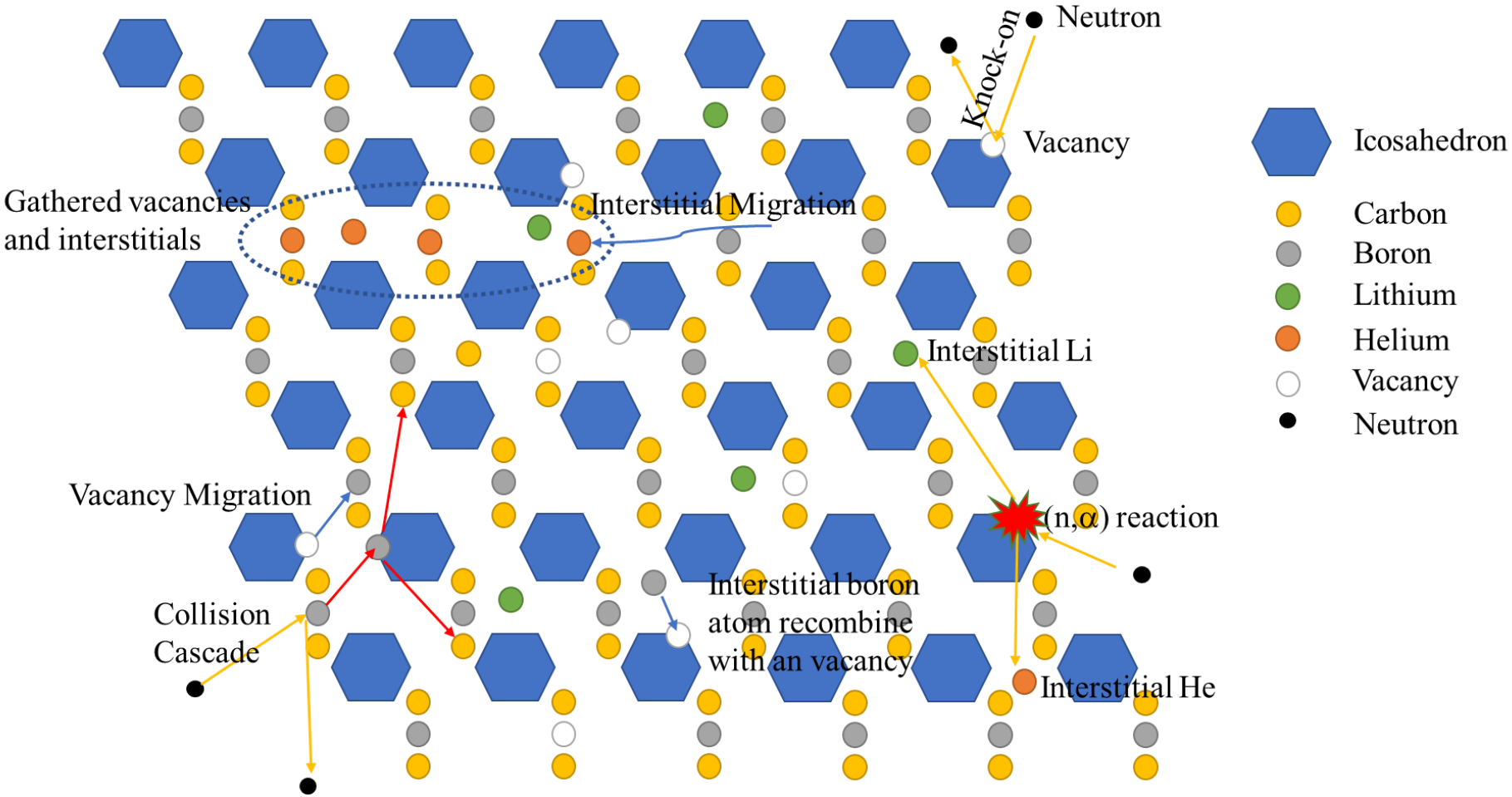

Figure 1.5 A schematic diagram of the neutron-induced defects in B_4C

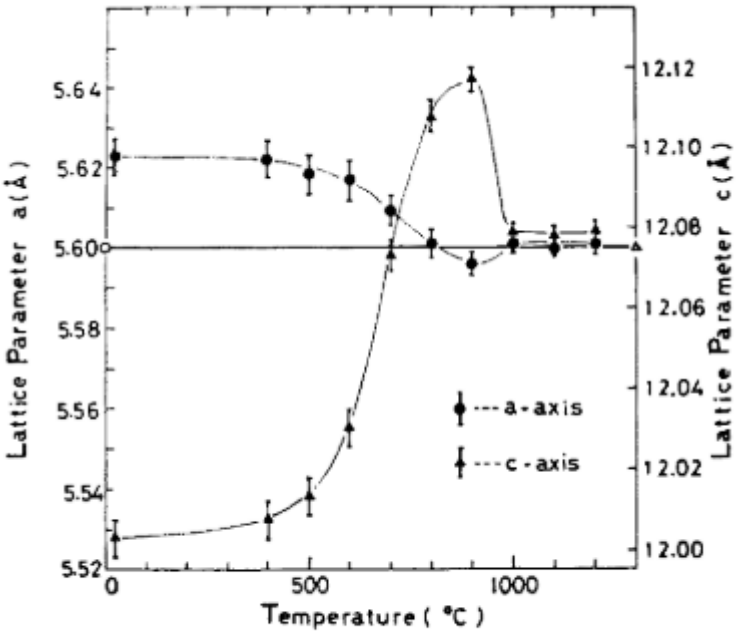

Figure 1.6 Lattice parameters changes of a B_4C pellet (4.1×10^{20} capture/cm^3) with annealing temperature[20]

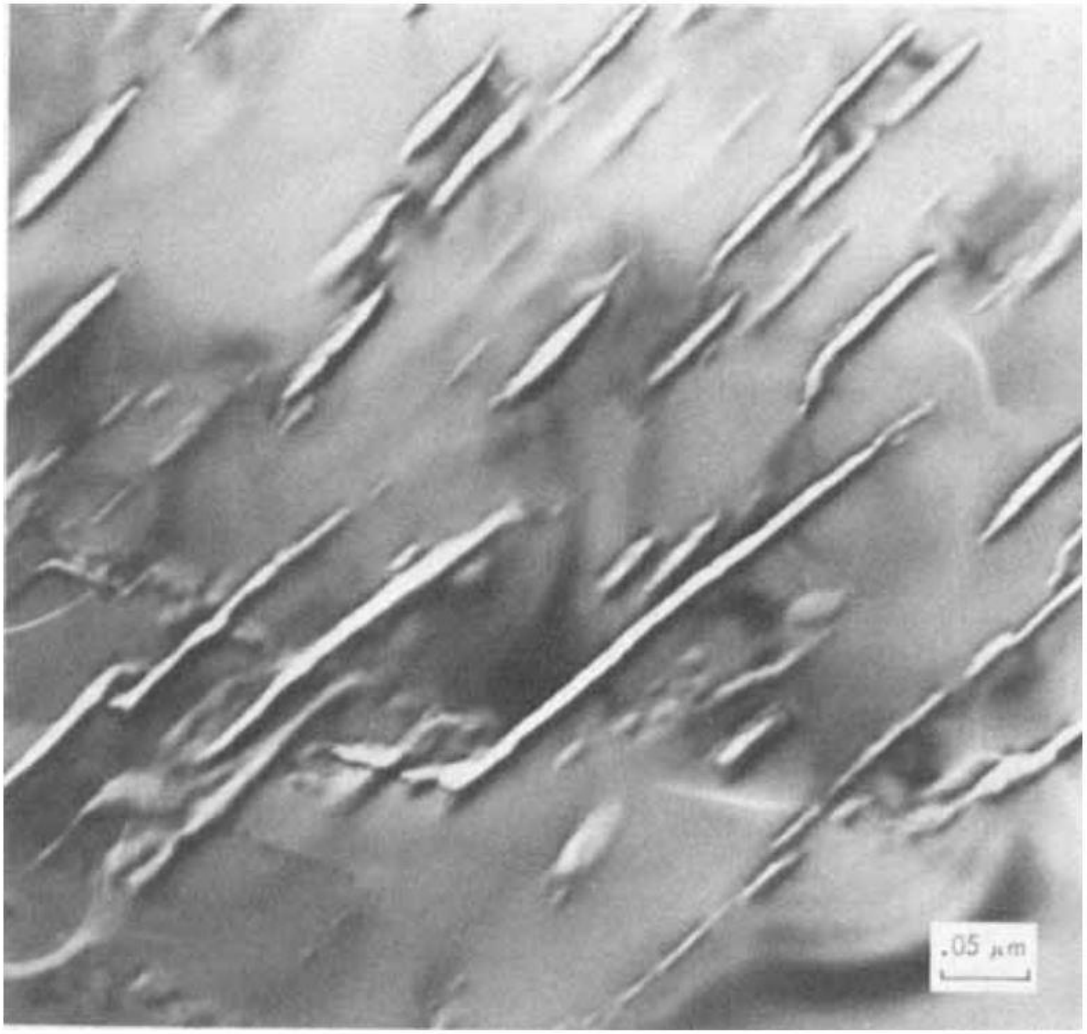

Figure 1.7 Voids in a B_4C pellet irradiated at 700°C to 21×10^{20} capture/cm^3[28]

CHAPTER 2
Neutron Irradiated B_4C samples for experiments

This chapter states the basic information of the neutron-irradiated B_4C samples investigated in this research, including the manufacturing specifications of the B_4C pellets, the estimated irradiation temperature and burnup distribution, and the appearance of the as-received cracked pellets. Additionally, the neutron features of the "JOYO MKIII" experimental reactor which is helpful to understand the irradiation process of the B_4C pellets will also be introduced.

2.1 Manufacturing information of the B_4C pellets

The irradiated B_4C pellets were supplied by Japan Atomic Energy Agency and were taken from a retired control rod (CR0901) of the JOYO MKIII reactor. The B_4C pellets were fabricated by hot-press sintering without sintering additives and achieved densification of approximate 90% of the theoretical density. The detailed specifications of pellets are shown in **Table 2.1**. The raw B_4C powder used for the pellet sintering is enriched to a ^{10}B abundance of 90%. A quality inspection report of the very batch of the raw B_4C power was provided by Omuta plant, Denki kagaku kogyo co. ltd. The results are shown in **Table 2.2**.

2.2 Neutron irradiation conditions of the B_4C samples.

The B_4C pellets were loaded in an actual control rod of JOYO MKIII, except for one

sample, the K711b41 sample used for TEM observations was irradiated in an Absorber Material Irradiation Rig (AMIR) of JOYO. The core configuration of JOYO MKIII is shown in **Figure 2.1**. One power operation cycle of JOYO MKIII is up to 60 effective full power days, then stop for approximately 19 days. The control rod CR0901 had experienced 5 cycles, approximately 279 effective full power days in the reactor. In order to maintain the same degree of burnups for all control rods, the position of the control rods may exchange after one operation cycle. The key features of the JOYO MKIII core are shown in **Table 2.3** and **Table 2.4**.

Due to the and the heat generation of the neutron capture reactions of B_4C pellets, there are large temperature gradients between the pellet center and the coolant contact surface, which resulted in large thermal stresses. Moreover, the neutron irradiation, mostly the production of helium, weakened the strength of the B_4C pellet simultaneously. Consequently, the B_4C pellets were fragmented into small pieces, wherein the ones have a greater temperature gradient and higher burnup were broken into smaller fragments. The burnup and the temperature of the B_4C pellet are obtained by the JOYO MKIII core management code system "HESTIA"[1]. The estimation results are shown in **Figure 2.2** and **Figure 2.3**. Obviously, the pellets at the bottom of the control element have the greatest temperature gradient and the highest burnup, because the bottom part of a control rod is the most frequently inserted into the reactor core. The sample r001b21 originally at the bottom of the control element was completely broken in small fragments, as shown in **Figure 2.4**. It is easy to find there is a negative correlation between the fragments sizes and their burnup. In addition, it should be noted here that in order to control the power of the reactor, the control rods in operation will adjust the position of insertion and removal. This caused a non-constant irradiation temperature and neutron flux on the B_4C absorber pellets.

A macroscopic examination of the fracture surfaces of these fragmented pellets was conducted with a Scanning Electron Microscope (S-3500, Hitachi). As shown in **Figure 2.5**, the fracture surfaces of the unirradiated sample cracked with a hammer and the lowest burnup sample r001_33 (below 10×10^{20}capture/cm^3) show characteristics of

intragranular fracture. However, in the case of the higher burnup samples, the r001c21 (approx. 30×10^{20} capture/cm^3) and r001b21 (approx. 80×10^{20} capture/cm^3) show significant characteristics of intragranular fracture on the fracture surfaces. This might because of the neutron irradiation have a greater impact on the binding strength of the grain boundaries than on the strength of the B_4C grains.

The sample K711b41 was irradiated in an AMIR, which have relatively constant temperature and neutron flux. The fragment of sample K711b41 are relatively complete comparing to the sample r001c21, and the burnup is slightly higher than the sample r001c21. Figure 2.6 shows the appearance of sample K711b41 and its irradiation information.

References

1. Okawachi Y, Maeda s, Sekine T, Nagasaki H. Development of JOYO MK-III core management code system "HESTIA". Japan Nuclear Cycle Development Institue, 2003 Jan. (no. JNC TN9400 2002-070).

2. Typical Core Configuration Japan: Japan Atomic Energy Agency; [cited 2017 Dec. 6]. Available from: https://www.jaea.go.jp/04/o-arai/joyo_users_guide/joyomk3/performance/index.html.

3. Radial Distribution of Fast Neutron Flux in the Core: Japan Atomic Energy Agency; [cited 2017 Dec. 6]. Available from: https://www.jaea.go.jp/04/o-arai/joyo_users_guide/joyomk3/distribution/index.html.

Table 2.1 Specification of a sample of the B_4C pellets for the CR09xx control rods.

	Diameter (mm)			Hight (mm)	Weight (mm)	Density (g/cm^3)	Relative density (% T.D.)
Specification / Pellet No.	16.30 (+0, -0.10)			50.00 ±0.20 mm			90.0±2.0 (T.D. 2.3836 g/cm^3)
	x-axis	y-axis	Avg.				
P90127	16.26	16.26	16.26	50.10	22.510	2.167	90.9

Table 2.2 Test results for the B_4C powder of P9 lot.

Test item	Quality standard	No.1	No.2
^{10}B abundance (at%)	90.0±1.0	90.1	90.1
Total Boron (wt%)	77.0±1.0	76.8	76.7
Total (B+C) (wt%)	≥99.0	99.2	99.3

Table 2.3 Key features of the JOYO MKIII core[2].

Reactor power	140 MWt
Maximum fast neutron flux (E≧0.1MeV)	4.0×10^{19} n·m^{-2}·s^{-1}
Primary coolant flow rate	2700 t/h
Coolant temperature (Inlet/Outlet)	350°C/500°C
Core height	500 mm
Number of fuel subassemblies	85 in maximum
Reflector/Shielding subassembly	Stainless steel/B_4C
Installable number of irradiation rigs	21 in maximum
Pitch between subassemblies	81.5 mm
Length of the rated power operation cycle	60 days/cycle in maximum

Table 2.4 Neutron flux in JOYO MKIII core[3].

Row installed	Maximum fast neutron flux ($n\cdot m^{-2}\cdot s^{-1}$)	Fast neutron fluence per 1 operation cycle ($n\cdot m^{-2}$)	Maximum total neutron flux ($n\cdot m^{-2}\cdot s^{-1}$)	Total neutron fluence per 1 operation cycle ($n\cdot m^{-2}$)
0	3.9×10^{19}	2.0×10^{26}	5.6×10^{19}	2.9×10^{26}
1st	3.9×10^{19}	2.0×10^{26}	5.6×10^{19}	2.9×10^{26}
2nd	3.8×10^{19}	2.0×10^{26}	5.3×10^{19}	2.7×10^{26}
3rd	3.4×10^{19}	1.8×10^{26}	4.8×10^{19}	2.5×10^{26}
4th	2.9×10^{19}	1.5×10^{26}	4.1×10^{19}	2.1×10^{26}
5th	2.2×10^{19}	1.1×10^{26}	3.2×10^{19}	1.7×10^{26}
6th	1.4×10^{19}	0.7×10^{26}	2.3×10^{19}	1.2×10^{26}

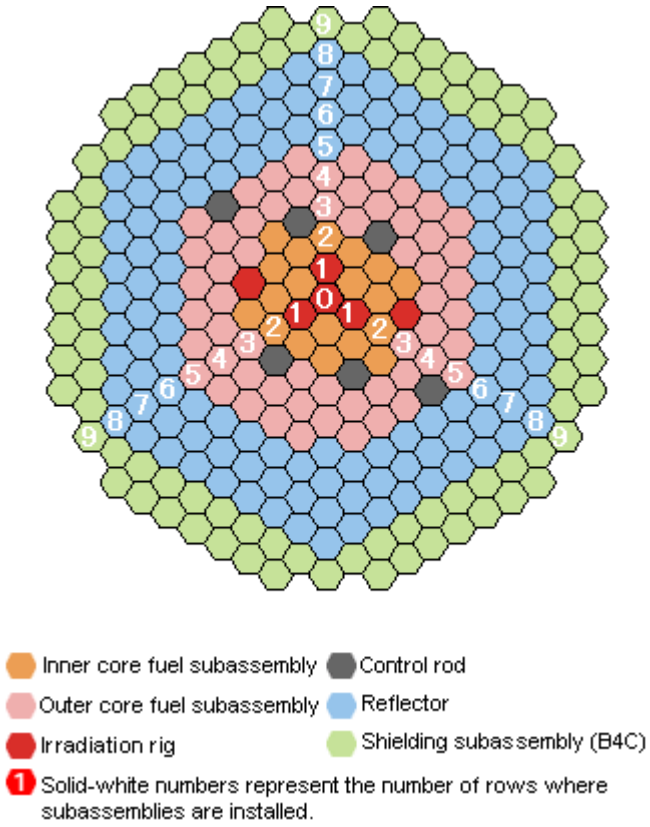

Figure 2.1 Typical core configuration of JOYO MKIII[2]

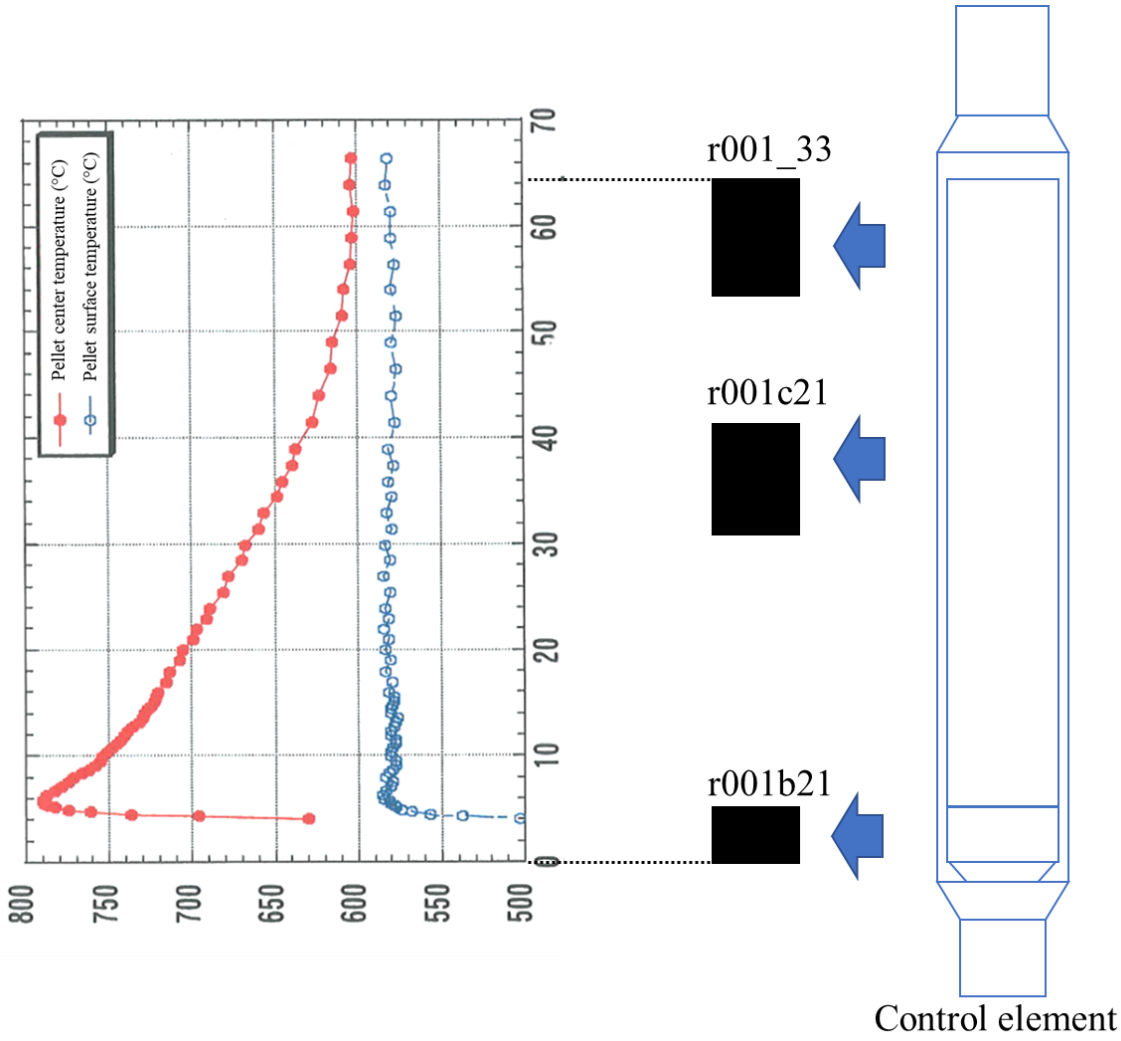

Figure 2.2 The temperature distribution of the B_4C pellets in JOYO MKIII core.

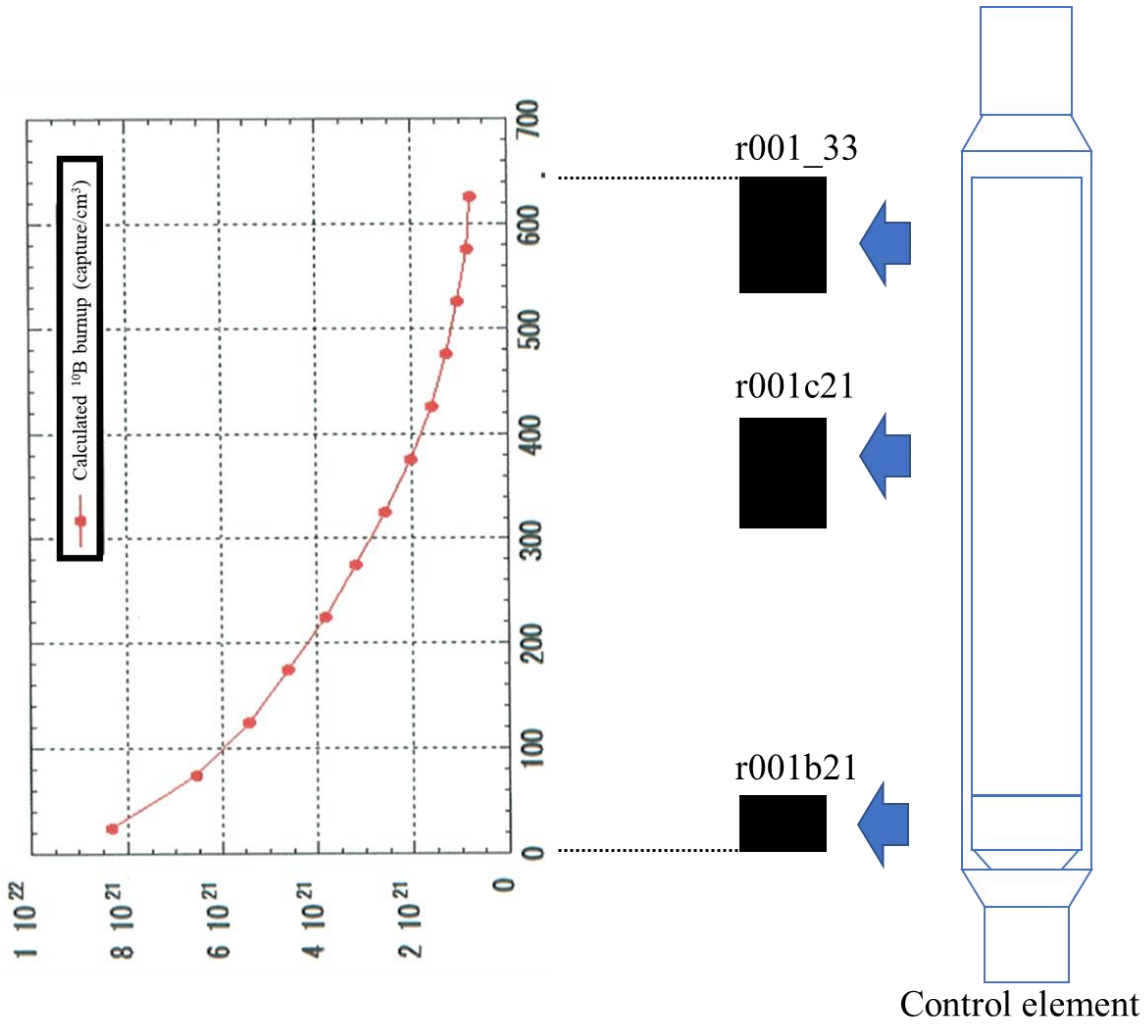

Figure 2.3 The burnup distribution of the B_4C pellets in JOYO MKIII core.

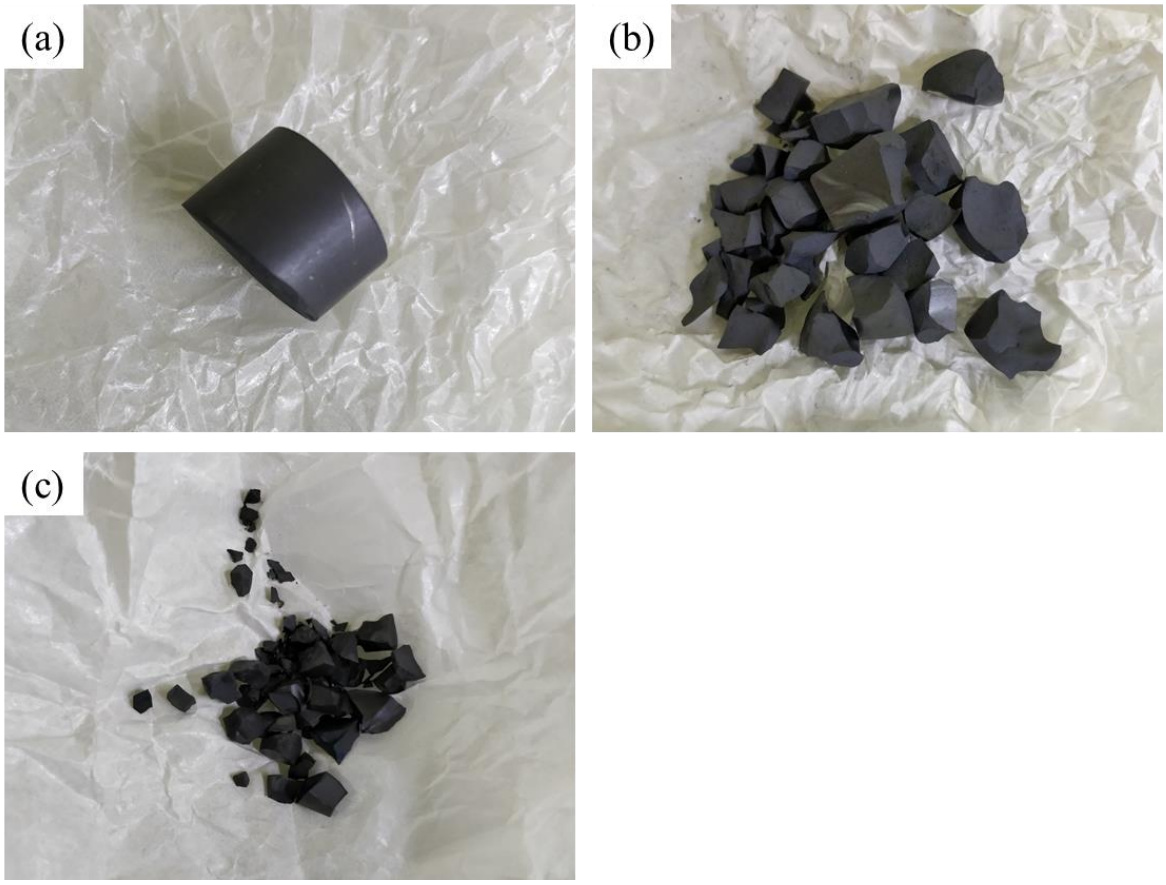

Figure 2.4 The as received B_4C pellet samples. (a), (b), (c) are sample r001_33, r001c21, r001b21, respectively, following the order of burnup from low to high.

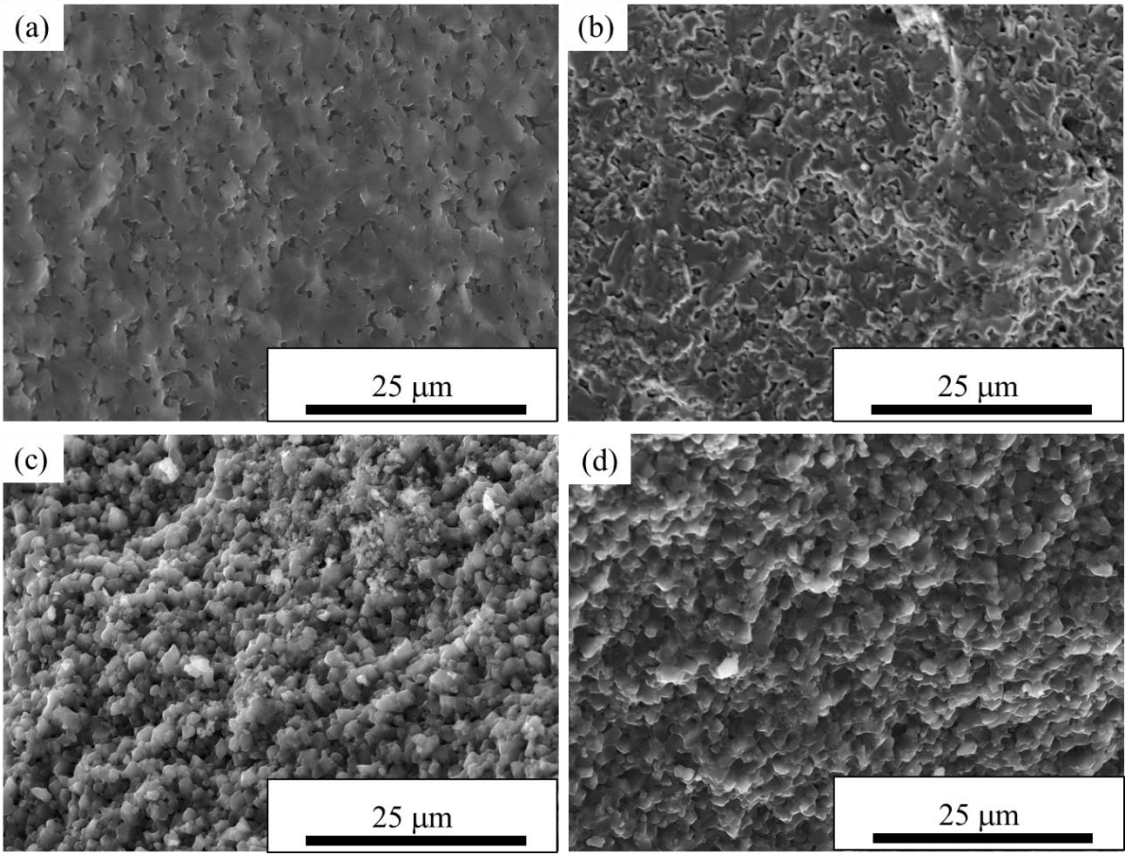

Figure 2.5 The fracture surface of (a) unirradiated B_4C cracked with a hammer, (b) sample r001_33, (c) sample r001c21, (d) sample r001b21.

Density (% T.D.)	95
^{10}B abundance (wt%)	90
Burnup ($\times 10^{20}$ capture/cm^3)	30.1
Irradiation Temp. (°C)	800

Figure 2.6 The appearance and the irradiation information of the sample K711b41.

CHAPTER 3
XRD analysis of the neutron-irradiated B_4C

3.1 Introduction

During neutron irradiation, a lot of Frenkel Pairs were created in the B_4C crystal; helium and lithium were produced by the $^{10}B(n, \alpha)^7Li$ reaction. The accumulation of these defects would distort the lattice of B_4C, or even make the B_4C grains partially amorphized. Moreover, due to the lattice atoms are not stationary but are vibrating, the atoms jumping probabilistically to the nearby interstitial sites and vacancies by thermal energy, causing the diffusion of the defects. Due to the diffusion of these defects, some of these existing defects may vanish by the recombination of Frenkel Pairs or migrating to the sinks to achieve a low total energy. Accordingly, the distortion of the lattice could get a certain recovery by heat the defective sample to a high temperature to accelerate the diffusion of the defects. Hence, a reasonable high-temperature environment is favorable to inhibiting the swelling of the B_4C pellets in a nuclear reactor.

To obtain a first understanding on the impact of the neutron-induced defects to the lattice and the effect of temperature, the X-ray diffraction (XRD) examination was the first method we took. In this chapter, the neutron-irradiated B_4C samples were analyzed with X-ray powder diffraction. Furthermore, with combinations of XRD analyze, the neutron-irradiated B_4C samples were annealed by steps up to 1000°C to understand the recovery behavior of the irradiation defects in B_4C.

3.2 Experimental details

3.2.1 X-ray diffraction measurement

The neutron irradiated B_4C pellet samples with relatively high burnup, r001c21 (approx. 30×10^{20} capture/cm^3) and r001b21 (approx. 80×10^{20} capture/cm^3), were selected in the experiment to compare with the reserved unirradiated B_4C absorber pellet. Because of the as-received neutron irradiated B_4C samples are completely fragmented, several fragments were picked from each sample without selectivity, and be crushed into fine powder to obtain the average data of the pellet. It would be interesting to investigate how the temperature gradient between the pellet center and surface during irradiation affect the microstructure of B_4C. However, due to the severe fragmentation, it is hard to tell where each fragment was in the original pellet. Therefore, we can only try to get the average results of each sample. The B_4C fragments were crushed in a B_4C mortar because of its super hardness nature. Although some small B_4C debris from the mortar may be mixed into the sample during the grinding process, such a small amount should not affect the experimental results.

The XRD patterns were recorded with a Philips PW-1700 automatic powder diffractometer (Netherlands) at room temperature (approx. 25°C). The X-ray was filtrated by a Ni Kβ filter, the Cu Kα1 radiation (λ=1.54059 Å) was used. The Kα2 was striped by software with Rachinger's Kα2 correction[1].

The internal standard was silicon powder. The scan parameters are listed as follow:

Scan mode: step scan

Acceleration voltage: 40 kV

Electron Current: 40 mA

Scan range: 15°–75°

Step width: 0.02°

Scan speed: 0.02° per 5 s

The lattice parameters were calculated from the (110), (021), (205), and (303) plane of B_4C with the least squares method.

3.2.2 Post-irradiation annealing

To study the irradiation defects recovery behavior of B_4C, we carried out a post-irradiation annealing test on powder specimens of the neutron irradiation B_4C. The post-irradiation annealing experiment was implemented by the electric furnace of a DIL402C dilatometer (NETZCH, Germany), with an argon atmosphere. The annealing temperatures were 300°C, 500°C, 600°C, 700°C, …, 1000°C; each temperature was kept for 1 h and then cooled to room temperature for measuring the lattice parameters. The heating rate was 10°C/min. A flow diagram of the experiment is shown in **Figure 3.1**.

3.3 Results and discussion

3.3.1 Comparison of specimens with different burnups

Firstly, the XRD patterns of the neutron-irradiated samples r001b21, r001c21, and the unirradiated sample are as shown in **Figure 3.2**. The unirradiated sample shows sharp peaks, while the irradiated samples show very broadened peaks. Some of the peaks' positions also occurred slight shifting which reflected the calculation results of the lattice parameters. The calculated lattice parameters are shown in **Table 3.1**. After neutron irradiation, the lattice parameter *a* slightly expanded for 0.29% in specimen r001c21, 0.18% in specimen r001b21, respectively. However, there are shrinkages in the lattice parameter *c*, -1.16% in specimen r001c21, -0.66 % in specimen r001b21, respectively. The volume changes of the unit cell of r001c21 and r001b21 are -0.63% and -0.29%, respectively.

By comparison of the positions and the widths of the peaks, it is easy to find that

the peaks of the planes associated with the hexagonal [001] axis have larger shifting and broadening, such as the peaks of (003) and (104); while the peaks nearly perpendicular to plane (001) have much smaller broadening, such as the peaks of (110) and (021). The comparison of the peaks of the plane (104) and plane (021), two of which have relatively high intensity is shown in **Figure 3.3** and **Figure 3.4**, respectively. For the peak (104), the width increased by 168% in specimen r001c21, and increased by 131% in specimen r001b21. For the peak (201), the broadenings are much smaller than that of peak (104), which are 54% in specimen r001c21, and 61% in specimen r001b21, respectively. Neither the broadenings in XRD peaks nor the changes in lattice parameters increase as the degree of the burnup increased.

3.3.2 Effects of post-irradiation annealing

Recovery in the lattices parameters as a function of annealing temperature was confirmed. The recovery behaviors in parameter a, c, and cell volume V are shown in **Figure 3.5**, **Figure 3.6**, and **Figure 3.7** with comparisons to the previous reported results by Suzuki et al. [2], respectively. As the dashed lines show the original lattice parameter of the unirradiated specimen, the low burnup specimen r001c21, and the high burnup specimen r001b21 showed similar recovery curves, and the lattice parameters almost recovered to the original value in both *a* and *c* axis. The lattice parameters reported by Suzuki et al.[2] are slightly larger than our results, which is approximately 0.015 Å larger in *a* axis and 0.05 Å higher larger in *c* axis, respectively. It is because the burnup of the Suzuki's specimen was much lower than our specimens, which was only 4.1×10^{20} capture/cm^3. However, the tendency of recovery by post-irradiation annealing is consistent with our results. The recovery in *a* axis started from 500°C, while in *c* axis the recovery started latter from 800°C. The biggest difference between the lattice parameter recovery of the two specimens is after annealed at 1000°C, the lattice parameter *a* of r001b21 shrank to smaller than that of unirradiated specimen whereas the specimen r001c21 was almost the same with the unirradiated specimen in

a axis. We considered this as a consequence of the higher boron burnup in r001b21 which induced a high concentration of vacancy defects in the B_4C crystal.

Figure 3.8 and **Figure 3.9** show the changes in the breadth of the peaks of the plane (104) and (021) after annealing. Although it is not significant, the peak breadth narrowed slightly after annealing at 1000°C. Both the peaks of the plane (104) and (021) narrowed by approximately 16%. Our results agree well with the reports from Suzuki et al.[2] which the recovery in line broadening does not occurred untiled annealed at 900°C. However, Simeone et al.[3] reported there is no significant evolution until 1600°C.

3.3.3 Discussion

The measured anisotropic changes in lattice parameters, which shrink in *c*-axis and slightly expands in *a*-axis, agrees well with the previous studies on neutron irradiated B_4C[2, 3]. This anisotropic reaction is considered due to the absence of atoms on the C-B-C atomic chains along with the *c*-axis, which causes the chains shrink and then consequently cause lattice cell shrinkage in the *c*-axis. The slight expansion in a-axis is probably caused by the lattice atoms been knocked out into interstitial sites or the reaction products (Li, He) in interstitial sites. Moreover, it is very strange that the changes in lattice parameters of the high burnup specimen r001b21 are smaller than that of the lower burnup specimen r001c21 which was supposed fewer irradiation defects had been generated. The only considerable reason is that due to the higher irradiation temperature of the r001b21 specimen, the irradiation-induced defects were more mobile and many of them had migrated to the sinks such as the grain boundaries that do not affect the lattice parameters. TEM observation results in Chapter 4 show wider grain boundaries with large helium bubbles in the r001b21 specimen than the grain boundaries in the r001c21 specimen.

Before discussing the line broadening in the XRD peaks of the neutron-irradiated B_4C samples, it should be noted that the XRD peaks are accurately reflecting

the degree of the orderly atomic arrangement in the materials. If a perfect crystal has a completely orderly arranged structure measured by an ideal XRD instrument, the XRD peaks would be recorded as straight lines and the 2 theta angels are related to their associated plane spacing. However, in reality, the XRD instrument has inherent errors and there are defects in crystals which would distort the lattice to some extent, wherefore the lines are broadened to peaks. Hence, we can consider the degrees of the peak broadening as the degrees of the average lattice distortion of the associated planes.

Generally, the reasons cause the line broadening of the peaks are micro-strains, surface relaxation effect of the small-size crystalline domain, incompleteness of crystal, and stacking faults. Due to there was no significant increase in stacking faults depending on the TEM observations, the stacking faults may be excluded from consideration. In the neutron-irradiated B_4C, numerous tiny helium bubbles formed in the gains that divide the intact crystalline grain into many small crystalline domains, as a schematic diagram is shown in **Figure 3.10**. The interface atoms contacted with the helium bubbles would relax to some extent, and slightly change their associated plane spacing. Therefore, the miniaturization of the crystalline domains is one of the reason could be considered to explain the broadening of the diffraction peaks. However, depending on TEM observations, there is a significant difference in the bubble density between sample r001c21 and r001b21, that if the diffraction peak broadening only related to the crystalline domain size, the breadth of peaks shall quite different between the r001c21 and r001b21 samples. Here we should note the fact that the helium bubbles are surrounded by strain fields under TEM observations, which indicates a high gas pressure inside the helium bubbles. And even if the burnup of sample r001b21 are more than twice as high as that of the sample r001c21, the size of helium bubbles is almost the same, the burnup difference only reflected in the bubble density. Based on this fact, Simeone et al.[3] assumed that the helium bubbles had achieved a characteristic size, and hence the bubble-induced strain had reached its limit in the samples with burnups above 40×10^{20} captures/cm^3. Therefore, the helium-bubble-caused strain is one of the main factors of the peak broadening, as the diffraction peak breadth of sample r001c21

and r001b21 are so similar. Finally, beside the bubble-induced strains, the incompleteness of crystal due to the irradiation damage, mainly the high concentration of point defects, is considered as another important cause of the peak broadening. Due to a previous TEM study showed the bubble-induced strains would not be eliminated by annealing until 1450°C[4], Suzuki et al.[2] showed the release of helium gas from the neutron irradiation B_4C dramatically increased around 900°C, we conjecture that the recovery in peak breadth we observed is originated by the thermally activated migration process of the helium interstitial atoms.

3.4 Summary

The neutron-irradiated B_4C samples with burnups of approximately 30×10^{20} captures/cm^3 and 80×10^{20} captures/cm^3, respectively, were studied by XRD. Isotropic changes in the lattices parameters which expanded in *a*-axis and shrank in *c*-axis were confirmed in our measurement. The changes in lattice parameters could be numerically all recovered by a post-irradiation annealing at 1000°C. However, the line broadening in the diffraction peaks originated by the helium-bubble-induced lattice strain and the point defects, only showed a small recovery after annealed at 1000°C. The small recovery in peak breadth were considered because of the thermally activated migration of the interstitial helium atoms which reduced the lattice distortion.

References

1. Rachinger WA. A Correction for the α1 α2 Doublet in the Measurement of Widths of X-ray Diffraction Lines. J Sci Instrum. 1948;25:254.

2. Suzuki H, Maruyama T, Wakasa T. Postirradiation Annealing of Boron Carbide Pellet Irradiated in Fast Breeder Reactor. J Nucl Sci Technol. 1979;16:588-95.

3. Simeone D, Gosset D, Quirion D, Deschanels X. Study of B_4C microstructure evolution under neutron irradiation by X-ray diffraction profiles analysis. J Nucl Mater. 1999;264:295-308.

4. Copeland GL, Donnelly RG, Martin WR. Irradiation Behavior of Boron Carbide. Nucl Technol. 1972;16:226-37.

Table 3.1 Lattice parameters of neutron irradiated B_4C

Specimen	Burnup ($\times 10^{20}$capture /cm^3)	Lattice parameters					
		a (Å)	Δa (%)	c (Å)	Δc (%)	V (Å^3)	ΔV (%)
unirradiated	–	5.598	–	12.07	–	327.56	–
r001c21	30	5.614	0.29%	11.93	-1.16%	325.51	-0.63%
r001b21	80	5.608	0.18%	11.99	-0.66%	326.60	-0.29%

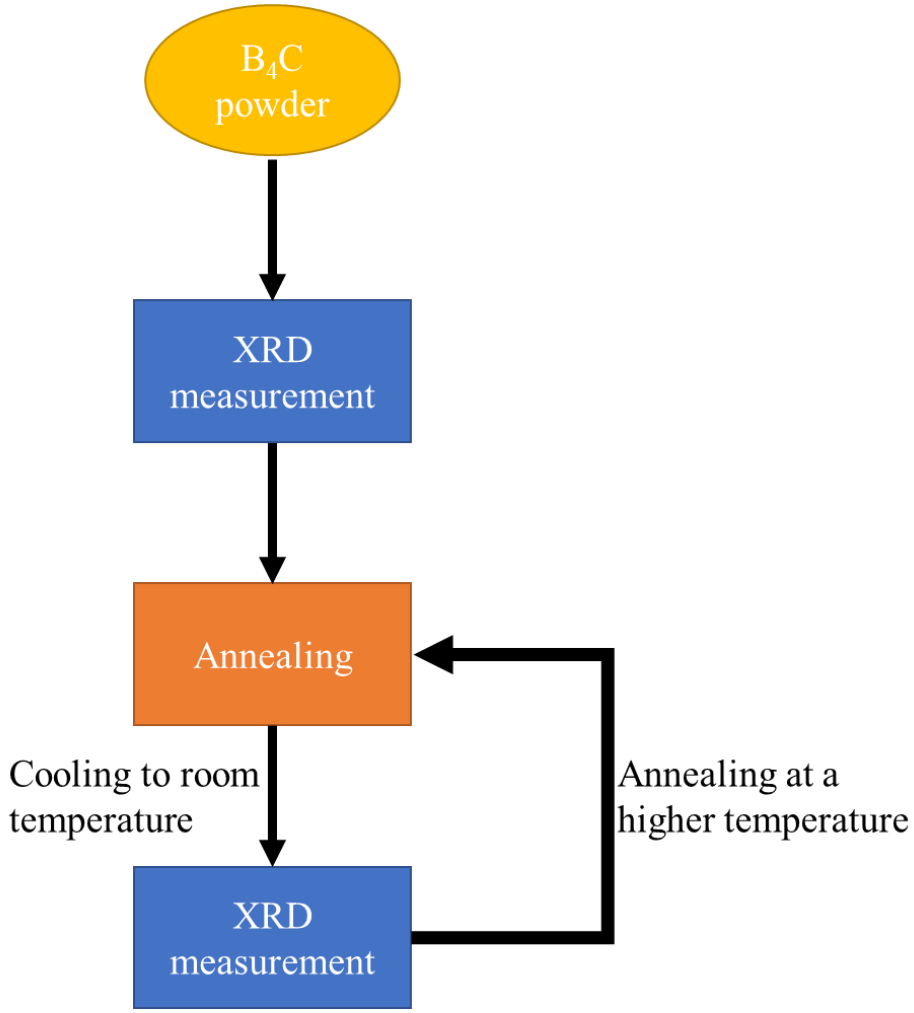

Figure 3.1 A flow diagram of the post-irradiation annealing experiment

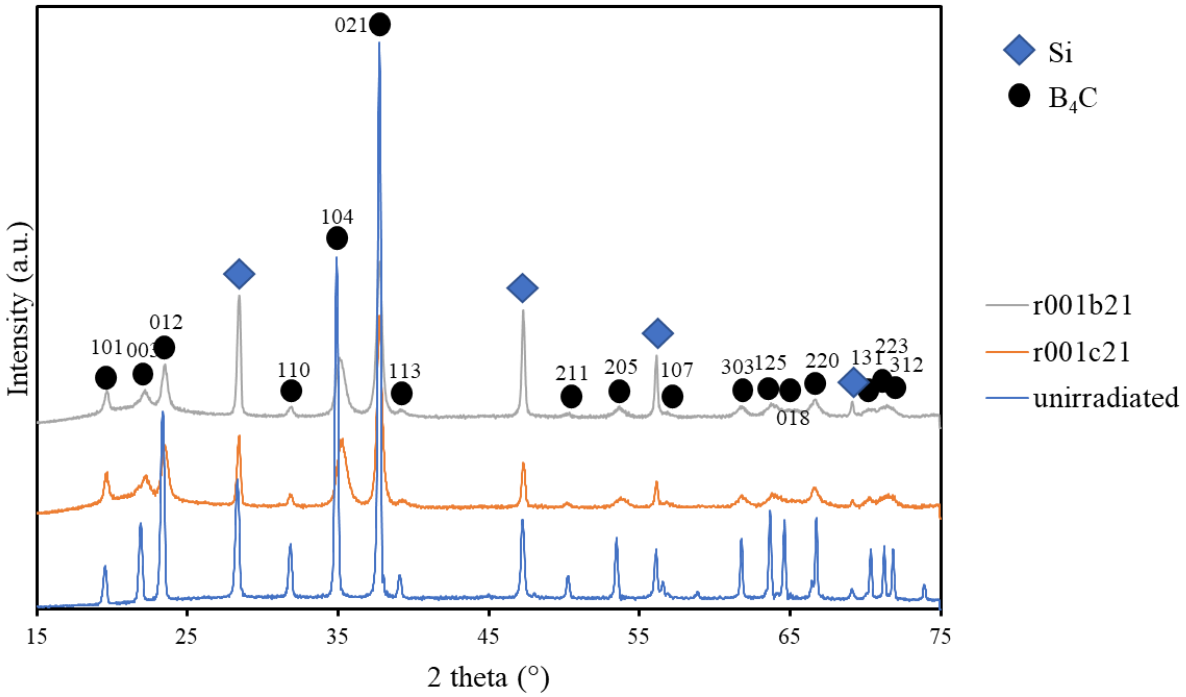

Figure 3.2 A comparison of the XRD patterns of the unirradiated sample and the neutron irradiated sample r001b21, r001c21.

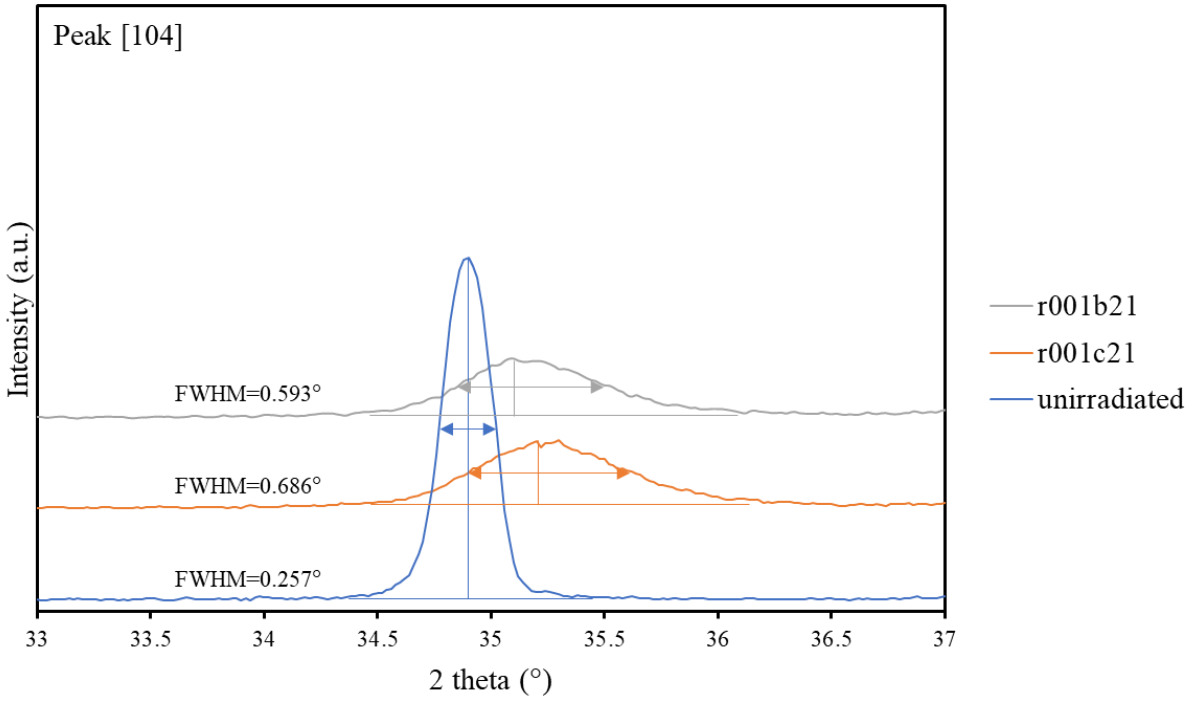

Figure 3.3 Evolution of the breadth of peak [104] in neutron irradiated B_4C specimen. The full width at half maximum (FWHM) are shown beside the peaks.

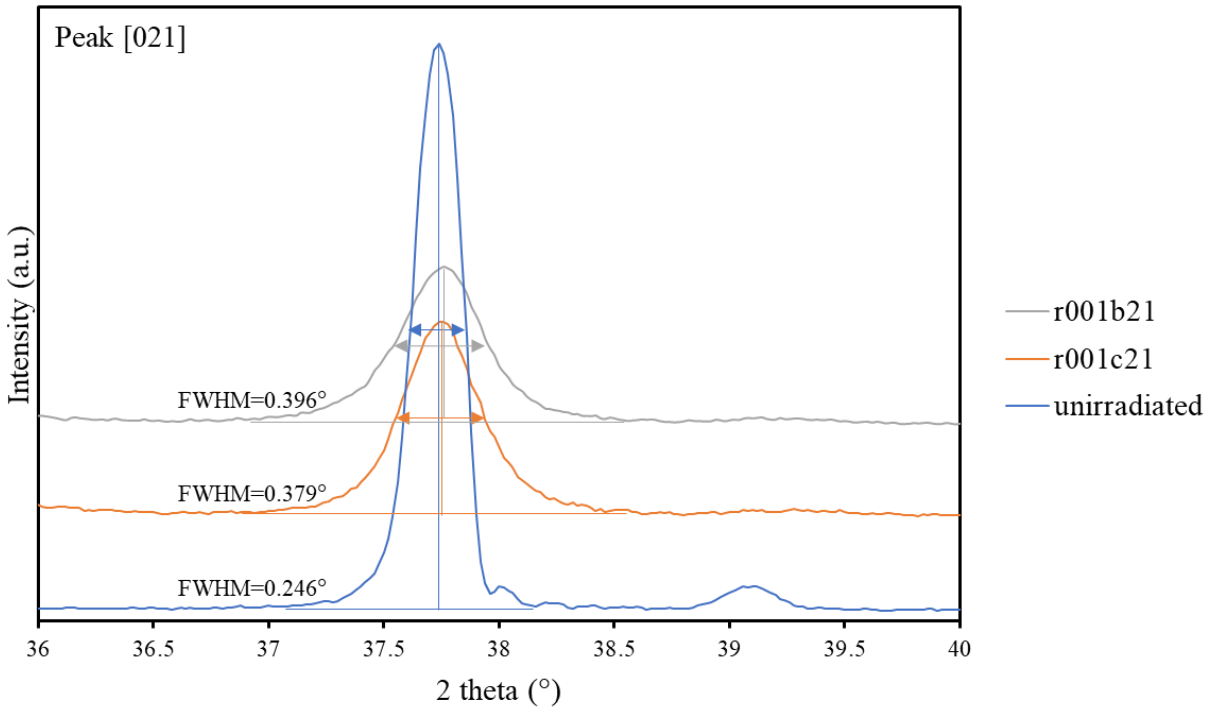

Figure 3.4 Evolution of the breadth of peak [201] in neutron irradiated B_4C specimen. The full width at half maximum (FWHM) are shown beside the peaks.

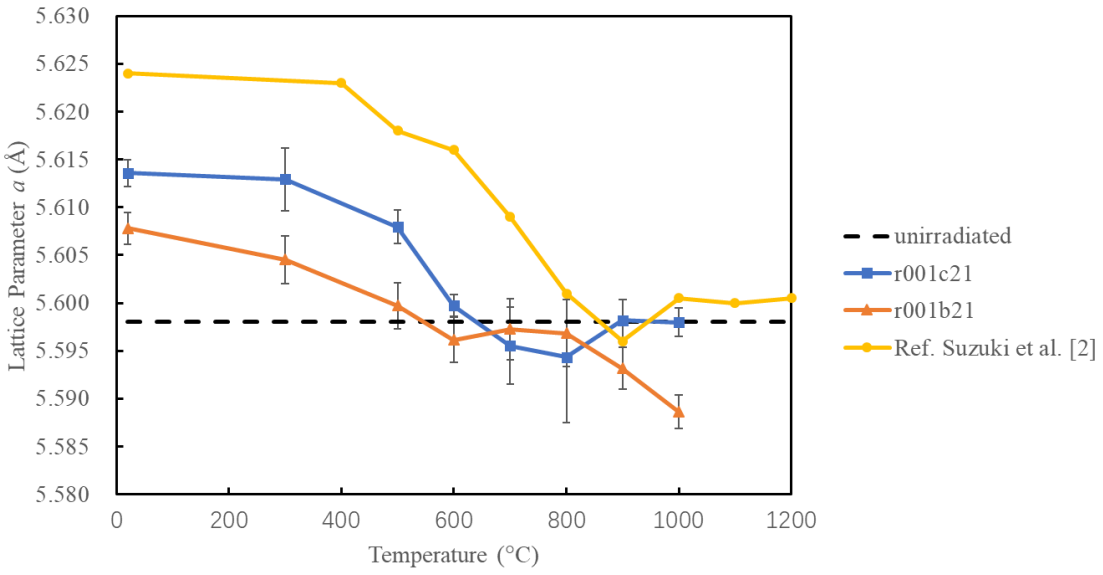

Figure 3.5 Recovery in lattice parameter *a* as a function of temperature.

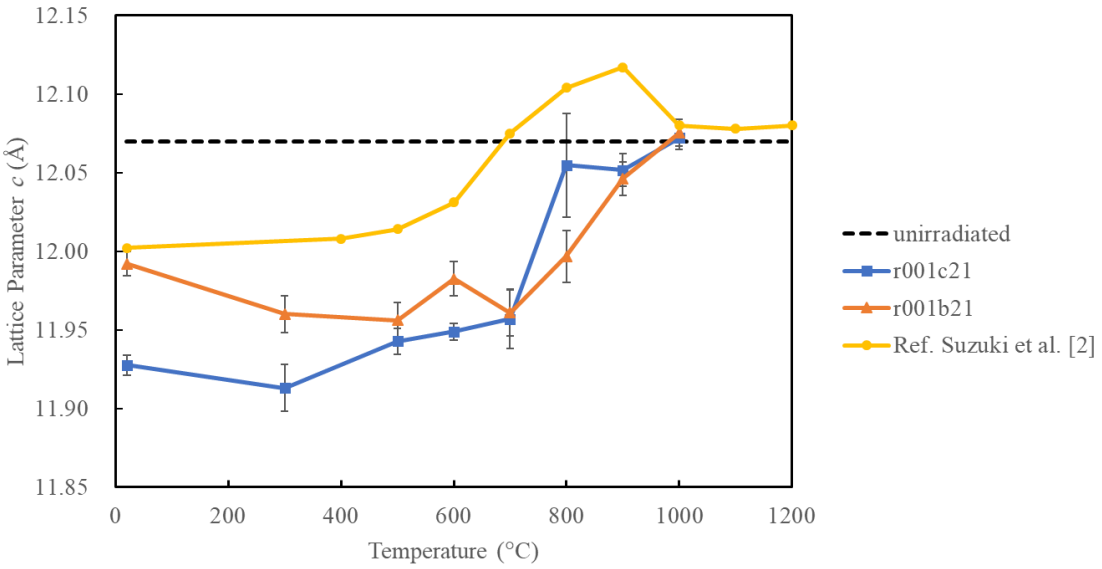

Figure 3.6 Recovery in lattice parameter *c* as a function of temperature.

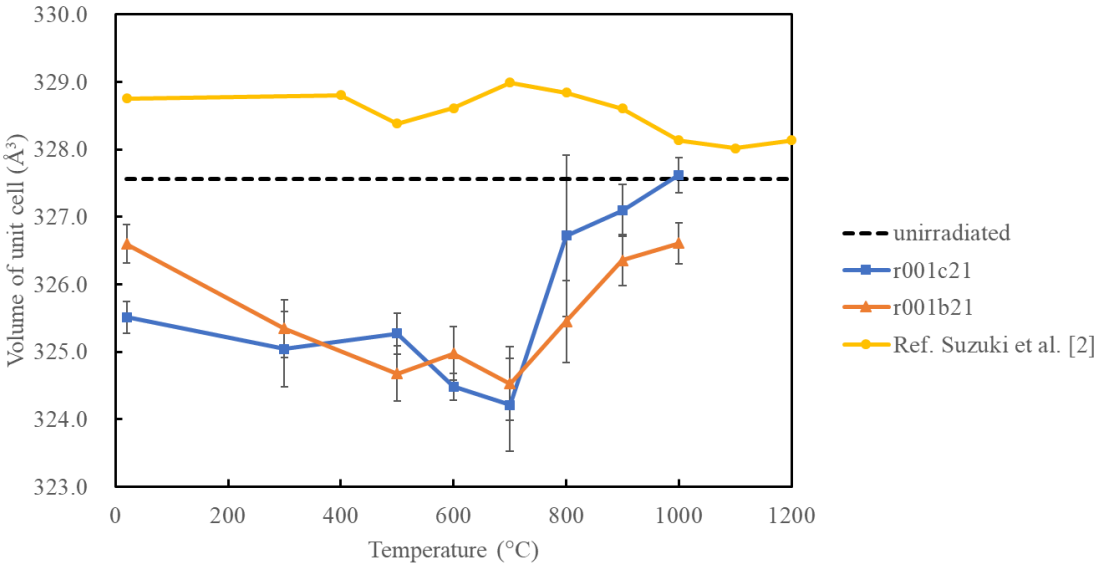

Figure 3.7 Recovery in cell volume V as a function of temperature.

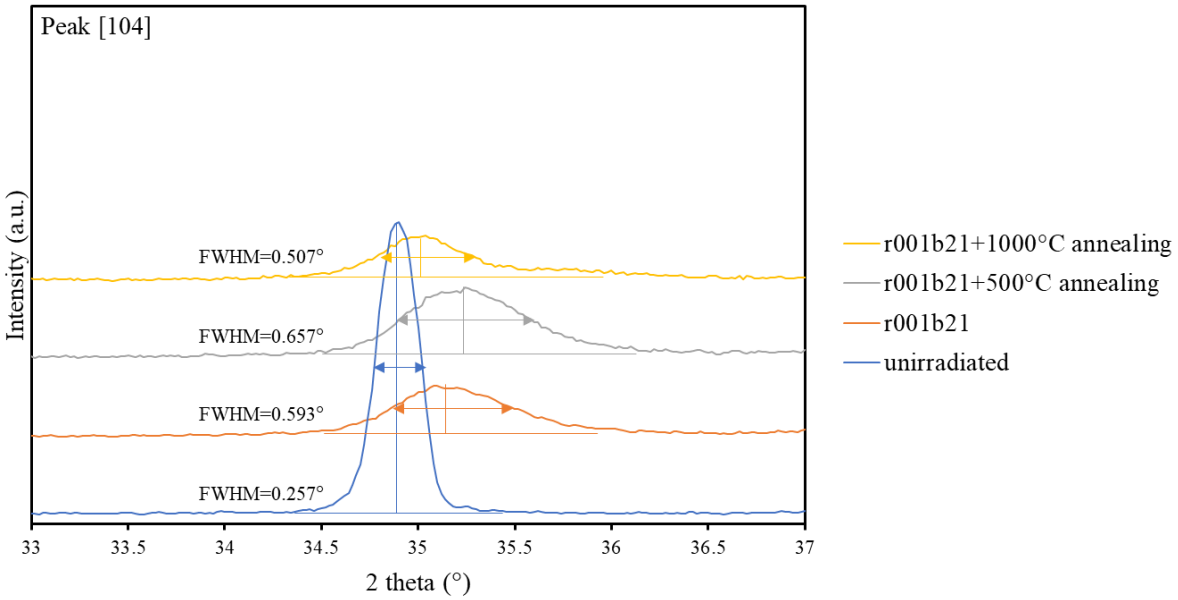

Figure 3.8 Evolution of the breadth of peak [104] after annealing

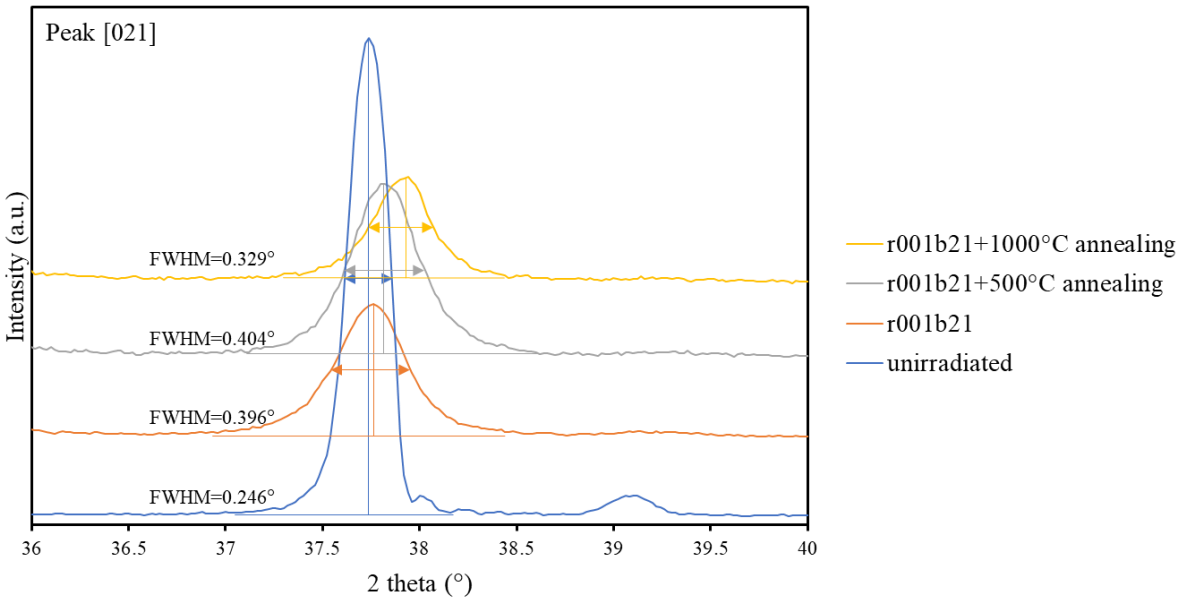

Figure 3.9 Evolution of the breadth of peak [021] after annealing

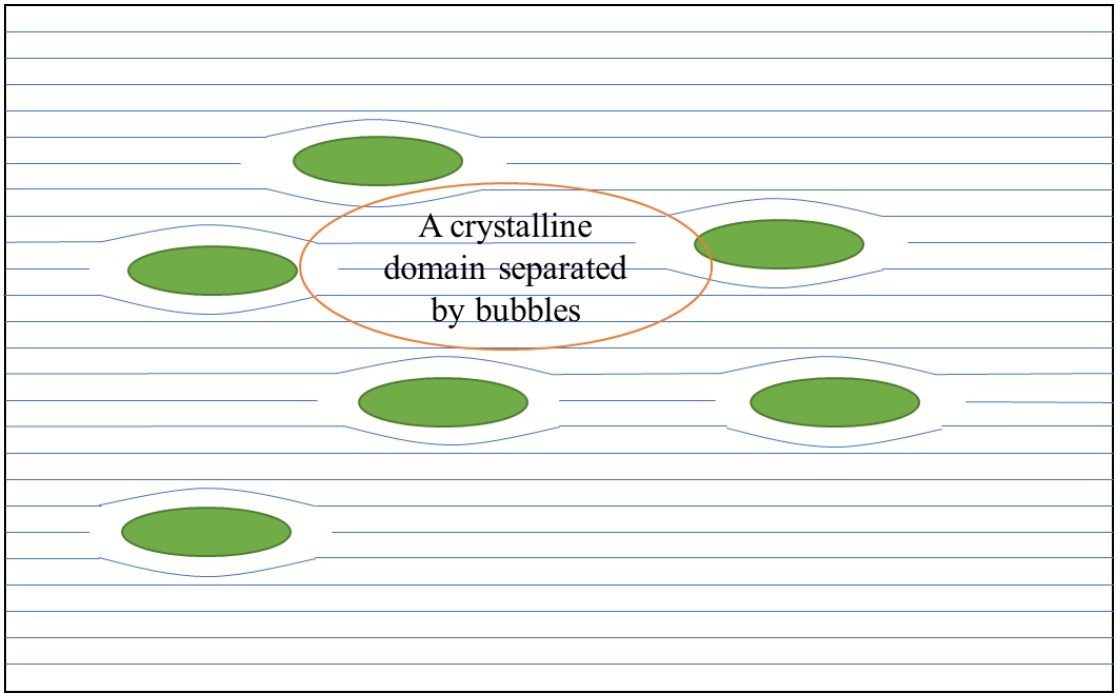

Figure 3.10 A schematic diagram for the miniaturization process of the crystalline domains induced by helium bubbles.

CHAPTER 4
TEM observation of the neutron-irradiated B_4C samples

4.1 Introduction

Under the neutron radiation of the reactor core, a large number of point defects were produced by neutron collisions and the neutron-induced $^{10}B(n, \alpha)^7Li$ reactions in the B_4C absorber pellets. Furthermore, the point defects could be considered as zero-dimensional (0D) defects which have very small influence regions, however, the high concentration of point defects could associate to form larger defect complexes/clusters and brought a major impact on the macro properties of the B_4C material. In the XRD based investigations of the previous chapter, we already know that the anisotropic changes in the lattice parameter have indicated the neutron-induced defects have a preference for specific crystalline directions in the B_4C crystals; and the recovery behaviors showed the migration of point defects become active in the temperature above approx. 800°C.

Transmission electron microscopy (TEM) is a powerful tool to investigate the materials' structure, defects, and crystallinity. As already described in chapter 1, many researchers have studied various boron carbide materials irradiated under various conditions with TEM[1–10]. However, the previous studies reported the occurrence of a variety of helium bubble morphology in the B_4C samples irradiated in different reactors. Even in the B_4C samples irradiated at the similar condition, different shapes of helium bubbles have been reported (e. g. Jostsons et al.[6] reported large disk-like bubbles parallel to (111) plane were formed in the B_4C sample irradiated at a temperature of 800–840°C. While Hollenberg et al.[8] showed the large disk-like bubbles were not fully developed in the B_4C sample irradiated at a higher temperature

of 900°C). Moreover, there is a disagreement in the orientation of the disk-like bubbles in B_4C. Ashbee et al.[2] reported the helium bubbles parallel to the {110} planes, Jostson et al.[5] and Copeland et al.[9] reported the helium bubbles most frequently parallel to the trace of the (111) plane and less frequently parallel to {100} and {110} traces.

In view of the different results in the past studies mainly based on the materials irradiated at constant temperature and flux, and it is still not clear how the helium bubbles are formed under different conditions, it is essential to clarify the exact state of the helium bubbles in B_4C irradiated in the actual control rods of fast reactors. Furthermore, there is no report on the evidence of lithium which is concurrently created the same amount as that of the helium atoms by the nuclear reaction mentioned above.

This chapter describes the TEM observation results of the B_4C specimens obtained from different parts of an actual control rod of the experimental fast reactor "JOYO." Heat treatment up to a temperature of 1040°C has been carried out at inside TEM using a high-temperature specimen holder to investigate the effect of temperature on the behaviors of helium and lithium in B_4C polycrystals.

4.2 Experimental details

The specimen observed with TEM were taken from the different positions of a retired control rod of the sodium-cooled JOYO fast reactor, which were labeled as r001_33, r001c21, and r001b21, in an order of from top to bottom; and the B_4C pellet irradiated in an irradiation rig of JOYO, labeled as K711b41. Due to the control rods of JOYO were inserted from the top of the reactor; therefore, the r001b21 specimen from the bottom part stayed near the reactor core for the longest time and was subjected to the largest fluence of neutron irradiation. The details of the neutron-irradiated B_4C samples were described in chapter 2. It must be pointed out that the K711b41 specimen was irradiated at a constant condition (neutron flux, temperature, etc.), while the irradiation conditions of the specimens from an actual control rod were variable due to the

movement of the control rod.

The K711b41 specimen for TEM was prepared using a focused-ion-beam-type micro-fabrication equipment (FIB) using accelerating Ga^+ ion beam (Seiko Instruments/SMI9800, Japan). **Figure 4.1** (A) is the scanning ion microscope (SIM) image of the specimen after sample preparation using the FIB. The grain boundaries were clearly visible. TEM observation was carried out with a JEM-2010F FE-TEM at 200 kV electron acceleration (JEOL, Japan). The other specimens were prepared by the ion-milling method using ~3 kV argon beam (Ion Tech, England). The observations were carried out with an H-9000 TEM operated with 300 kV beam-acceleration (Hitachi, Japan).

In order to study the temperature effects on the helium microstructure, some thin foils of specimens were heated up to a maximum temperature of about 1040°C and kept for 10–15 min on a single-tilt heating holder (GATAN, Model 628, USA). The heating and cooling rates were about 100°C/min. During heating, it was generally difficult to obtain fine micrographs due to specimen drift. Therefore, the microstructure was observed just after cooling to room temperature, except for mentioned cases.

To examine the phase change of the irradiated B_4C, the r001c21 specimen was crashed into powder and put in a Pt pan, followed by heat-treatment at 600–800°C for 1 h in Ar atmosphere. The heat-treated powder was identified using powder X-ray diffraction (XRD) technique on a PW-1710 diffractometer (Philips. Netherland), with CuKα radiation.

4.3 Results

In the K711b41 specimen irradiated at 800°C up to a burnup of 30.1×10^{20}cap/cm^3, the intragranular bubbles generally appeared in a flat-plate-like shape. When the specimen was adjusted to the proper angle that the bubbles were positioned parallel to the electron beam, many light-colored parallel straight lines were observed inside the B_4C grains, as shown in **Figure 4.1** (B). The typical lengths of these lines were in the range 10–50

nm, with most being approximately 30 nm in length. As shown in **Figure 4.1** (C), when the sample was tilted, the fine lines gradually became oval-shaped with reduced contrast, which revealed the flat lenticular shape of the intragranular helium bubbles. The intragranular bubbles in any grain of K711b41 were proved to be parallel to the rhombohedral (111) planes of B_4C by the selected area electron diffraction patterns.

Figure 4.2 shows the transmission electron micrographs of the low-burnup specimen r001_33 from the control rod. Only a small amount of helium was produced; therefore, it was assumed that helium almost completely dissolved in the B_4C lattice. Figure 4.2 (A) indicates the presence of parallel twin boundaries (stacking fault) that are frequently observed in as-received B_4C crystals, as reported by Ashbee [1] and Chen et al.[11]. It is very difficult to determine the neutron-irradiation-induced helium bubbles in the grains. Only the strain fields along the grain boundaries indicating a gathering of helium gas, as shown in Figure 4.2 (B). After the heat treatment up to 1040°C for 15 min, as shown in Figure 4.2 (C) the invisible irradiation defects became visible by forming defect clusters (appearing as black dots). Figure 4.2 (C) is the same area as (A) after heating. Figure 4.2 (D) is taken from another grain after the heat treatment. Small helium bubbles nucleated and appeared along with the strain fields in this specimen after the heat treatment.

In the r001c21 specimen, very small helium bubbles in the order of a few nanometers in diameter could be found. The bubbles looked approximately spherical in shape and heterogeneously nucleated, as shown in **Figure 4.3** (A). They had a tendency to connect to form wavy strings approximately parallel to the (111) plane. Near the grain boundaries, there is a significant reduction in bubble density; the so-called denuded or depleted zone (Figure 4.3 (B)) as previously mentioned in many reports[3–6, 9]. The formation of this zone is attributed to the strong defect-trapping effect of grain boundaries (i.e. sink). In contrast, the thickness of the grain boundary extended and the inner side of the grain boundary looked low density.

In the high-burnup specimen r001b21, there is no obvious difference in the size of the small helium bubbles when compared to the r001c21 specimen, as shown in

Figure 4.4(A) and (B). However, because more helium was produced, the bubbles had a very high density in each grain. The grain boundary bubbles are bigger and the grain boundary is thicker than in Figure 4.3, as shown in Figure 4.4(B).

As can be seen in **Figure 4.5** (A), a grid-like contrast is observed in the r001_33 specimen. The crystallographic orientation was examined using a selected area diffraction pattern, which showed that stacking faults lie on the rhombohedral {100} planes. As shown in Figure 4.5 (B), parallel to the trace of {100} planes, straight bubbles or cracks of lengths more than 200 nm are rarely observed in the as-received r001c21 specimen. As shown in Figure 4.5 (C), thick and large bubbles formed along the {100} planes in the r001b21 specimen after heat-treatment up to 1040°C for approximately 10 min.

When the r001b21 specimen was heated to over 800°C, a large number of liquid droplets suddenly appeared and quickly evaporated during TEM observation. **Figure 4.6** (A) shows a micrograph of the r001b21 specimen during heating near 800°C obtained using TEM. Hemisphere-shaped residues are visible on the specimen surface. Figure 4.6 (B) was taken at room temperature after heating up to 1040°C; black traces remain after evaporation of the liquid drops. The formation of hemispherical drops on the surface of foils was observed for all irradiated B_4C specimens, but more obviously for high burnup specimens. Because it may contaminate the inside of the TEM device, the in-situ heating of the high burnup B_4C specimens should be avoided, as they contain a large amount of lithium.

Figure 4.7 shows the XRD patterns of the r001b21 specimen after 2-time heat-treatment at 700 and 800°C in an Ar atmosphere for 1 h, respectively. In the XRD pattern for the 800°C-annealed specimen, $LiBO_2$ and $Li_2B_4O_7$ are identified along with the B_4C main phase. The peak heights of these compounds are slightly smaller for the specimen annealed at 700°C for 1 h. However, after the first-time heat-treatment both at 800 or 700°C, the peaks of $LiBO_2$ and $Li_2B_4O_7$ were not detected by XRD.

4.4 Discussion

Our TEM observations of the constant-temperature-irradiated specimen K711b41 showed that all the plate-shaped helium bubbles lie parallel to the (111) plane, which is in good agreement with previous reports for B_4C specimens irradiated at temperatures lower than ~1000°C, presented by Jostsons et al.[6], Ashbee[1], and Stoto et al.[4]. As Stoto et al.[4] have already indicated, as several cuts in the reciprocal lattice of B_4C are quite similar to each other, it is confusing to index the (110) and (111) plane, which might lead to some incorrect results for the orientation of helium bubbles in the B_4C crystal. When the specimen K711b41 was capsule-irradiated in JOYO at a constant temperature of 800°C, helium bubbles grew to a relatively large plate shape (10–50 nm in diameter). It has been reported that helium bubbles are usually accompanied by strain fields[2, 4–6] . However, this phenomenon is not clearly observed for the K711b41 specimen in this study. It is reasonable to assume that this is because only this specimen was prepared by FIB technique, and a high-energy Ga^+ beam used to fabricate thin films induces a local temperature rise of more than 1000°C, same as for low thermal conductivity insulators such as SiO_2[12]. After neutron irradiation, the thermal conductivity of ceramics generally decreases significantly due to the formation of crystalline defects[13–16]. Because the local temperature rose during FIB fabrication, the local strain was mitigated in the K711b41 thin film. It has been reported that strain fields accompanying the bubbles disappeared after post-irradiation high-temperature annealing at temperatures above 1400°C[2–6].

However, in the specimen irradiated in the actual control rod environment of JOYO which has a lower irradiation temperature than K711b41, the bubble size was much smaller (a few nanometers in diameter), and was mostly spherical rather than in a larger plate shape. The helium bubbles observed in the r001c21 and r001b21 specimens are tiny and spherical, with a tendency to align into wavy lines approximately parallel to the (111) plane; however, their sizes do not differ much. It is reasonable to infer that the effect of the ^{10}B burnup mainly determines the bubble

density. When comparing the K711b41 and r001b21 specimens, the shape of helium bubbles in the former (large plate-shaped) and latter (small spherical) is different, even though the ^{10}B burnup and maximum temperature are relatively similar. Jostson et al.[6] reported that small spherical bubbles were formed for the specimen irradiated at 550°C with 81% burnup (natural B_4C). However, for specimens irradiated at 700°C and above, a flat plate shape is developed. Copeland et al.[9] also indicated that black-spot defects occur for lower temperature (350–400°C) irradiated specimens. Therefore, temperature seems to be the major factor affecting the helium bubble shape. A clear difference in irradiation conditions is "steady state irradiation" for samples irradiated in materials testing rigs (such as K711b41 and Jostson's) and "cyclic or variable condition in actual control rod" for the present specimens (such as r001_33, r001c21, and r001b21). In the actual control rod, the highest temperature was achieved near 800°C, and the duration at that temperature was not so long; however, these conditions were experienced cyclically. This means that the generation of helium was cyclic, and there was not sufficient time for the helium to migrate and accumulate into large bubbles. However, there was a tendency to align with the (111) plane, the same plane as observed in the K711b41 specimen. In summary, in the actual control rod with a high burnup in the sodium-cooled fast reactor, small spherical bubbles are formed, and for high temperature steady state irradiation, lenticular or plate-shaped bubbles are produced. Bubble formation process should be dominated by the migration of helium atoms/vacancies in the crystal. Therefore, the large plate-shaped bubbles cannot be formed at low temperature where the helium/vacancy has poor mobility. Similarly, if the temperature is unstable, they also do not have enough time to form plate-shaped bubbles. The former aligns into a wavy plane and the latter forms onto a plane, both parallel to the (111) plane in the B_4C crystal.

The heterogeneous distribution of helium bubbles in the r001c21 specimen may be caused by the migration of vacancies containing helium atoms (V_{He}) onto weakly-bonded interstices. Initially helium atoms are randomly generated by the neutron absorption reaction; therefore, distribution of helium is also random. Once helium

bubbles are nucleated at proper sites such as the (111) planes, they grow by capturing free V_{He}. The difference in defect concentration generates the driving force for V_{He} migration. Hence, the bubbles can slowly grow. A study on helium gas release of neutron irradiated B_4C pellets conducted by Suzuki et. al.[17] determined that, the helium gas release rate is very low at temperatures lower than 700°C. It is assumed that the migration of V_{He} in B_4C at temperatures lower than 700°C is slow; therefore, V_{He} are trapped by nearby helium bubbles to generate arrays of tiny bubbles. If the material is kept for a relatively long time at temperatures higher than 700°C, these tiny bubbles will connect each other to make larger plate-shaped bubbles, as observed in the K711b41 specimen and other many reports[1–10, 18, 19].

Other than on the (111) plane, it is confirmed that big helium bubbles or cracks are also generated on the {100} planes in some grains, possibly because the trace of slip is a good sink for V_{He}. These helium bubbles can be easily distinguished from the bubbles along the (111) plane by their longer length. According to Reddy et al.[20] and Qi An and Goddard[21], slip in B_4C can be induced by shock loading or indentation on the {100} planes by debonding of C-B-C chains under shear stress, followed by formation of amorphous bands. Chen and McCauley[22] observed that mechanical scratching also induced amorphization of B_4C. Therefore, one of a possible explanation for the formation of long bubbles or cracks along the {100} planes is due to the amorphous bands caused by slip or mechanical scratches during powder preparation are good sinks for irradiation-induced defects, and also are suitable places for helium bubble growth.

It was very difficult to find the trace of the lithium generated with the helium in neutron irradiated B_4C, as it is generally invisible in TEM observation. The liquid phase that appeared during in-situ heating of the high burnup specimen at over 800°C (Figure 4.6) is suspected to be a consequence of the formation of lithium-bearing compounds on grain surfaces. From the XRD analysis shown in Figure 4.7, two kinds of lithium borates are detected. The melting points of $LiBO_2$ and $Li_2B_4O_7$ are 845°C and 917°C, respectively. Because the $Li_2B_4O_7$ have a higher melting point than that of $LiBO_2$ and

the former may only form under oxygen-rich condition, and the liquid phase was observed at around 800ºC, the observed material on the specimen surface is more likely to be $LiBO_2$. In considering the possible eutectic reaction of these two borates and the high vacuum inside TEM, the equilibrium melting points might be lower than the above value. The detection of Li-compounds in the heat-treated specimen is an evidence of the presence of Li on the surface of the specimens at that temperature. Considering the atomic size of lithium, a lot of it may remain in the interstitial sites of the B_4C lattice. It can migrate to the surface easily under high temperatures, and subsequently form low melting-point compounds. Oxygen may be supplied from the oxidized surface layer, which generally exists on the surface of non-oxide ceramics[23]. The reason why the borates detected only in the secondly heated specimens can be attributed for the high reactivity of metallic Li on the specimen surface. The specimen was kept in ambient atmosphere after the first heat-treatment, the lithium absorbs easily moisture from atmosphere to form lithium-H-O compounds. That compound will react with B_4C during the second heat-treatment. If the temperature increases further or the surface is bombarded by the electron beam during TEM observation, lithium compounds will be evaporated away in a high vacuum.

4.5 Conclusions

The shape of helium bubbles in B_4C, induced by fast neutron irradiation in an actual control rod of the fast reactor JOYO was observed using TEM. The helium bubbles are tiny and spherical with a diameter of a few nanometers; the bubbles are produced inside crystals in the as-received specimens. If the burnup increases, the size of the bubbles is not affected, but the density increases. These tiny bubbles form arrays approximately parallel to the rhombohedral (111) plane. In the specimen irradiated in the materials testing rig under a constant temperature of 800°C, the helium forms relatively large plate-shaped bubbles with a diameter of 10 to 50 nm, which lie parallel to the (111)

plane of B_4C. Other than the (111) plane, it is confirmed that large helium bubbles/cracks are sometimes generated on the {100} planes. It can be inferred that amorphous bands caused by slip or mechanical scratches during powder preparation are also good sinks for irradiation defects, and amorphous bands are a suitable place for helium bubble growth.

Finally, a liquid phase appeared during the in-situ heating of the specimens at temperatures over 800°C, which is believed to be caused by the melting of some lithium-bearing compounds. One of the possible candidates is $LiBO_2$, which has a lower melting point of 845°C. Considering the atomic size of lithium, it is possible that a lot of it may remain in the interstitial sites of the B_4C lattice, and that it can migrate easily to the specimen surface at high temperatures.

References

1. Ashbee KHG. Defects in Boron Carbide before and after Neutron Irradiation. Acta Metall. 1971;19:1079-&.

2. Ashbee KHG, Frank FC, Dubose CKH. Voids in Boron Carbide. J Nucl Mater. 1973;48:193-8.

3. Stoto T, Ardonceau J, Zuppiroli L, Castiglioni M, Weckermann B. Behavior of Implanted Helium in Boron-Carbide in the Temperature-Range 750-Degrees-C to 1720-Degrees-C. Radiat Eff Defect S. 1987;105:17-30.

4. Stoto T, Housseau N, Zuppiroli L, Kryger B. Swelling and Microcracking of Boron-Carbide Subjected to Fast-Neutron Irradiations. J Appl Phys. 1990;68:3198-206.

5. Jostsons A, Dubose CKH. Microstructure of Boron Carbide after Fast-Neutron Irradiation. J Nucl Mater. 1972;44:91-&.

6. Jostsons A, Dubose CKH, Copeland GL, Stiegler JO. Defect Structure of Neutron-Irradiated Boron-Carbide. J Nucl Mater. 1973;49:136-50.

7. Hollenberg GW, Cummings WV. Effect of Fast Neutron Irradiation on the Structure of Boron Carbide. J Am Ceram Soc. 1977;60:520-5.

8. Hollenberg GW, Mastel B, Basmajian JA. Effect of Irradiation Temperature on the Growth of Helium Bubbles in Boron-Carbide. J Am Ceram Soc. 1980;63:376-80.

9. Copeland GL, Donnelly RG, Martin WR. Irradiation Behavior of Boron Carbide. Nucl Technol. 1972;16:226-37.

10. Cummings WV, Laidler JJ, Mahagin DE, Mastel B. Microstructure of Fast-Reactor-Irradiated Boron Carbide. Trans Am Nucl Soc. 1972;15:742-+.

11. Chen M, McCauley JW, Hemker KJ. Shock-induced localized amorphization in boron carbide. Science. 2003;299:1563-6. Epub 2003/03/08.

12. Ishitani T, Kaga H. Calculation of Local Temperature Rise in Focused-Ion-Beam Sample Preparation. Journal of Electron Microscopy. 1995;44:331–6.

13. Yano T, Miyazaki H, Iseki T. Effect of isochronal annealing on thermal diffusivity of neutron-irradiated AIN. J Nucl Mater. 1996;230:74-7.

14. Akiyoshi M, Yano T, Tachi Y, Nakano H. Saturation in degradation of thermal diffusivity of neutron-irradiated ceramics at 3×1026n/m2. J Nucl Mater. 2007;367-370:1023-7.

15. Akiyoshi M, Tsuchida H, Takagi I, Yoshiie T, Qiu X, Sato K, Yano T. Irradiation effects on thermal diffusivity and positron annihilation lifetime in ceramics induced by neutron and 30 MeV electron. J Nucl Sci Technol. 2012;49:595-601.

16. Maruyama T, Onose S, Kaito T, Horiuchi H. Effect of fast neutron irradiation on the properties of boron carbide pellet. J Nucl Sci Technol. 1997;34:1006-14.

17. Suzuki H, Maruyama T, Wakasa T. Postirradiation Annealing of Boron Carbide Pellet Irradiated in Fast Breeder Reactor. J Nucl Sci Technol. 1979;16:588-95.

18. Soga T, Tobita K, Mitsugi T, Miyakawa S. The Development of a Sodium Bonded Type Control Rod in Joyo. Japan Nuclear Cycle Development Institution, 2000. (no. 1344-4239).

19. Basmajian JA, Pitner AL, Mahagin DE, Ripfel HCF, Baker DE. Irradiation Effects in Boron Carbide Pellets Irradiated in Fast Neutron Spectra. Nucl Technol. 1972;16:238-48.

20. Reddy KM, Liu P, Hirata A, Fujita T, Chen MW. Atomic structure of amorphous shear bands in boron carbide. Nat Commun. 2013;4:2483. Epub 2013/09/21.

21. An Q, Goddard WA, 3rd. Atomistic Origin of Brittle Failure of Boron Carbide from Large-Scale Reactive Dynamics Simulations: Suggestions toward Improved Ductility. Phys Rev Lett. 2015;115:105501. Epub 2015/09/19.

22. Chen MW, McCauley JW. Mechanical scratching induced phase transitions and reactions of boron carbide. J Appl Phys. 2006;100.

23. Park D-C, Yano T, Iseki T, Urabe K. Effect of Nitrate Salts as Sintering Additives during the Ball-Milling Process of Silicon Nitride Powders. J Am Ceram Soc. 2000;83:2967-73.

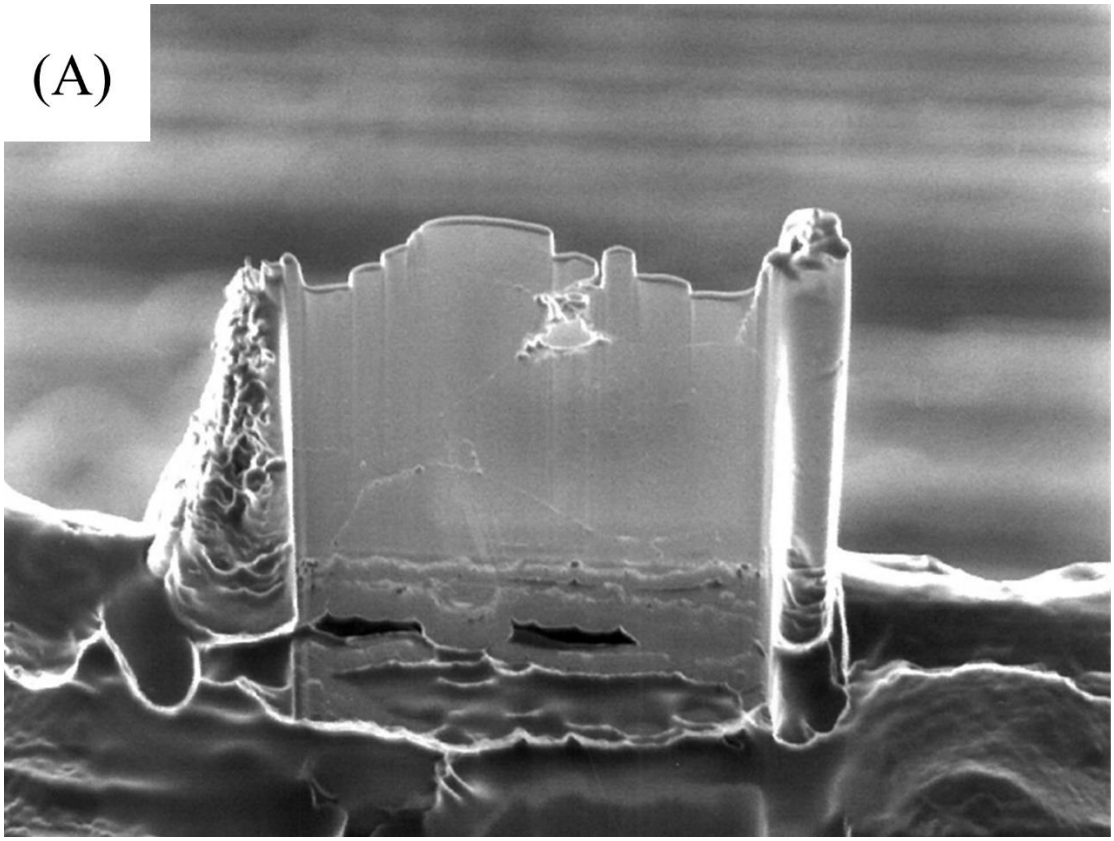

Figure 4.1 (A) SIM micrograph of the K711b41 specimen after thin foil preparation using FIB. (B) TEM micrograph of the as-received K711b41 specimen. (C) The same area with (B) but tilted 25°. The crowded dark spots were considered as the damages of FIB process.

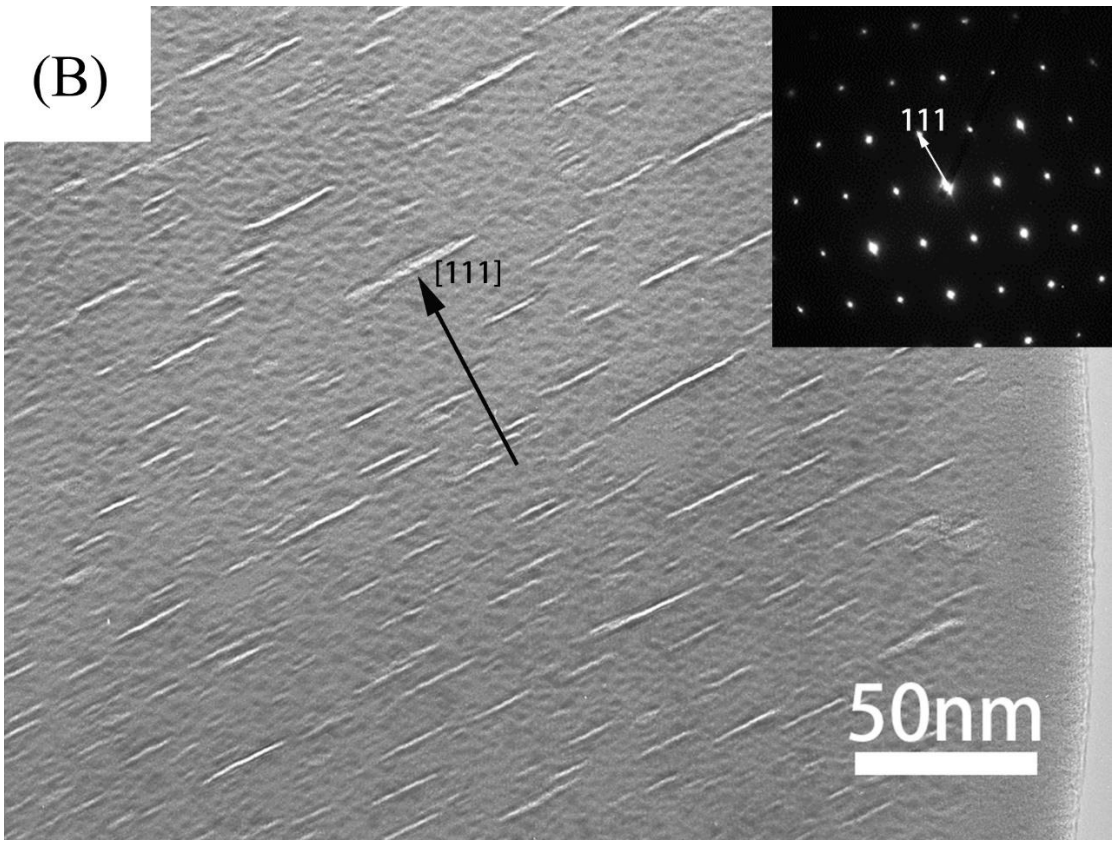

Figure 4.1 (B)

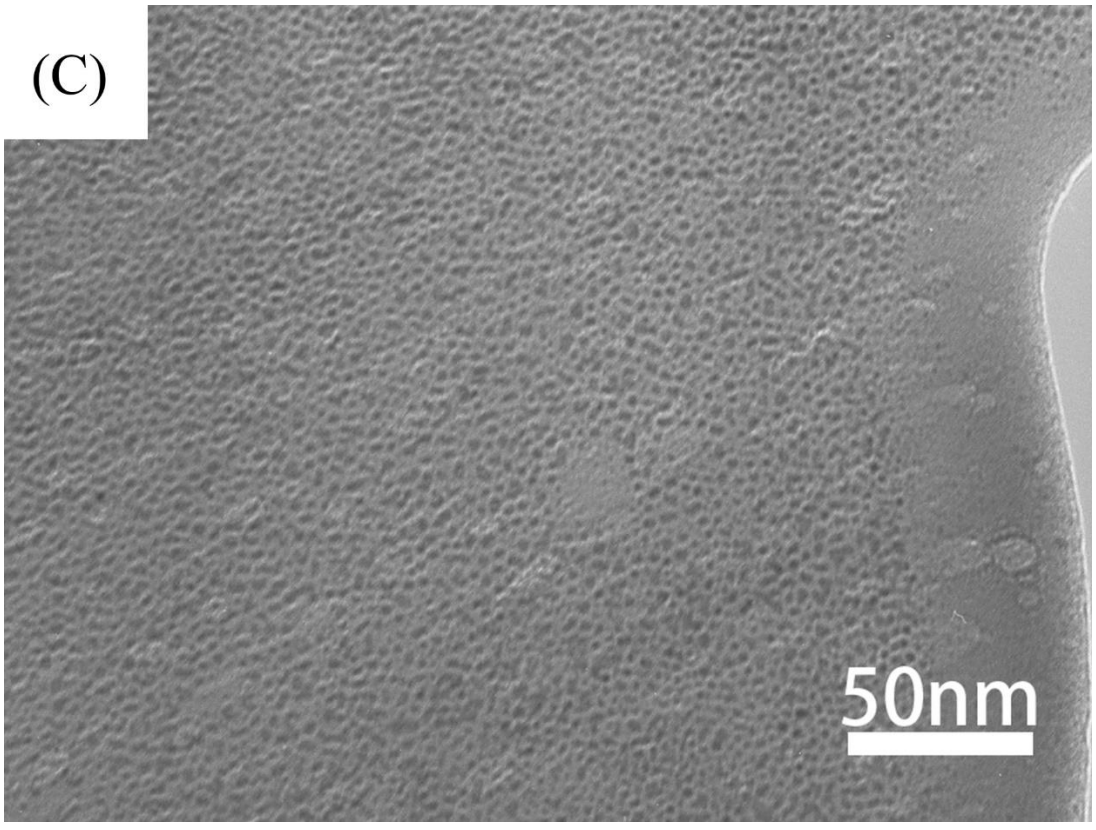

Figure 4.1 (C)

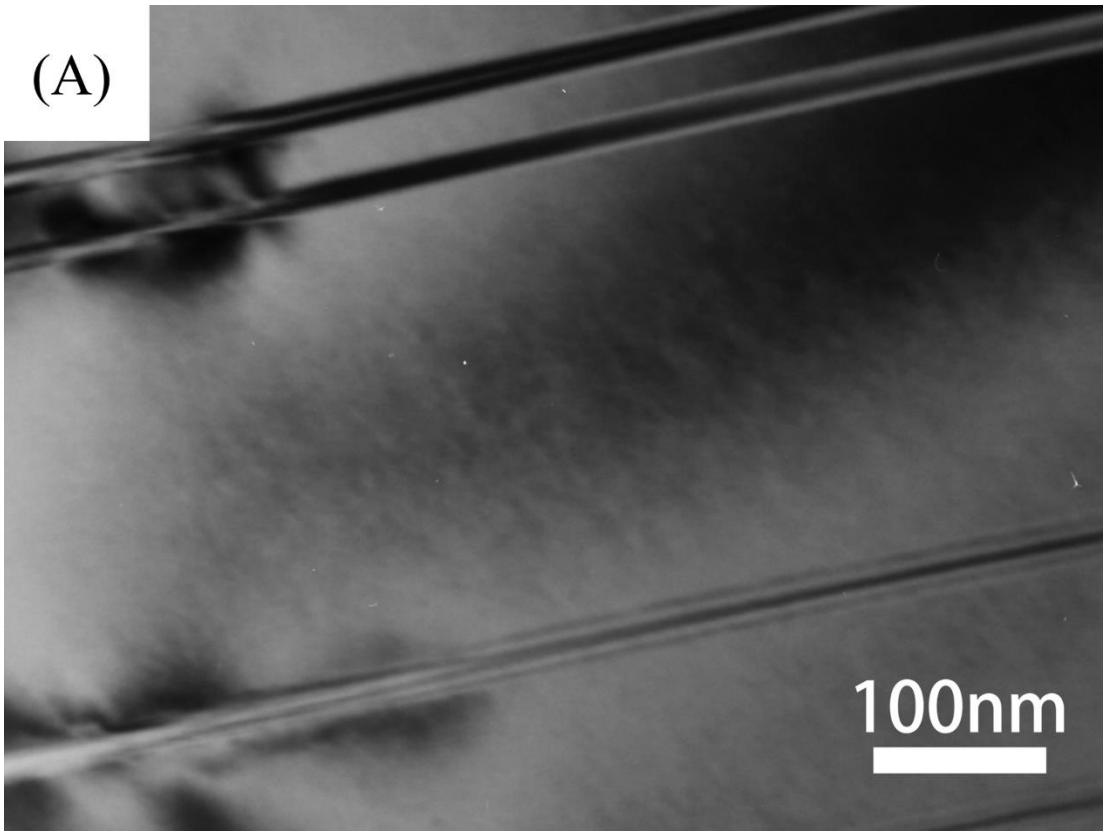

Figure 4.2 TEM micrographs of r001_33 specimen. (A) and (B) As-received specimen. (C) The same area with (A) after 1040°C heat-treatment and observed at room temperature. (D) Another grain after heat-treatment and observed at room temperature.

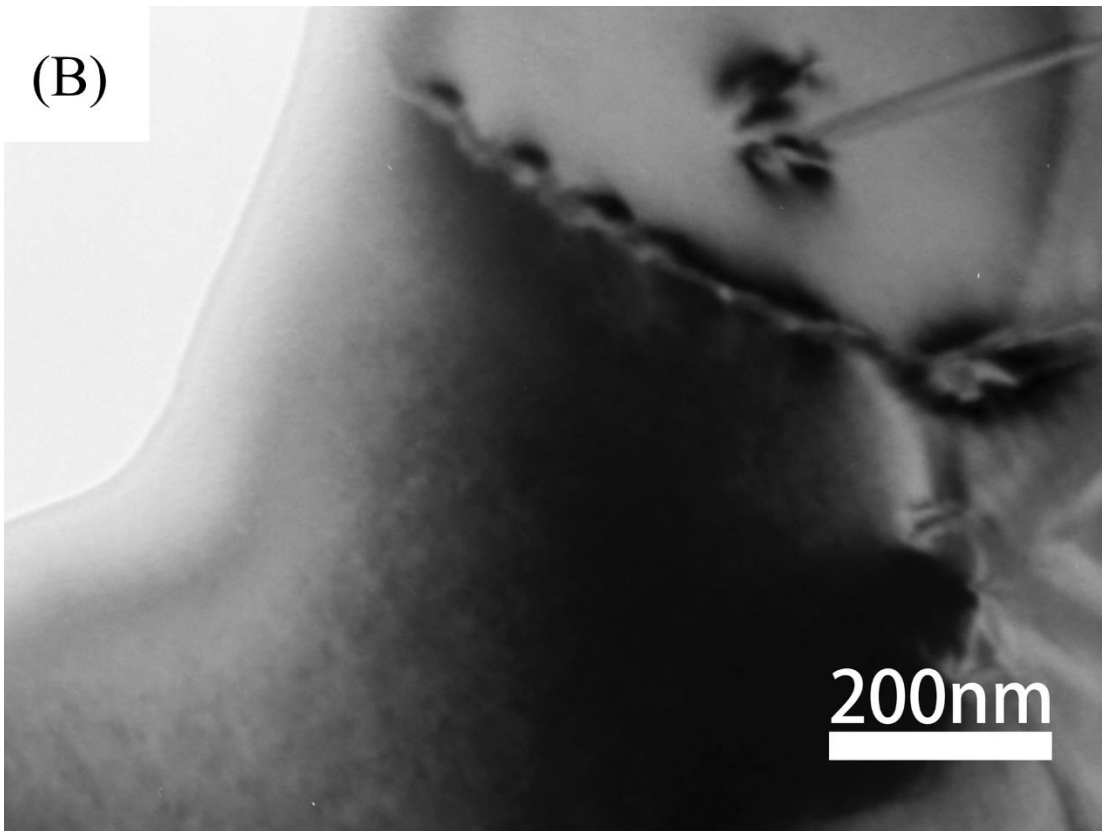

Figure 4.2 (B)

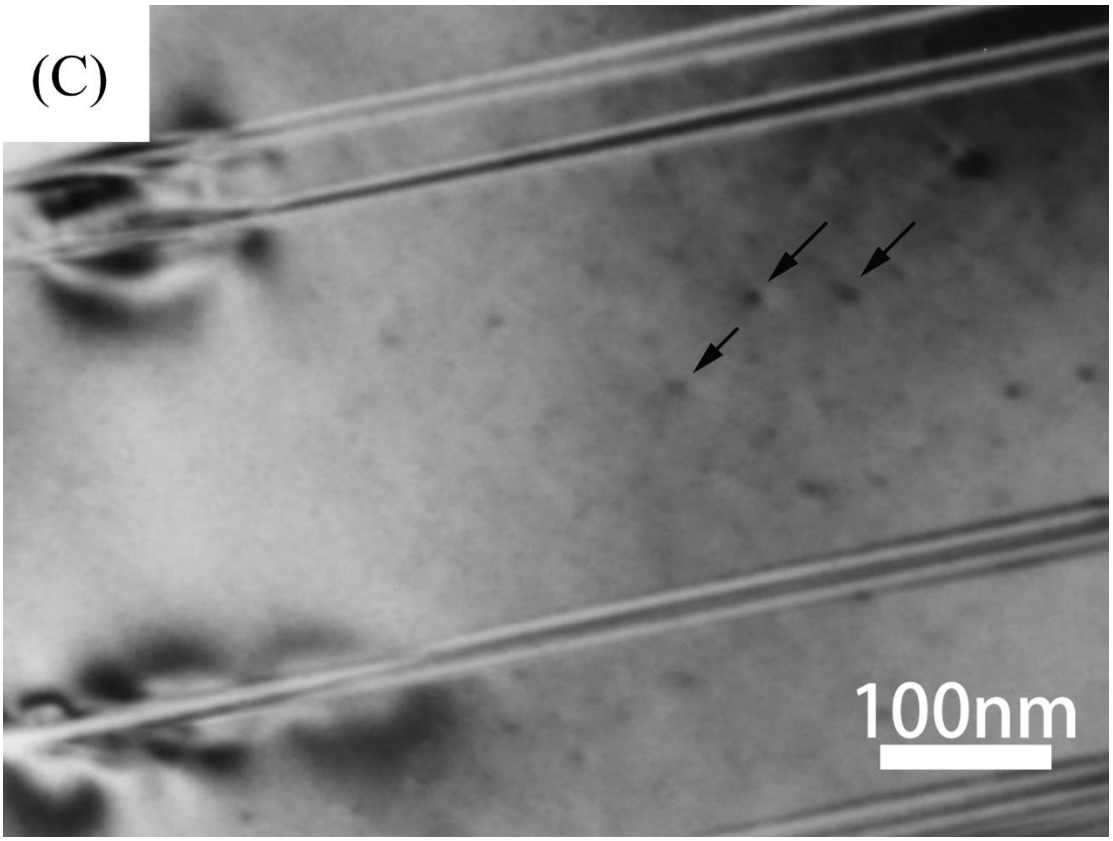

Figure 4.2 (C)

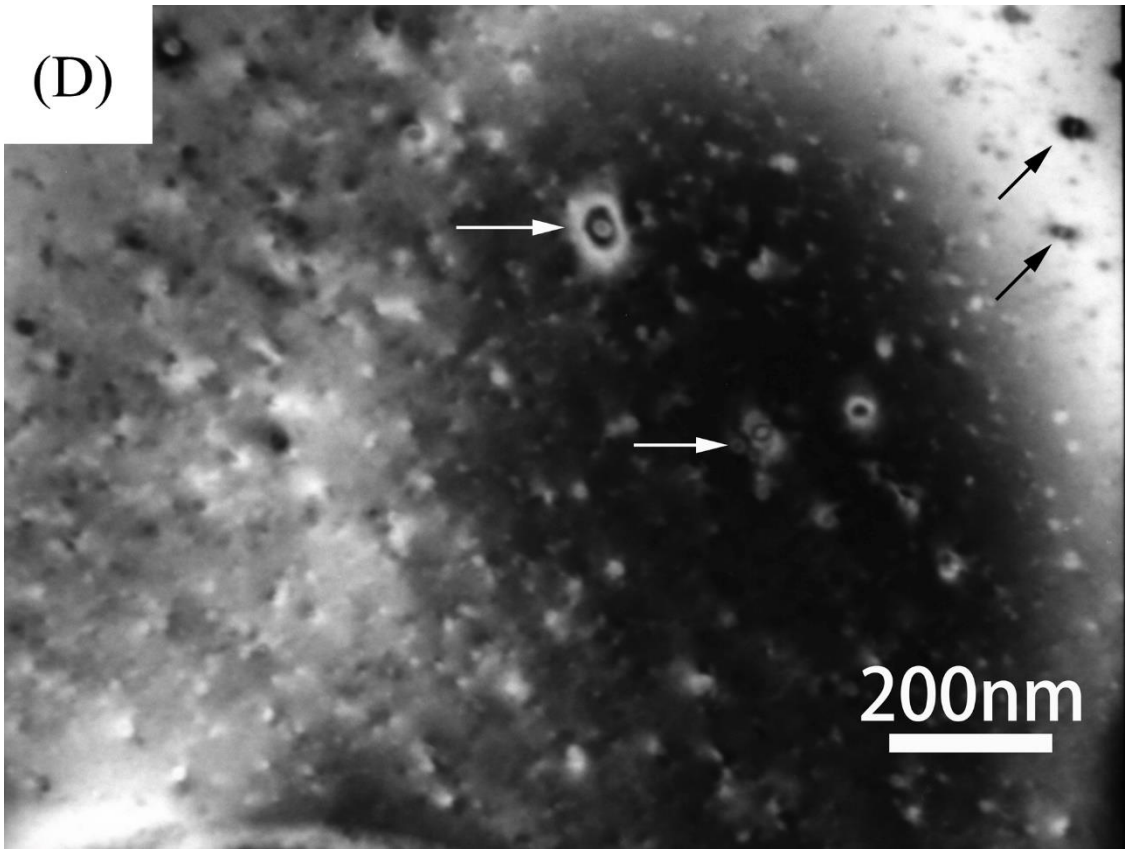

Figure 4.2 (D)

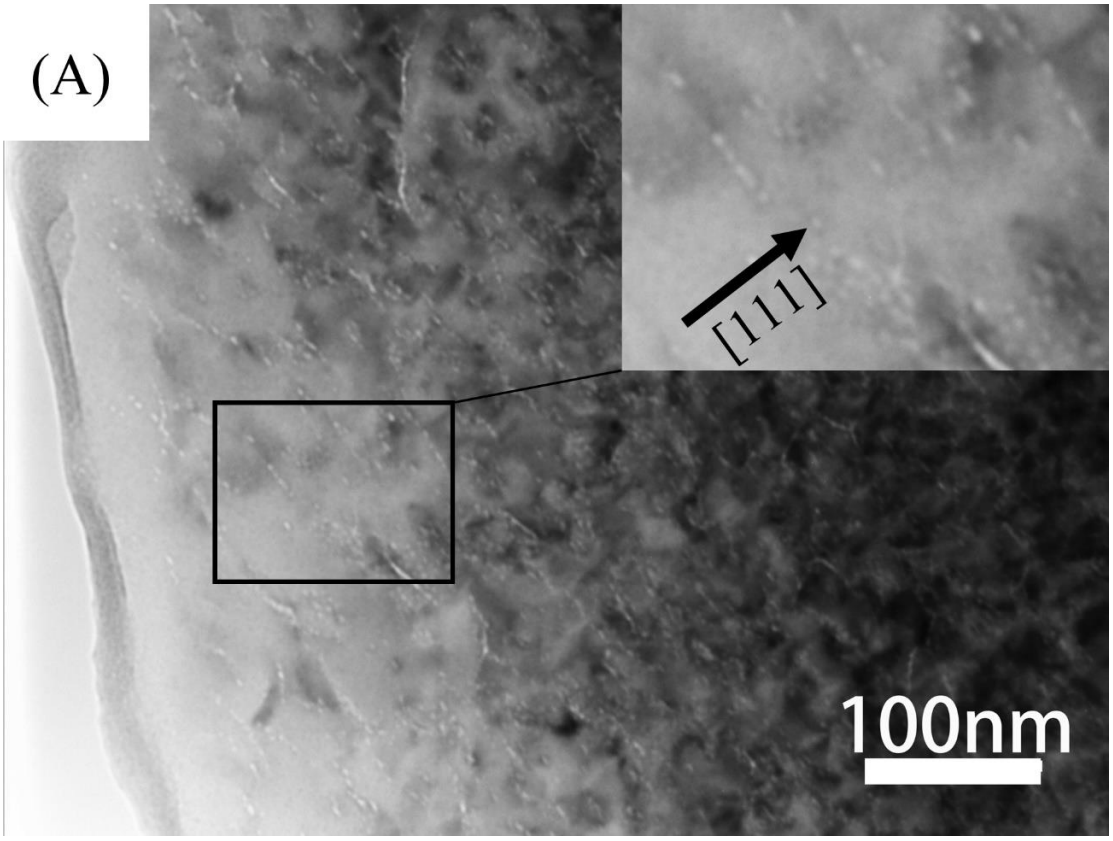

Figure 4.3 TEM micrographs of the as-received r001c21 specimen.

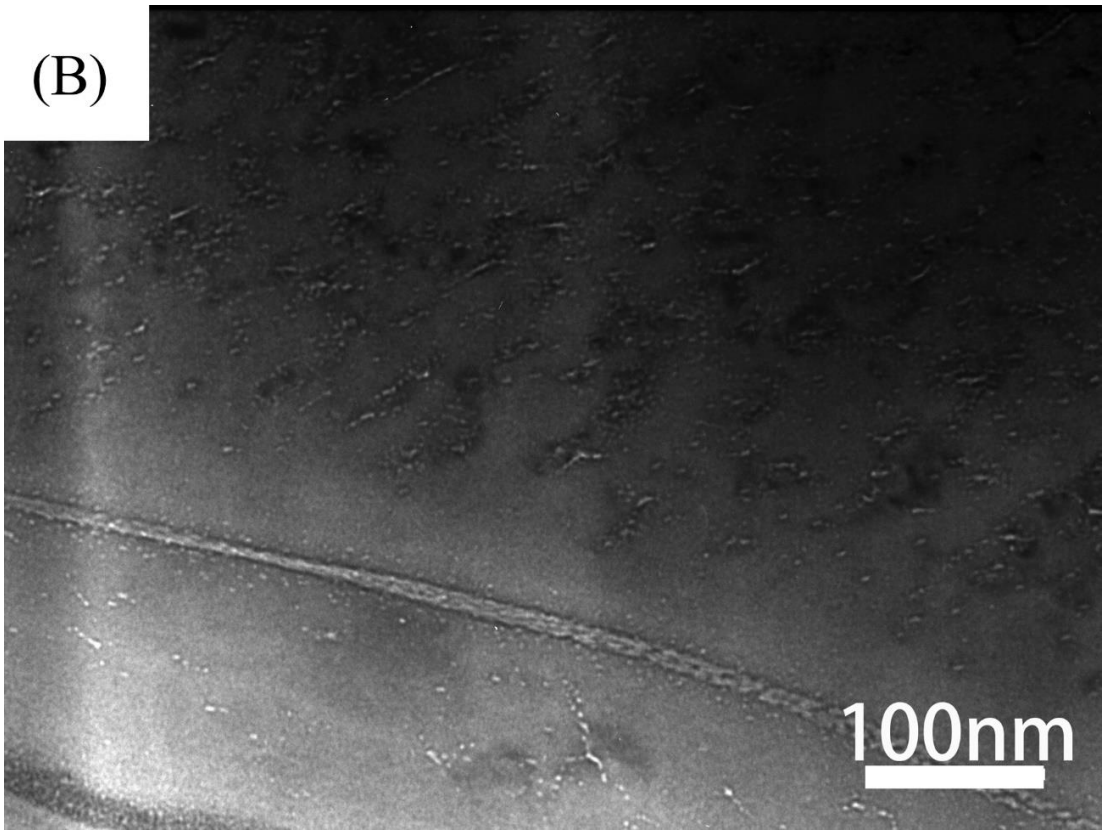

Figure 4.3 (B)

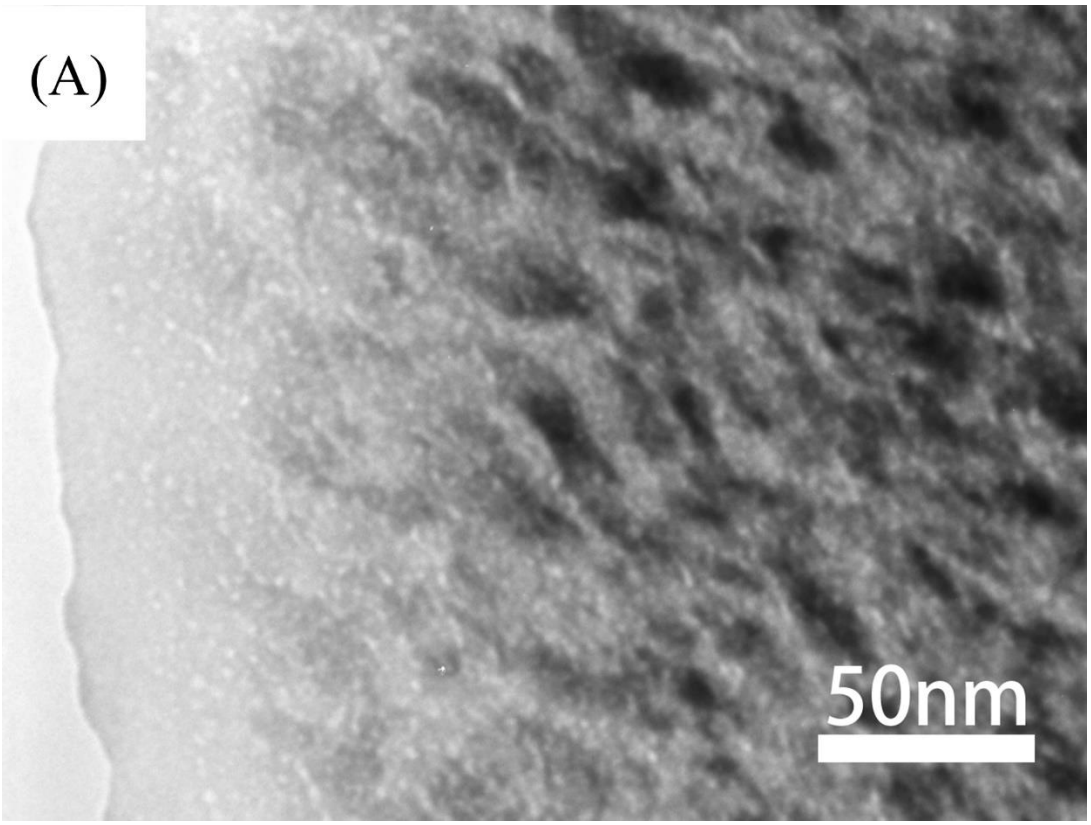

Figure 4.4 TEM micrographs of the as-received r001b21 specimen.

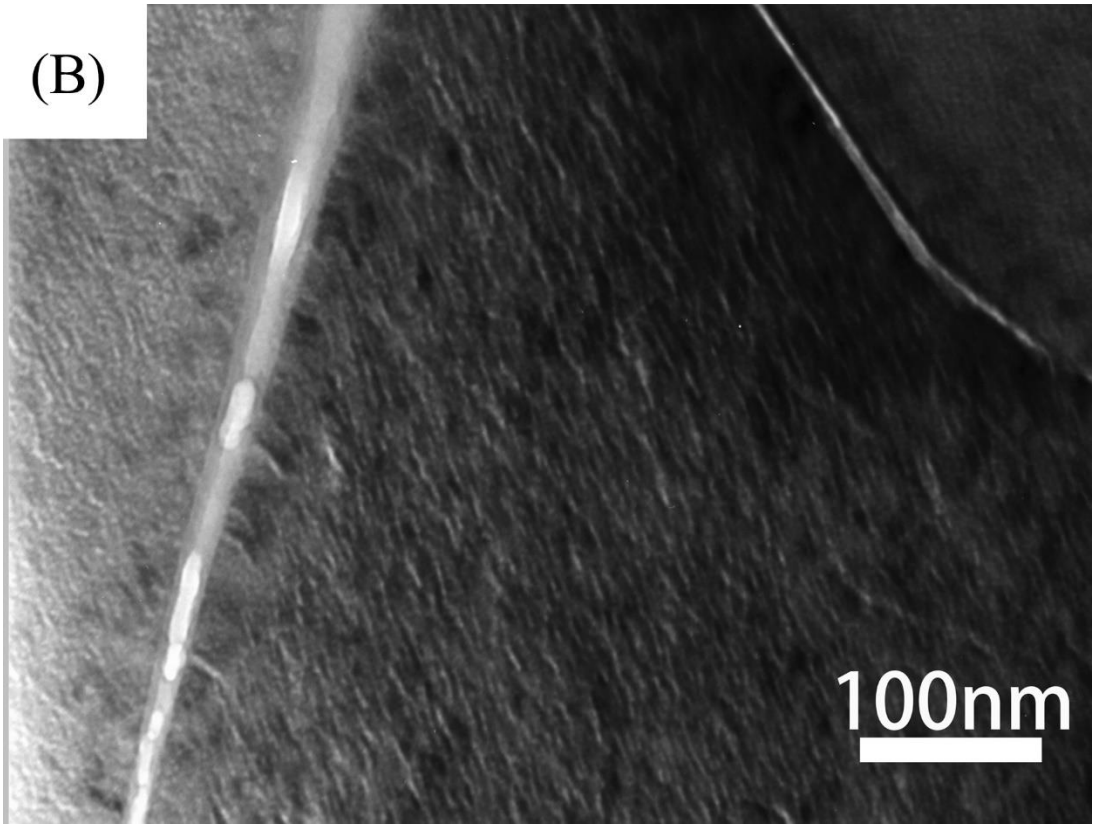

Figure 4.4 (B)

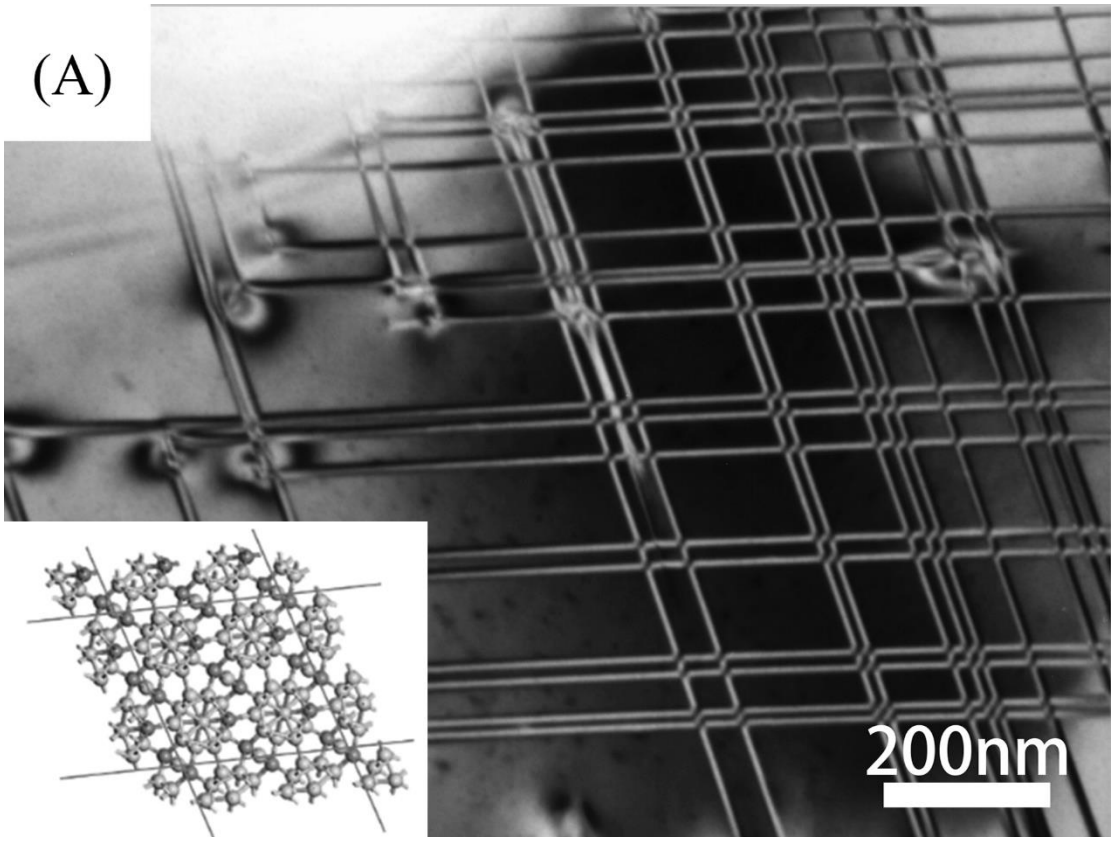

Figure 4.5 TEM micrographs of the B_4C specimen. (A) As-received r001_33 specimen. Insert is structure model of B_4C. (B) As-received r001c21 specimen. (C) The r001b21 specimen after heat-treatment at 1040°C for 10 min, and observed at room temperature.

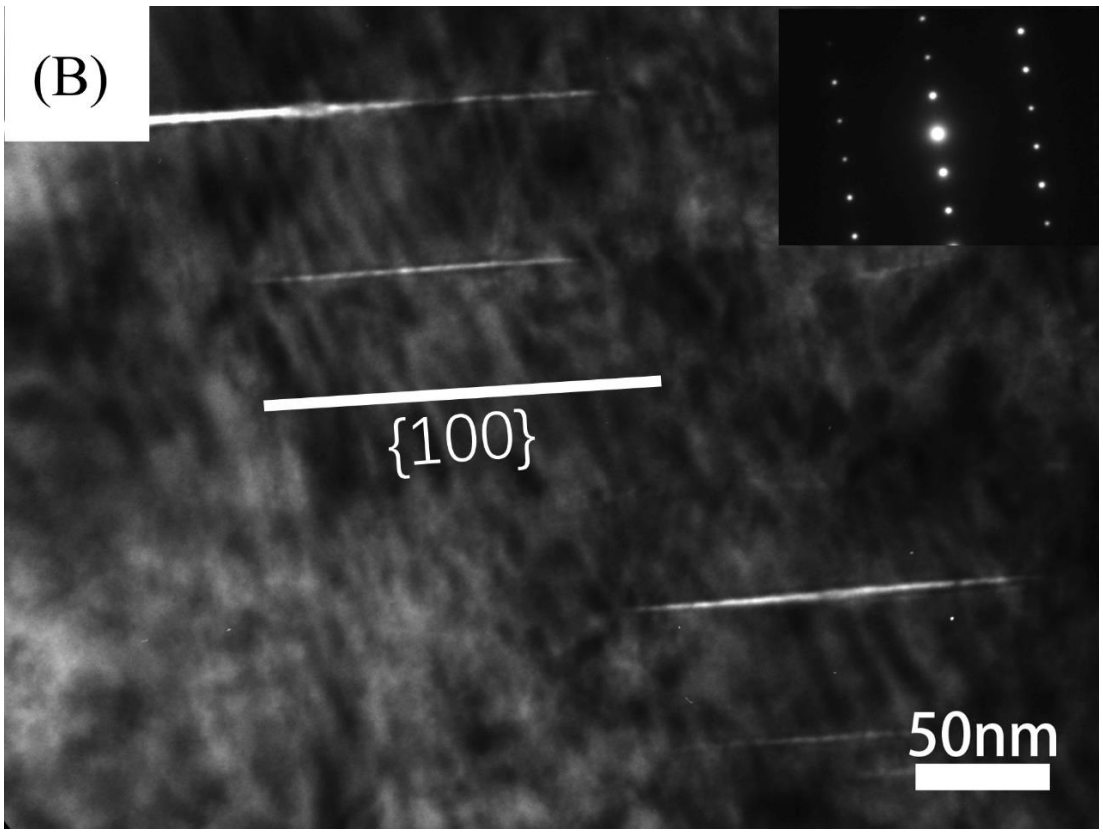

Figure 4.5 (B)

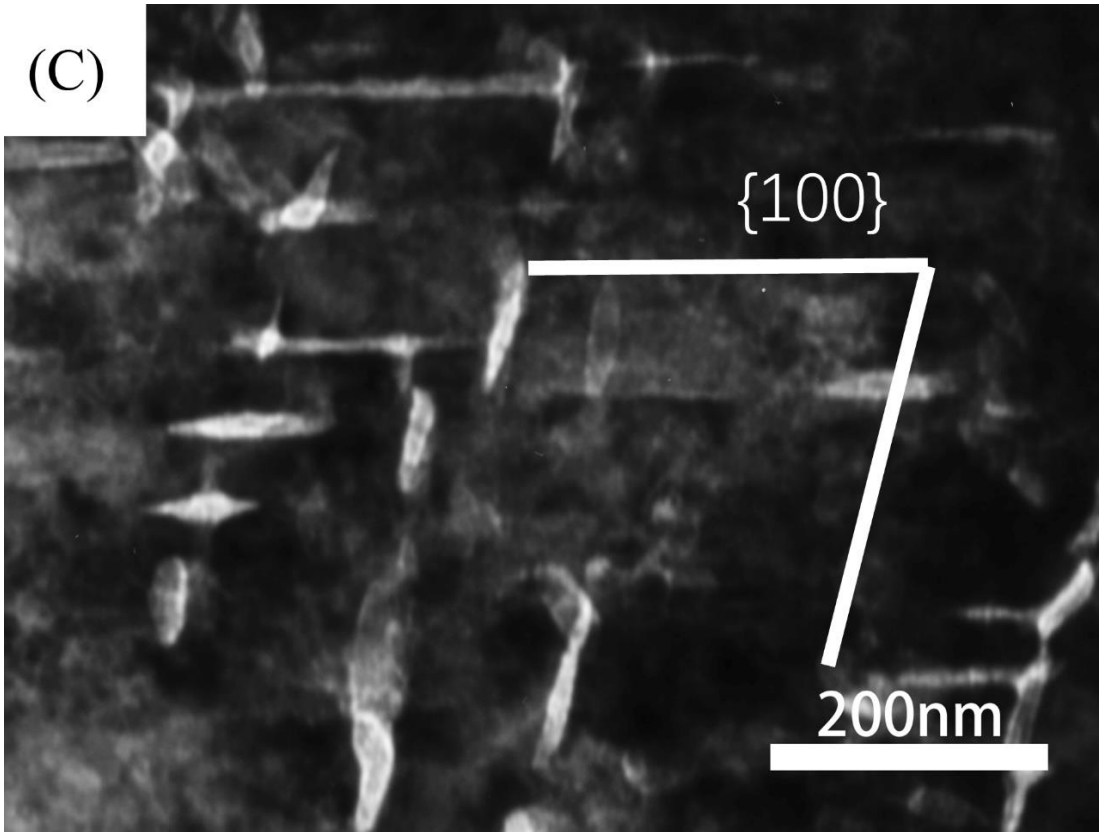

Figure 4.5 (C)

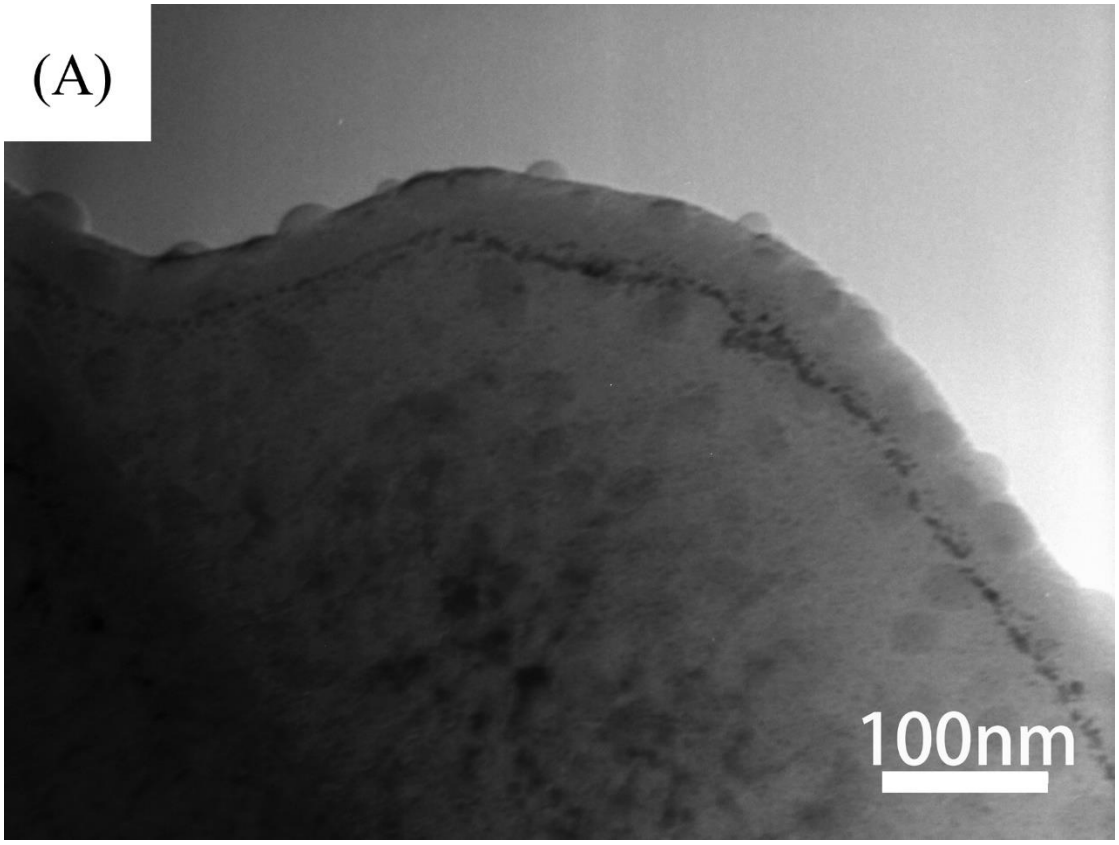

Figure 4.6. TEM micrographs of the r001b21 specimen during and after heating in TEM. (A) Observed at around 800°C. (B) The edge of the same specimen after heating up to 1040°C and then cooled down to room temperature.

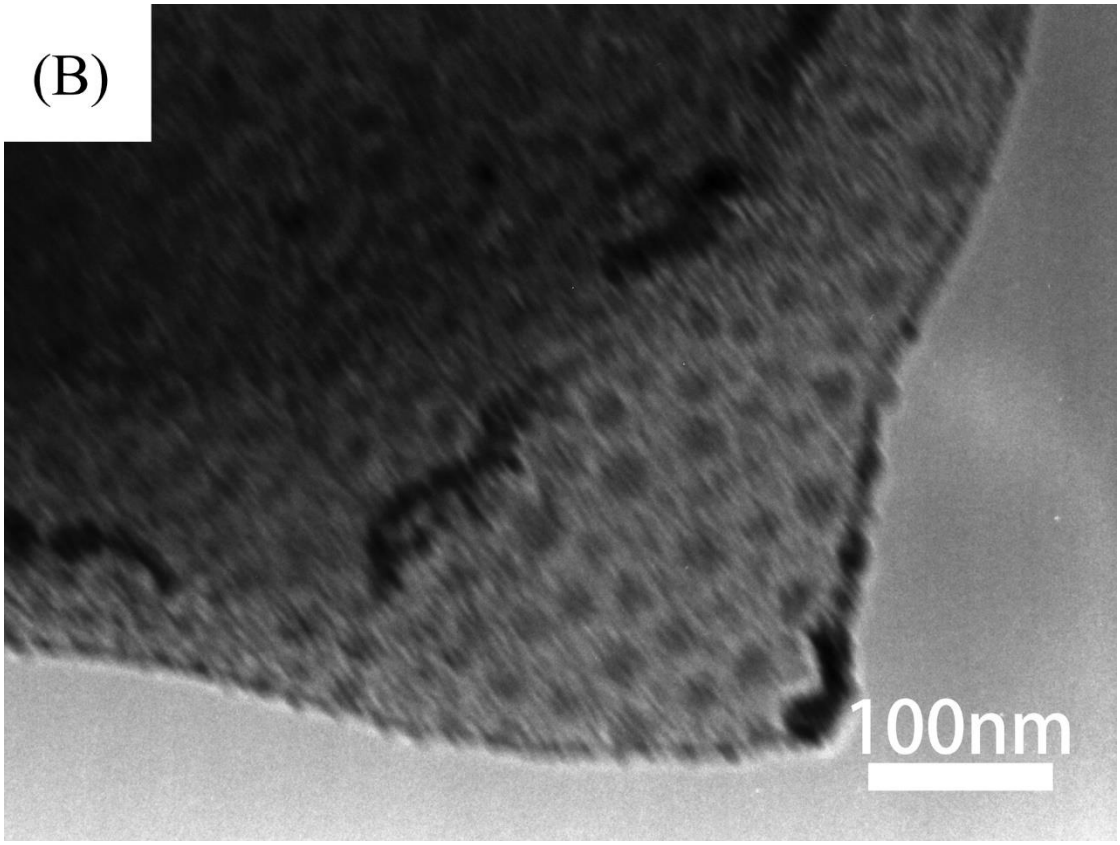

Figure 4.6 (B)

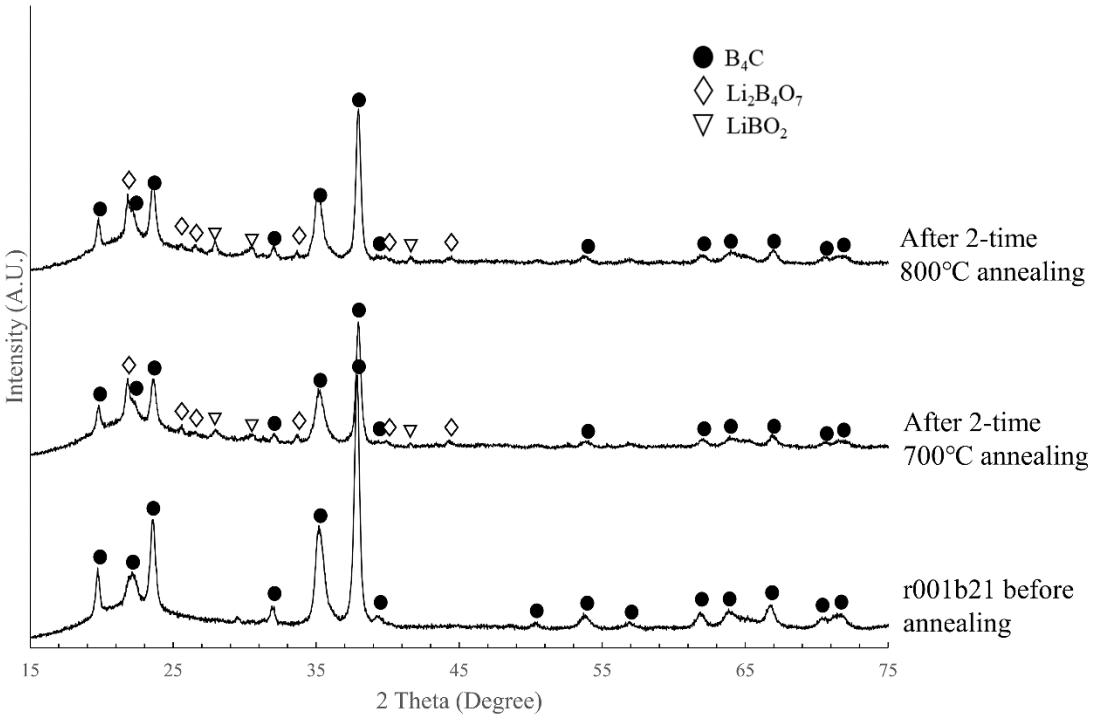

Figure 4.7 XRD patterns of the r001b21 specimen after 2-time heat-treatment at 700°C and 800°C for 1 h.

CHAPTER 5
Density Functional Theory

5.1 Introduction

To further understand the characteristics of the neutron-induced defects on the swelling of B_4C, first principles calculations based on the Density Functional Theory (DFT) were introduced to this study. In this chapter, a brief introduction will be given on the theoretical basis of the DFT method used in the following chapters.

Density Functional Theory (DFT) is one of the most popular methods of "first principles" in quantum chemistry, which provide a convenience way of material modeling and simulation. The DFT method has been widely used in catalyst research, surface science, nanotechnology, semiconductors, etc., and notable successes have been obtained in various fields by using the DFT calculations[1, 2]. To understand the DFT, first, we should know that the idea of "First principles", which means a calculation that started only from the basic physical laws, different from the empirical methods fit to experimental data. The first principles approach to the condensed matters is exactly based on the basic truth that they are made of atoms, and an atom contains a positively charged nucleus and several negatively charged electrons around the nucleus; the interactions of these nuclei and electrons ultimately determine all the physics of the condensed system. The famous Schrödinger equation which made the basis of quantum mechanics, have provided a mean to describe these interactions of microscopic particles.

5.2 The Schrödinger equation

The quantum mechanics have introduced a concept that as simple as the wavefunction

written as Ψ(r, t) contains all the information of the system at a certain state, which gave a possibility to calculate any condensed systems from first principles. The wavefunction of a microscopic system could be obtained by solving the corresponding Schrödinger equation.

Due to the nuclei are much heavier than the electrons (a neutron or proton is more than 1800 times heavier than an electron), the nuclei are much more retarded in response to the energetical changes than the electrons, even we could approximately be considered as relatively static to the electrons. Based on this, the Born–Oppenheimer approximation assumes that the motion of nuclei and electrons can be separately considered. As a result, we can firstly calculate the lowest energy configuration (the ground state) of electrons with the fixed nuclei, and then relax the positions of nuclei to minimize the forces on the nuclei. Wherefore, the Schrödinger equation could be simplified as follow:

$$\hat{H}\Psi = \left[\hat{T} + \hat{V} + \hat{U}\right]\Psi = \left[\sum_{i}^{N}\left(-\frac{\hbar^2}{2m_i}\nabla_i^2\right) + \sum_{i}^{N} V(r_i) + \sum_{i<j}^{N} U(r_i, r_j)\right]\Psi = E\Psi \quad (5.1)$$

Where $\hat{H}$ is the Hamiltonian operator, Ψ is a set of solutions of the Hamiltonian, E is the electronic energy. T is the kinetic energy of each electron, V is the potential energy of the electron-nucleus attraction, U is the interaction energy between different electrons. Thus, for a system with N electrons, each electron has three space coordinates, the Schrödinger equation of this system has 3N variables. In this many-body problem, there is no analytic solution even for as simple as a two-electron system. However, to solve any quantum mechanics problems of materials need to process large numbers of electrons. Therefore, the equation 5.1 still need to be further simplified by a set of approximation to be practical.

5.3 Density Functional Theory

The concept of DFT originated in the Thomas–Fermi model named after Llewellyn

Thomas and Enrico Fermi. The Thomas–Fermi model firstly proposed that to use electron density instead of wavefunctions in the Schrödinger equation. In the Thomas–Fermi model, the total kinetic energy of the electrons could be expressed as

$$\mathrm{T} = C_F \int [n(r)]^{5/3} d^3 r \tag{5.2}$$

$$C_F = \frac{3\hbar^2}{10 m_e} \left(\frac{3}{8\pi}\right)^{2/3} \tag{5.3}$$

In equation 5.2, the total kinetic energy is a function of the electron density, which is a function of electron coordinates. A functional is a function of a function. This is where the DFT got its name.

However, the Thomas–Fermi model is a very rough model that its accuracy was very limited, because of the kinetic energy T is only approximate and the exchange energy was not considered in this model. Though Dirac latterly added a term for exchange energy, it was still inaccurate for most applications. Therefore, it was not until the Hohenberg-Kohn theorems[3] was proved in 1964, that the DFT finally has a solid theoretical foundation.

5.3.1 The Hohenberg-Kohn theorems

The Hohenberg-Kohn theorems are

1) The external potential, and hence the total energy, is a unique functional of the electron density.
2) The functional that delivers the ground state energy of the system, gives the lowest energy if and only if the input density is the true ground state density.

As a result of Theorem 1, we can turn the complex Schrödinger equation of a many-body system with 3N variables into a functional of electron density with only three spatial variables, which could greatly reduce the computational complexity. Moreover, the Theorem 2 allows us to use the variational principle to solve the system ground energy. However, the Hohenberg-Kohn theorems do not specify the way to calculate the electron density of ground state. This problem was solved about a year after the

original Hohenberg-Kohn theorems paper came out, Kohn and Sham[4] provided a feasible method for carrying out DFT calculations.

5.3.2 The Kohn-Sham Equations

According to the Hohenberg-Kohn theorems, the wavefunction Ψ and energy E are functions of electron density n. The electron density n could be expressed as follow

$$\mathrm{n} = \mathrm{n}(r) = N \int dr_1 \cdots \int dr_N \Psi^*(r_1, r_2, \cdots r_N)\Psi(r_1, r_2, \cdots r_N) \tag{5.4}$$

The total energy of the multi-electron system is

$$\mathrm{E}(n) = \Psi^*(n)\hat{H}\Psi(n) = \Psi^*(n)\left(\hat{T} + \hat{U} + \hat{V}\right)\Psi(n) \tag{5.5}$$

As mentioned in equation 5.1, the three terms in the parentheses represent the kinetic energy of the electrons, the Coulomb interactions between the pairs of electrons, and the Coulomb interactions between the electrons and the nuclei. If ignore the interaction between electrons, and assume the electrons are moving individually on their own orbitals, then

$$\mathrm{T}(n) = -\frac{\hbar^2}{2m}\sum_{i=1}^{N}\int d^3r\phi_i^*(r)\nabla^2\phi_i(r) \tag{5.6}$$

The term of coulomb interactions between the electrons could be approximately obtained from the Thomas–Fermi model, which

$$U(n) = \frac{e^2}{2}\int dr \int r' \frac{n(r)n(r')}{|r - r'|} \tag{5.7}$$

The Coulomb interactions between the electrons and the nuclei could be express as

$$V(n) = \int V(r)n(r)dr \tag{5.8}$$

Therefore, an approximation of energy $E_{approx.}$ could be obtained by the combination of these three terms. Every thing that not included which would cause a deviation between the $E_{approx.}$ and the E_{true}, are simply summed up as E_{xc}, the exchange-correlation energy, thus the E_{true} could be written as

$$E_{true}(n) = T(n) + U(n) + V(n) + E_{xc}(n) \tag{5.9}$$

The greatest contribution of the Kohn-Sham equations is that it shows the true

electron density can be expressed by solving a set of equations in which each equation only involves a single electron. Kohn and Sham rewrited the Schrödinger equation in a form of following

$$\left[-\frac{\hbar^2}{2m}\nabla^2 + V(r) + V_H(r) + V_{XC}(r)\right]\Psi_i(r) = \varepsilon_i\Psi_i(r) \qquad (5.10)$$

The three potentials in the square brackets V, V_H, and V_{xc} are the interaction between an electron and the collection of atomic nuclei, the Hartree potential which describes the Coulomb repulsion between the electrons and the total electron density in the system, and the exchange and correlation contributions, respectively. To obtain the electron density of the ground state, the Kohn–Sham equations treated in an iterative way that constantly define a trial electron density in the equations, find the single-particle wave functions, using the obtained single-particle wave functions to calculate the electron density, until the trial electron density is same with the trial electron density which means it is the ground state electron density. Due to there is no accurate way to define the exchange–correlation energy V_{xc}, the accuracy of the Kohn–Sham equations depends largely on the approximation of the exchange–correlation energy.

5.4 Exchange–Correlation Functional

At present, there are many approximation of the Exchange–Correlation Functional have been developed (e.g. the local-density approximation (LDA), the generalized gradient approximation (GGA), the meta-GGA which is an extension of GGA, and the hybrid functionals)[5]. These approximations work well in some systems, while in some systems the performance is not guaranteed. There is still a lack of a universal approximation which could achieve a high accuracy in all systems.

LDA is the simplest approach to define the unknown exchange-correlation functional. Due to the exchange-correlation functional is only known in the uniform electron gas (UEG), it assumes the exchange-correlation potential is equal to the known exchange-correlation potential of the UEG, which:

$$V_{xc}^{LDA} = V_{xc}^{UEG}[n(r)] \tag{5.11}$$

The LDA has been widely used in materials science and chemistry, and showed a good accuracy with the comparison of the experimental results. Meanwhile, it also showed disadvantages of overestimating the bond energies and underestimating the reaction activation energy. Furthermore, in a system with a rapidly changing electron density, the LDA shows poor accuracy because of the simple assumption of LDA is no longer appropriate.

To solve the problems of the LDA, the GGA was latterly developed with the gradient of the electron density considered. The GGA is given by:

$$V_{xc}^{GGA} = V_{xc}[n(r), \nabla n(r)] \tag{5.12}$$

There are many distinct GGA functionals have been developed, including the Becke-Lee-Yang-Parr (B-LYP)[6, 7], the PW91[8], and the Perdew-Berke-Ernzerhof (PBE)[9]. Comparing to the LDA, GGA can predict more accurately in the system energy, binding energy, and activation energy. However, it also may overestimate the lattice parameters.

References

1. Hafner J, Wolverton C, Ceder G. Toward Computational Materials Design: The Impact of Density Functional Theory on Materials Research. MRS Bulletin. 2006;31:659-68.

2. Burke K. Perspective on density functional theory. The Journal of Chemical Physics. 2012;136:150901. Epub 2012/04/24.

3. Hohenberg P, Kohn W. Inhomogeneous Electron Gas. Phys Rev. 1964;136:B864-B71.

4. Kohn W, Sham LJ. Self-Consistent Equations Including Exchange and Correlation Effects. Phys Rev. 1965;140:A1133-A8.

5. Orio M, Pantazis DA, Neese F. Density functional theory. Photosynth Res. 2009;102:443-53. Epub 2009/02/25.

6. Becke AD. Density-functional exchange-energy approximation with correct asymptotic behavior. Physical Review A. 1988;38:3098-100.

7. Lee C, Yang W, Parr RG. Development of the Colle-Salvetti correlation-energy formula into a functional of the electron density. Phys Rev B. 1988;37:785-9.

8. Perdew JP, Wang Y. Accurate and simple analytic representation of the electron-gas correlation energy. Phys Rev B. 1992;45:13244-9.

9. Perdew JP, Burke K, Ernzerhof M. Generalized Gradient Approximation Made Simple. Phys Rev Lett. 1996;77:3865-8. Epub 1996/10/28.

CHAPTER 6
First-principles investigation of neutron-irradiation-induced point defects in B_4C

6.1 Introduction

The XRD analysis results in chapter 3 showed an anisotropic change in the lattice parameters of the neutron-irradiated B_4C; the a-axis expanded while the c-axis shrank, where this change was recoverable by post-irradiation annealing. From TEM study in chapter 4, the helium gas is found tend to form a flat disc-like shape with the plane of the plate parallel to the (111) rhombohedral plane in helium-implanted and neutron-irradiated B_4C samples. It is thought possible to control the volume swelling of B_4C pellets considering this anisotropic lattice expansion by neutron irradiation since a method of fabricating orientation-controlled polycrystalline B4C pellets using a strong magnetic field is under development[1].

It is clear that the recovery of the swelling of B_4C after post-irradiation heat treatment was a direct consequence of the interaction and elimination dynamics of the irradiation-induced defects. However, to date, the behavior of neutron-irradiation-induced defects in B_4C is not well understood. Therefore, as a first step in understanding the effect of neutron irradiation on B_4C at the atomic scale, here, we investigated the energetics of formation and migration of the neutron-induced point defects in B_4C by first-principles calculations based on density functional theory (DFT). Results of this study suggested that the icosahedra structures of the B_4C crystal have a strong resistance to irradiation while the C-B-C linear chains are much more likely to be destroyed by the neutron irradiation; the products of the neutron-absorption reaction, helium and lithium atoms, have significantly lower migration energy barriers along the

rhombohedral (111) plane than perpendicular to this plane.

The motivation of this work was to advance the understanding of defect diffusion mechanisms in B_4C and provide a theoretical basis for further research of B_4C materials for its use in control rods.

A recently published study calculated the formation and migration energies of the helium interstitials in B_4C[2]. They used the Vienna Ab-initio Simulation Package (VASP)[3] for the calculation and the projector augmented wave (PAW) method[4] was used for the electron-ion interactions. We compared our results with those of this study and found that our independent results had similar conclusions.

6.2 Computational methods and structure models

Boron carbide is generally considered to crystallize in the $R\bar{3}m$ space group. The B_4C with a carbon ratio of 20% has been most commonly used in the stoichiometric form; therefore, all calculations in this study were based on this form of B_4C. The structure of our B_4C model had one carbon in the polar site of each icosahedron (the atoms bond the icosahedra together), and with C-B-C configured linear chains between the icosahedra, commonly be written as $(B_{11}C^p)CBC$, as shown in **Figure 6.1**. This configuration of B_4C has been reported to have the lowest energy in some previous DFT studies[5, 6, 7]. Our calculations also showed that the energy of the $(B_{11}C^p)CBC$ configuration was approximately 2.95 eV per hexagonal cell $(B_{11}C^p)CBC$ lower than the $(B_{12})CCC$ configuration, and 1.27 eV lower than the model with the carbon at the equatorial site, the $(B_{11}C^e)CBC$ configuration. Our $(B_{11}C^p)CBC$ structure model was fully relaxed; all calculations on the irradiation defects were carried out on the 2×2×1 supercell based on this model.

All calculations were based on DFT and performed using the Cambridge Sequential Total Energy Package (CASTEP) of the BIOVIA Materials Studio version 7.0[8, 9]. The ultra-soft pseudopotential method was used for the interactions between the ionic cores and electrons[10]. The Generalized Gradient Approximation of the

Perdew-Burke-Ernzerhof approach (GGA-PBE) was used for calculating the electronic exchange-correlation energy[11]. A plane-wave cut-off energy of 400 eV was used. Only a single k-point at the Γ-point was used in the calculation of the 2×2×1 supercell-based model by considering the calculation cost-effectiveness; the energy change was less than 0.01 eV/atom compared to using a 2×2×2 k-point mesh of Brillouin zone sampling. All calculations used a convergence tolerance of maximum energy difference of 1×10^{-6} eV, maximum force of 0.01 eV/Å, and maximum displacement of 5×10^{-4} Å. The geometry optimization was performed using the Broyden-Fletcher-Goldfarb-Shannon (BGFS) algorithm[12]. Both the cell parameters and the fractional coordinates of the atoms were fully optimized for the initial models of each defect type (vacancy, interstitial lithium, and interstitial helium). Then, the cell parameters were fixed during the geometry optimization of the models containing the same defect type sitting at different positions to meet the requirement of the transition state searching calculations for calculating the migration energy. The effect of fixing the lattice parameters on the calculations of defect formation energies was found to be insignificant during our pre-calculations.

The formation energies of defects were calculated using the following equation[13, 14, 15]:

$$E^f = E_{def} - E_{perf} + n_i\mu_i \tag{6.1}$$

where E_{perf} and E_{def} are the total energies of the perfect structure model and the defective structure model, respectively, and n_i and μ_i are the number change and chemical potentials in the B_4C of element i (B, C, Li, He, etc.), respectively. However, it is difficult to obtain the chemical potentials of each element in B_4C. Therefore, we introduced α-rhombohedral boron, and graphite as reference phases for calculating the approximate value of μ_i for B and C. The μ_i for Li and He were calculated from single isolated Li and He atom, respectively.

The migration energies of the defects were calculated by performing transition state searching processes between the starting and end defect models. The complete linear synchronous transit/quadratic synchronous transit (LST/QST) method was used for the

transition state searches.

6.3 Results

6.3.1 Vacancy-type defects

Under neutron irradiation, atoms in materials can be knocked out from the original lattice sites by collision with neutrons with high kinetic energy, leaving vacancies. The mechanism of the production and recombination of Frenkel pairs is very important when studying the neutron irradiation tolerance of materials. As shown in Figure 6.1, the lattice sites in B_4C can be generally divided into five types; polar boron sites (B5–B7), polar carbon sites (C1), equatorial boron sites (B1–B4), chain end carbon sites (C2, C3), and chain center boron sites (B8). Although the polar carbon reduced the symmetry of the lattice, meaning that all the polar boron and equatorial sites are not exactly equivalent, the similar properties of boron and carbon in atomic sizes and electronic properties make the vacancy-type defects affiliated to the same category have little differences in energies.

The results of the calculations of the formation energies for the vacancy-type defects are shown in **Table 6.1**. The vacancies on the icosahedron had much higher formation energies (~3 eV higher) than the vacancies on the C-B-C linear chain. The vacancy site at the center of the linear chain had the lowest formation energy of 1.66 eV, which means that the center boron atom of the C-B-C linear chain was very easily knocked out at the end of collision cascades induced by neutrons or other particles with high kinetic energy. As Kwei et al.[16] indicated that there is a large vacancy concentration at the center of the three-atom chains from neutron powder diffraction. First-principles studies of Saal et al.[17] and Betranhandy et al.[18] shows a low vacancy formation energy at the center of the C-B-C chain. Our results agree well with these previous works.

After performing geometry optimizations of the structure models with a vacancy

on the icosahedron, the chain center boron atom of the nearby C-B-C chain was attracted to the vacancy, resulting in significantly bending of the chain. **Figure 6.2** shows the C-B-C chain bent by the vacancy at the closest equatorial site B1. Furthermore, the vacancy at the equatorial site B4 directly took away the center boron atom from the neighboring C-B-C chain during the geometry optimization; thus, the vacancy at B4 is thought to be unstable.

The mobility of vacancy-type defects was investigated by transit state searching between these vacancy configurations. The results showed that the migration energy of a vacancy on the equatorial site (B1) of an icosahedron to the closest center site (B8) of the C-B-C chain was extremely low, approximately 0.18 eV. Moreover, the migration energies between the neighboring equatorial and polar sites were also as low as ~1 eV. However, it was much more difficult for a vacancy on the C-B-C chain to migrate to the neighboring icosahedron as the formation energies of vacancies on the icosahedron were about 3 eV higher than those of the vacancy defects on the chain. Therefore, the vacancies at the equatorial sites were considered metastable and would rapidly be transferred to the chain center sites. The results of the calculations revealed that the icosahedral cage structures in B_4C were far more resistant to neutron irradiation than the linear chains as the atoms on the icosahedra were harder to knock out at the end of the collision cascade; the vacancies formed on the icosahedra could rapidly migrate to the nearby chain sites to keep the icosahedral structures intact.

6.3.2 Interstitial-type defects

As shown in the schematic diagram in **Figure 6.3**(a), our calculations showed that, in addition to the center of the icosahedral cage, there were eight stable inter-icosahedra interstitial sites for helium atoms affiliated to each C-B-C chain. We calculated the formation energies of the helium interstitial defects of the center C-B-C chain (i-He_1, i-He_2, …, i-He_8), which are shown in Figure 6.3(b). The calculated formation energies for helium interstitials are listed in **Table 6.2**. All inter-icosahedra helium interstitials

have formation energies around 3 eV, while the helium atom sitting at the center of an icosahedron (i-He_9) had a significantly higher formation energy of 7.1 eV. The excessive formation energy of the inter-icosahedra sites for helium atoms showed that it is an unfavorable interstitial site. In addition, it is unlikely that the helium atom at the center of the cage can break the intact cage and escape. Thus, we excluded these sites for the subsequent migration energy investigation.

We selected the optimized structures of interstitial-type defects of i-He_2, i-He_3, i-He_5, i-He_4' (as shown in Figure 6.3(b)), and i-He_7 as the focus for the calculations of the migration energies of the interstitial helium atom in B_4C. Considering the possible migration paths of helium, we performed transition-state searching between five paths in the helium interstitial structure models; i-He_3 and i-He_5, i-He_3 and i-He_4', i-He_3 and i-He_2, i-He_3 and i-He_7, and i-He_4' and i-He_7. These results are shown in **Table 6.3**. As the i-He_4' site was very close to the i-He_7 site, only a small amount of energy was required for a helium atom to jump between the i-He_7 and i-He_4' sites. It is worth noting that every i-He_7 and i-He_8 site was actually sitting at the center of an equilateral triangle consisting of three interstitial sites of other C-B-C chains (as shown in **Figure 6.4**), so that the helium interstitial atoms could easily migrate between different C-B-C chains by bypassing the i-He_7 or i-He_8 sites. However, the migration barrier between the i-He_3 and i-He_7 sites of 2.19 eV were high compared to the barrier of 1.35 eV between i-He_3 and i-He_5; hence, it is thought to be an unfavorable path for interstitial helium diffusion. It is reasonable to assume that the helium interstitial atoms are more inclined to migrate in a horizontal layer aligned along the (111) rhombohedral plane, as shown in Figure 6.4, because an ~62% higher energy was needed to overcome the migration barrier for the helium interstitial atoms migrating vertically to another layer.

Similarly, the interstitial sites discussed above can also apply to the lithium interstitials. We calculated formation and migration energies for the lithium interstitial-type defects following the same calculation method as for the helium interstitial atoms and these results are listed in **Table 6.4** and **6.5**, respectively. The lithium interstitial-type defects had much smaller formation energies of 0.53 eV (average) at the inter-

icosahedra interstitial sites than ~3.00 eV for those corresponding to interstitial helium. Therefore, the lithium atoms could be more easily dissolved in the B_4C lattice than the helium atoms. The interstitial site inside the icosahedron was still an unfavorable site for the lithium atoms as the formation energy was 9–17 times higher than the inter-icosahedra interstitial sites. By comparing the migration energies of each path, it was obvious that the lithium interstitial atoms also followed the same migration route of the helium interstitial atoms. There was a barrier of only ~1 eV for the lithium interstitials to migrate among the interstitial sites in the same horizontal layer, which was lower than the migration barrier of 1.35 eV for the helium interstitials. However, the migration barrier was even higher for the lithium interstitials to migrate vertically among the different horizontal layers than the migration barrier of the helium interstitials. It is supposed that the lithium atoms could diffuse faster than helium atoms in B_4C, and showed a more obvious tendency of horizontal diffusion parallel to the (111) rhombohedral plane than the helium interstitials.

In addition to the products of the neutron-absorption reaction, helium and lithium atoms, we also investigated the interstitial boron and carbon atoms, which can be removed from their original lattice sites by the collision of neutrons. Our calculations showed that the carbon and boron interstitials acted very differently than the lithium and helium interstitials. The boron and carbon interstitials were electrostatically bonded to the closest icosahedron atoms and chain center boron atom (as shown in **Figure 6.5**), respectively, making it difficult for them to migrate freely in the B_4C crystal like the lithium and helium interstitials can. The formation energies of these interstitial boron and carbon defects were approximately 4.2 eV and 5.3 eV, respectively. The formation energies were larger than those of the helium and lithium interstitials. However, it was negligible when taking into account the kinetic energy of the fast neutrons (~1 keV) and the energy released per neutron-capture reaction of ^{10}B (2.4 MeV). A large amount of Frenkel pairs of boron and carbon should be created during neutron irradiation. In addition, the vacancies on the icosahedra have a strong ability to capture the knocked-out boron and carbon atoms to keep an intact icosahedral structure. This mechanism is

believed to be the main process for the annihilation of the irradiation-induced Frenkel pairs.

6.3.3 Discussion

The calculation results for the vacancies and the B and C interstitials in B_4C clearly showed that the icosahedral cage structures in B_4C had good neutron irradiation tolerance resulting from the capture of the center atoms of the chains and knocked-out carbon and boron atoms. As a result, many vacancies would be created, which firstly migrated to the center sites of the C-B-C linear chains. Moreover, these vacancies did not affect the crystallinity of boron carbide. This is probably why there are few reports on the amorphization of the B_4C by neutron irradiation. Gosset et al.[19] used 4-MeV Au ions to irradiate a bulk B_4C sample at room temperature with a dose of more than $10^{15}/cm^2$, and observed partial amorphization of B_4C by TEM. Considering that the temperature in SFRs is more than 500°C, the defect migration is faster than at room temperature, meaning that B_4C control rod pellets can withstand more radiation without amorphization. In addition, Carrard et al.[20] observed strong self-healing of electron-irradiation-induced defects on the icosahedra of boron-based materials by TEM investigation. Huber et al.[21] studied the self-healing properties of $B_{12}P_2$ by DFT calculations and reported very low recombination energies (0.003 eV) for Frenkel pairs. These results lead to the same conclusion that the icosahedra in boron-rich materials have very strong defect recovery ability. Therefore, we conclude that the impact of the neutron knock-out effect on the strength deterioration of B_4C pellets during irradiation is small.

The migration energies of helium in B_4C obtained in this study were very close to the values reported by Schneider et al.,[2] as shown in **Table 6.3** and **6.5**. The significant differences in the migration barriers for both helium and lithium atoms in different migration directions revealed that they tended to follow a two-dimensional diffusion regime parallel to the rhombohedral (111) plane in B_4C. We hypothesized that

the formation of flat disk-like helium bubbles was due to the rapid migration and coalescence of helium atoms along the (111) plane. We observed tiny helium bubbles connected in strings parallel to the (111) plane in our previous TEM study, which implied this kind of bubble merger. Helium bubbles remaining in the pellets are thought to be the main contribution to the volume expansion of the B_4C pellets, based on the anisotropic characteristics of the helium in B_4C. Optimization of the microstructure is expected to achieve B_4C absorber pellets with improved capability for excluding helium gas from the pellets by aligning most of the grains in the same direction. The obviously small formation and migration energies of the lithium interstitials suggested that the lithium could also very easy dissolve in the B_4C lattice and diffuse rapidly at relatively low temperatures while having little impact on the B_4C lattice. This explains why it was difficult to find traces of the lithium by electron microscopy. We detected a significant amount of lithium borate by XRD due to lithium migration to the surface of neutron-irradiated B_4C powder after two cycles of heating at 700°C for 1 h each in an inert atmosphere (described in chapter 4). This could be evidence of the lithium atoms produced by neutron irradiation being hidden in the grains of B_4C.

However, because the DFT calculations were limited to a small model of the B_4C grain, the calculated migration energies were not applicable to describe diffusion along the grain boundaries, although they played a significant role in the diffusion of helium and lithium in polycrystalline B_4C pellets. A pioneering investigation of the helium diffusion in boron carbide using the $^3He(d,p)^4He$ nuclear reaction (NRA method) was conducted by Motte et al.[22] and the activation energy, E_a, of helium obtained from the Arrhenius diagram was 0.523 ± 0.107 eV. This value was very low compared to the DFT calculation result of 1.35 eV for the two-dimension diffusion path of helium. Similarly, Deschanels et al.[23] experimentally measured the lithium diffusion coefficient in irradiated B_4C and the calculated E_a for lithium was 0.19 eV for temperatures below 948 K and 0.88 eV temperatures above 948 K, which were lower than our calculated result (1.01 eV). There was no evidence that their obtained lithium diffusion coefficient was that of the Li inside the B_4C grain; however, in actual B_4C

control rod pellets, the diffusion mechanisms are more complicated than the simple migration of helium and lithium atoms from one interstitial site to another. This makes it very difficult to directly compare the results of the DFT calculation and the experiments from previous research works. However, the results of our calculations show no contradictions with the previous experimental observations and could explain phenomena such as the formation of the disk-like helium bubbles and strong irradiation resistance of B_4C.

6.4 Conclusions

The behaviors of vacancy-type and interstitial-type defects in B_4C were studied through DFT calculations. It is shown that the icosahedral cage structures in B_4C were quite stable under neutron irradiation. An obvious consequence for a neutron-irradiated B_4C absorber is that it would contain a lot of vacancies concentrated at the C-B-C chain center sites. Helium and lithium atoms produced by the neutron-capture reaction of ^{10}B could dissolve in the inter-icosahedra sites of the B_4C lattice. The results of the migration energy calculations revealed that both lithium and helium atoms tended to follow a two-dimensional diffusion regime along the (111) rhombohedral plane at low temperature. This anisotropic diffusion characteristic of helium could promote migration and merging of the initially-formed helium atoms along the (111) plane. This can explain the formation of the flat disk-like helium bubbles in neutron-irradiated B_4C pellets observed from TEM images. The anisotropic diffusion property of helium in B_4C has the potential to be applied in the future material design of long-life B_4C absorber for fast reactors.

References

1. Grasso S, Hu CF, Vasylkiv O, Suzuki TS, Guo SQ, Nishimura T, Sakka Y. High-hardness B4C textured by a strong magnetic field technique. Scripta Mater. 2011;64:256-9.

2. Schneider A, Roma G, Crocombette J-P, Motte V, Gosset D. Stability and kinetics of helium interstitials in boron carbide from first principles. J Nucl Mater. 2017;496:157-62.

3. Kresse G, Furthmüller J. Efficient iterative schemes forab initiototal-energy calculations using a plane-wave basis set. Phys Rev B. 1996;54:11169-86.

4. Kresse G, Joubert D. From ultrasoft pseudopotentials to the projector augmented-wave method. Phys Rev B. 1999;59:1758-75.

5. Lazzari R, Vast N, Besson JM, Baroni S, Dal Corso A. Atomic Structure and Vibrational Properties of Icosahedral B_4C Boron Carbide. Phys Rev Lett. 1999;83:3230-3.

6. Vast N, Sjakste J, Betranhandy E. Boron carbides from first principles. J Phys: Conf Ser. 2009;176.

7. Mauri F, Vast N, Pickard CJ. Atomic structure of icosahedral B4C boron carbide from a first principles analysis of NMR spectra. Phys Rev Lett. 2001;87:085506. Epub 2001/08/11.

8. Segall MD, Lindan PJD, Probert MJ, Pickard CJ, Hasnip PJ, Clark SJ, Payne MC. First-principles simulation: ideas, illustrations and the CASTEP code. J Phys: Condens Matter. 2002;14:2717-44.

9. Clark SJ, Segall MD, Pickard CJ, Hasnip PJ, Probert MJ, Refson K, Payne MC. First principles methods using CASTEP. Z Kristallogr. 2005;220:567-70.

10. Vanderbilt D. Soft self-consistent pseudopotentials in a generalized eigenvalue formalism. Phys Rev B: Condens Matter. 1990;41:7892-5.

11. Perdew JP, Burke K, Ernzerhof M. Generalized Gradient Approximation Made Simple. Phys Rev Lett. 1996;77:3865-8. Epub 1996/10/28.

12. Head JD, Zerner MC. A Broyden-Fletcher-Goldfarb-Shanno Optimization Procedure for Molecular Geometries. Chem Phys Lett. 1985;122:264-70.

13. Wang J, Liu B, Wang J, Zhou Y. Theoretical investigation of thermodynamic stability and mobility of the intrinsic point defects in Ti_3AC_2 (A=Si, Al). Phys Chem Chem Phys. 2015;17:8927-34. Epub 2015/03/10.

14. Zhao S, Xue J, Wang Y, Huang Q. Ab initio study of irradiation tolerance for different $M_{n+1}AX_n$ phases: Ti_3SiC_2 and Ti_3AlC_2. J Appl Phys. 2014;115.

15. Zhang G, Xiang X, Yang F, Peng X, Tang T, Shi Y, Wang X. Helium stability and its interaction with H in alpha-Al_2O_3: a first-principles study. Phys Chem Chem Phys. 2016;18:1649-56. Epub 2015/12/18.

16. Kwei GH, Morosin B. Structures of the Boron-Rich Boron Carbides from Neutron Powder Diffraction: Implications for the Nature of the Inter-Icosahedral Chains. The Journal of Physical Chemistry. 1996;100:8031-9.

17. Saal JE, Shang S, Liu Z-K. The structural evolution of boron carbide via ab initio calculations. Appl Phys Lett. 2007;91.

18. Betranhandy E, Vast N, Sjakste J. Ab initio study of defective chains in icosahedral boron carbide B_4C. Solid State Sci. 2012;14:1683-7.

19. Gosset D, Miro S, Doriot S, Victor G, Motte V. Evidence of amorphisation of B4C boron carbide under slow, heavy ion irradiation. Nucl Instrum Methods Phys Res, Sect B. 2015;365:300-4.

20. Carrard M, Emin D, Zuppiroli L. Defect clustering and self-healing of electron-irradiated boron-rich solids. Phys Rev B: Condens Matter. 1995;51:11270-4.

21. Huber SP, Gullikson E, Frye CD, Edgar JH, de Kruijs RWEV, Bijkerk F, Prendergast D. Self-healing in $B_{12}P_2$ through Mediated Defect Recombination. Chem Mater. 2016;28:8415-28.

22. Motte V, Gosset D, Miro S, Doriot S, Surble S, Moncoffre N. Helium behaviour in implanted boron carbide. Epj Nucl Sci Technol. 2015;1.

23. Deschanels X, Simeone D, Bonal JP. Determination of the lithium diffusion coefficient in irradiated boron carbide pellets. J Nucl Mater. 1999;265:321-4.

Table 6.1 The formation energies (in eV) of vacancy defects in B_4C

	Vacancy site	Formation energy
Vacancy site on the icosahedron	B1	5.56
	B2	4.68
	B3	4.73
	B4	unstable
	B5	6.29
	B6	5.68
	B7	4.73
	C1	4.94
Vacancy site on the Chain	B8	1.66
	C2	2.59
	C3	2.69

Table 6.2 The formation energies (in eV) of helium interstitial defects, with the comparison of results from Schneider et al.[2] shown in the right.

	Interstitial site	E_f	Ref. 22
Inter-icosahedra interstitial sites	i-He_1	3.00	2.89–3.01
	i-He_2	2.97	
	i-He_3	2.97	
	i-He_4	2.98	
	i-He_5	2.97	
	i-He_6	2.97	
	i-He_7	2.95	2.96–3.25
	i-He_8	3.26	
Inside the icosahedron	i-He_9	7.14	–
Inter-icosahedra interstitial site affiliated to an C-B-C chain of the upper layer	i-He_4'	2.97	7.23

Table 6.3 The calculated migration energies (in eV) between the selected positions of helium interstitials with the results of the same migration paths from Schneider et al.[2] shown in the right.

Migration path	E_m	Ref. 22
i-He_3 → i-He_5	1.35	1.21
i-He_3 → i-He_2	1.87	–
i-He_3 → i-He_7	2.19	–
i-He_3 → i-He_4’	2.17	2.22
i-He_4’ → i-He_7	0.08	0.13–0.35

Table 6.4 The formation energies in eV of lithium interstitial defects

	Interstitial site	E_f
Inter-icosahedra interstitial sites	i-Li_1	0.33
	i-Li_2	0.61
	i-Li_3	0.61
	i-Li_4	0.59
	i-Li_5	0.59
	i-Li_6	0.42
	i-Li_7	0.43
	i-Li_8	0.62
Inside the icosahedron	i-Li_9	5.66
Inter-icosahedra interstitial site affiliated to an C-B-C chain of the upper layer	i-Li_4'	0.59

Table 6.5 The migration energies (in eV) between the selected positions of lithium interstitials

Migration path	E_m
$i\text{-}Li_3 \rightarrow i\text{-}Li_5$	1.01
$i\text{-}Li_3 \rightarrow i\text{-}Li_2$	2.42
$i\text{-}Li_3 \rightarrow i\text{-}Li_7$	2.19
$i\text{-}Li_3 \rightarrow i\text{-}Li_4'$	2.18
$i\text{-}Li_4' \rightarrow i\text{-}Li_7$	0.02

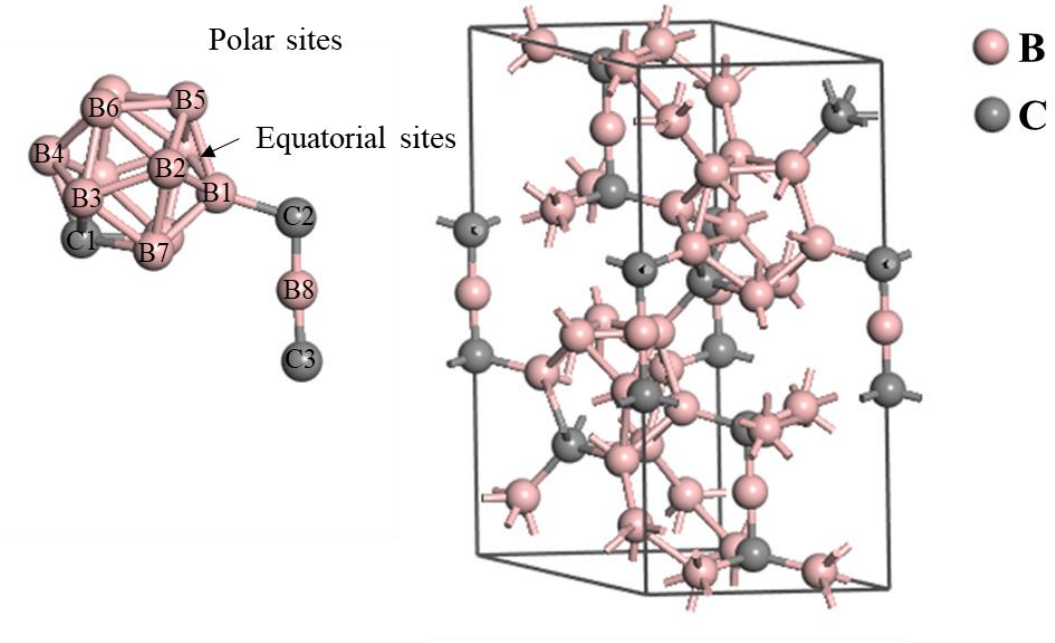

Figure 6.1 Structure of a B_4C cell in hexagonal representation, the icosahedron structure with a C-B-C chain is illustrated at the left. The geometrically inequivalent atom sites were labeled from B1 to B8 and C1 to C3.

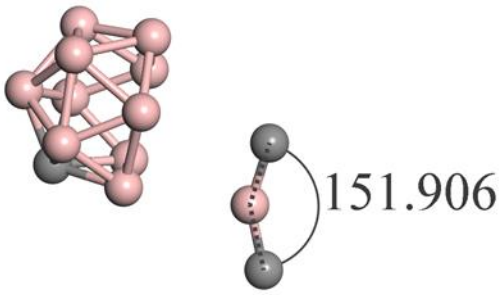

Figure 6.2 The C-B-C linear chain bent to 151.9° after geometry optimization of the structure with a vacancy on the closest equatorial site B1.

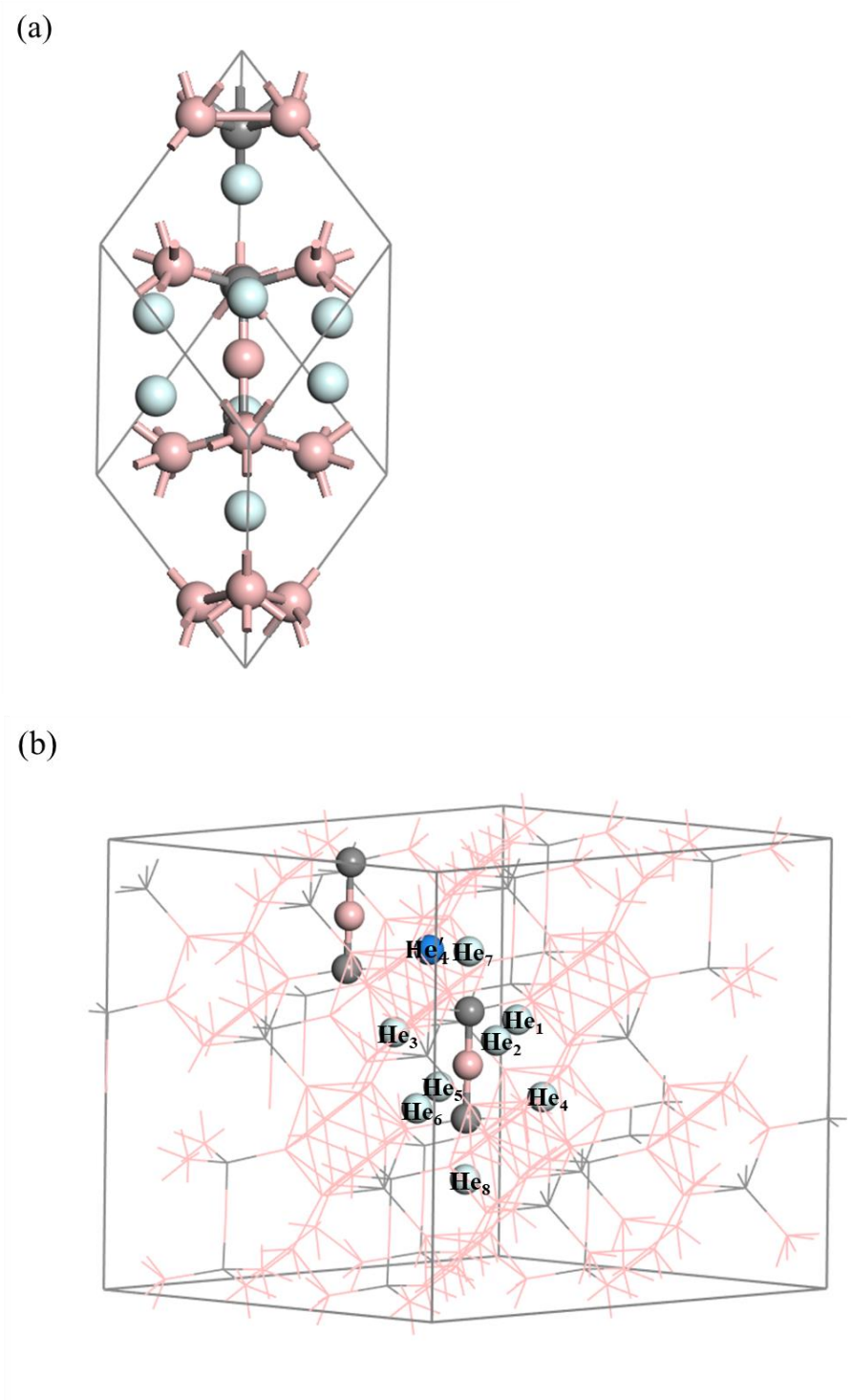

Figure 6.3 (a) The helium interstitial sites (white balls) are illustrated in a rhombohedral unit cell of B_4C (b) The helium interstitial sites around the center C-B-C chain of the 2×2×1 supercell are labeled from He_1 to He_8. The blue ball labeled as He_4' is the He_4 site belong to the upper left C-B-C chain.

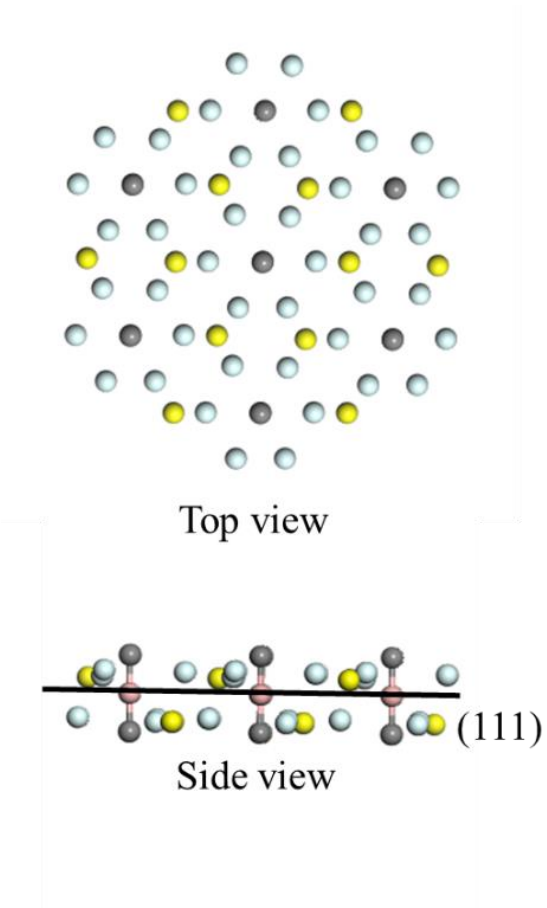

Figure 6.4 A slice of the C-B-C chains align to the (111) plane with the helium interstitial sites around them, the i-He_{1-6} sites are shown in white balls, and the i-He_{7-8} sites are shown in yellow balls, the icosahedral cages were hidden for easy observation.

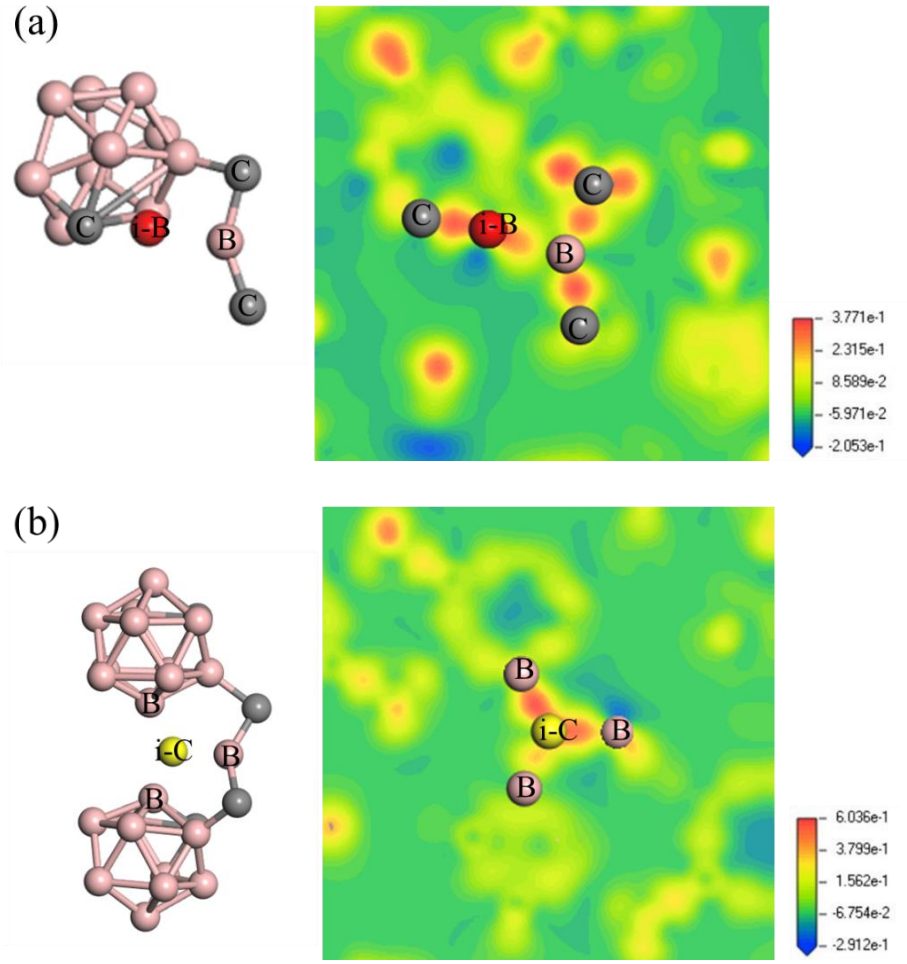

Figure 6.5 The structure distortion caused by the interstitial boron (a) and carbon (b), the differential charge density shows the interstitial boron and carbon atoms are sp^2 hybridized and form three bonds with the nearby B_4C lattice atoms.

CHAPTER 7

First-principles study on the helium migration energies in $B_{12}X_2$ (X=O, Si, P, As) crystals

This chapter is temporarily unable to publish online because the results are being submitted to a Journal.

CHAPTER 8
Conclusions

The neutron-irradiation effects on the B_4C pellets irradiated in an actual control element of JOYO have been studied with XRD, TEM, and DFT calculations. Moreover, a prediction based on DFT calculations on the helium migration energies of the $B_{12}X_2$ crystals has been made to explore the potential upgrade alternatives for the B_4C absorber.

The XRD study on the neutron-irradiated B_4C samples with different burnups revealed there is an anisotropic reaction on the B_4C lattice to the neutron irradiation. The expansion in *a*-axis and shrinkage in *c*-axis in the neutron-irradiated B_4C were confirmed in our measurement. Furthermore, the changes in the lattice parameters are greatly affected by temperature. After annealed at 1000°C for 1h, the lattice parameters of the neutron-irradiated B_4C samples were almost completely numerically restored to the original values. However, broadening in the diffraction peaks mostly remains which indicated the annealing up to 1000°C have little effect on the strains induced by the helium bubbles. Only a small recovery in the breadths of diffraction peaks associated to the rhombohedral (111) peaks was confirmed after annealed at 1000°C. It was speculated because of the thermally activated migration of the interstitial helium atoms which reduced the lattice distortion.

The follow-up TEM observations showed the neutron-induced helium formed numerous tiny bubbles in the B_4C grains. In the B_4C sample irradiated in an irradiation rig of JOYO, the bubbles were in a flat plate shape, and all perfectly parallel to the rhombohedral (111) plane in each grain. The result negated the conclusion made by some previous studies that the helium bubbles are parallel to the {110} or {100} plane. However, the morphologies of the helium bubbles in the B_4C samples from an actual control rod were significantly different from the capsule-irradiated sample. The helium bubbles in the actual control rod pellets were less grow-up and mostly in a tiny uni-

sized spherical shape. These tiny bubbles form arrays approximately parallel to the rhombohedral (111) plane, which implied they were stacked in the previous stage of forming the larger plated-shaped bubble observed in the capsule-irradiated sample. The reason is considered as the result of the short duration of high temperature caused by the frequent movement of the control rod. The irradiation temperature seems dominated the morphology of the helium bubbles in B_4C, and the impact of burnup is limited to the bubble density. Furthermore, helium bubbles/cracks several times larger the ordinary ones are sometimes found on the {100} planes. In the view of the previous studies showed the characteristic of B_4C that forming amorphous bands along the {100} planes under stress, the formation of large bubbles on the {100} planes are regarded as a result of the partial amorphization on the {100} planes. Due to the small number, it should not significantly affect the swelling behavior of the B_4C pellet. Finally, a liquid phase appeared during the in-situ heating of the specimens at temperatures over 800°C indicated a lot of the neutron-induced lithium remains in the interstitial sites of the B_4C lattice.

Due to both of the results of XRD and TEM showed the anisotropic reaction of B_4C to the neutron radiation may relate to the (111) plane. Further theoretical investigations based on DFT were carried out. The calculations on the neutron-induced point defects showed the vacancies caused by neutron collisions are tend to concentrate at the C-B-C chain center sites which explained the shrinkage in the *c*-axis after neutron irradiation. Moreover, the calculation results of the migration energies of helium and lithium showed a great anisotropy, which indicated the helium and lithium atoms in B_4C tend to follow a two-dimensional diffusion regime parallel to the (111) plane at low temperature. The faster migration speed of helium along the (111) plane is assumed as the reason of the small bubbles merge into larger plate-shaped bubbles parallel to the (111) plane. In addition, the formation energies of lithium interstitial defects are much smaller than the helium interstitial defects, which explained why the lithium precipitate was never confirmed by TEM observation of neutron-irradiated B_4C, regardless of their burnups.

Otherwise, due to the heavy fragmentation of the B_4C pellet under neutron radiation is an important factor that accelerated the ACMI which caused the short life of the B_4C control rods, improving the toughness of the absorber pellets is also effective in prolonging the service life of the B_4C control rod for the fast reactors. A method to improve the ductility of B_4C by switching the C-B-C chains into weaker two-atom chains have been presented. To verify if these B_4C based materials could be utilized as neutron absorbers for the fast reactors, DFT calculations on the migration energies of helium in these materials were carried out. The results showed the migration energies of helium in $B_{12}Si_2$ and $B_{12}O_2$ are lower than that in B_4C, and also the formation energies of helium interstitial defects are lower in these two crystals than in B_4C. Therefore, more neutron-induced helium atoms could exist in the lattice of $B_{12}Si_2$ and $B_{12}O_2$ without forming helium bubbles which is difficult to eliminate, and the lower migration energies mean the helium bubbles could be excluded from the grains more easily. The $B_{12}Si_2$ and $B_{12}O_2$ are worth further feasibility study on substituting the B_4C as neutron absorbers for fast reactors.

In summary, it's time to go back to the three questions raised in chapter 1:

1. How would the changing irradiation environment of an actual control rod of a FBR affect the B_4C pellet?
2. Why do the helium form bubbles in a flat disk-like shape?
3. Could the anisotropic reactions of B_4C under the neutron irradiation be utilized to improve the performance of the pellet?

My answers are given as follow:

1. The changing irradiation environment of actual control rods is mainly reflected in the shapes of helium bubbles. Due to the duration of the pellet at high temperature may very short, there is not enough time for the helium bubbles growing up. Even the estimated maximum irradiation temperatures are the same, the B_4C pellets irradiated in actual control rods tend to show the characteristics of irradiated at a lower temperature. Therefore, the maximum irradiation temperature cannot be used to infer the state of the helium bubbles in an actual control rod pellet.

2. The formation of the flat disk/plate-shaped bubbles could be regarded as a result of the fast helium migration along the (111) plane. The tiny helium bubbles formed at the early stage of neutron irradiation were considered have a certain mobility driven by the gradient in the concentration of defects (vacancy and helium interstitial atoms). The fast helium migration along the (111) plane make the small helium bubbles on the same level easier to get close to and merge each other. Consequentially, the bubbles grow much faster along the (111) plane than in the other dimension—it is not surprising that the grown-up helium bubbles are all in flat disk-like shapes parallel to the (111) plane.
3. Due to the helium in the neutron-irradiated tend to form plate-shaped bubbles parallel to the (111) plane, and it is easier for the helium migrate along the (111) plane, we have reasons to believe that the orientation-controlled B_4C polycrystalline pellet could reduce the radial expansion to some extent, which directly induced the ACMI, by the more efficient helium exhaust passage and transferring the swelling induced by the intragranular bubbles to the axial direction.